

An-Najah National University
Faculty of Graduate Studies

Structural, Electronic and Magnetic properties of $\text{Ga}_{1-x}\text{Fe}_x\text{N}$
($x = 0, 0.25, 0.5, 0.75, 1$) Alloys in Zincblende Structure:
First-Principles Study

By

Mahmoud Mohammed Ahmed Eissa

Supervisor

Dr. Mohammed Salameh Salem Abu-Jafar

Co- Supervisor

Dr. Abdel-Rahman Mustafa Abu-Labdeh

This Thesis is Submitted in Partial Fulfillment of the Requirements for the Degree of Master of Science in Physics, Faculty of Graduate Studies, at An-Najah National University, Nablus, Palestine.

2010

To the Memory of my Mother.

To my father, brothers, and sisters.

Structural, Electronic and Magnetic Properties of Ga_{1-x}Fe_xN (x=0,0.25,0.5,0.75, and 1) Alloys in Zincblende Structure: First-Principles Study

To my children: Shams Al-Deen, Shada, Ishraq, and Habeeb.

By
Mahmoud Mohammed Ahmed Eissa

This thesis was defended successfully on 2/12/2010 and approved by:

Defense Committee Members

Signature

- Dr. Mohammed Abu-Jafar (Supervisor)

Moh'd S.

- Dr. Abdel-Rahman Abu-Labdeh (Co-supervisor)

Abdel-Rahman

- Dr. Rushdi Kitaneh (External Examiner)

Rushdi Kitaneh

- Prof. Sami Al-Jaber (Internal Examiner)

Sami Al-Jaber

Dedication

To the Memory of my Mother.

To my father, brothers, and sisters.

To my wife who always encourages me to further of my study.

To my children: Shams Al-Deen, Shada, Ishraq, and Habeeb.

Acknowledgment

In the beginning I'd like to express my appreciation to my supervisors Dr. Mohammed S. Abu-Jafar and Dr. Abdel-Rahman M. Abu-Labdeh for their important guidance and supervision.

Also I am grateful to Dr. Musa El-Hassan for his guidance.

I'd like to thank all my teachers at An-Najah National University, and special thanks to my group at my faculty. My thanks go as well to the members of the jury.

اقرار

انا الموقع ادناه مقدم الرسالة التي تحمل العنوان :

**Structural, Electronic and Magnetic properties of Ga_{1-x}Fe_xN
(x = 0 , 0.25, 0.5, 0.75, 1)Alloys in Zincblende Structure:
First-Principles Study**

اقر بأن ما اشتملت عليه هذه الرسالة انما هو نتاج جهدي الخاص، باستثناء ما تمت الاشارة اليه حيث ورد، وان هذه الرسالة ككل، او أي جزء منها لم يقدم من قبل لنيل اية درجة او لقب علمي او بحث لدى مؤسسة تعليمية او بحثية اخرى.

Declaration

The work provided in this thesis, unless otherwise referenced, is the researcher's own work, and has not been submitted elsewhere for any other degree or qualification.

Student's name: Mahmoud Mohammed Eissa

اسم الطالب : محمود محمد عيسى

Signature :

التوقيع :

Date :

التاريخ : 2010 \ 12 \ 2

Table of contents

Section	Subject	Page
	Committee Decision	II
	Dedication	III
	Acknowledgment	IV
	Declaration	V
	Contents	VI
	List of Tables	VIII
	List of Figures	X
	Abstract	XIII
	Chapter I: Introduction	1
	Chapter II: Density Functional Theory	14
2.1	Introduction	14
2.2.1	The Born-Oppenheimer approximation	16
2.2.2	Hartree and Hartree-Fock Approximation	16
2.2.3	Density Functional Theory (DFT)	18
2.3	Single particle Kohn-Sham equation	21
2.4.1	The local spin density approximation LSDA	24
2.4.2	Generalized Gradient Approximation	25
	Chapter III: Methodology	26
3.1	Introduction	26
3.2	The Augmented Plane Wave Method (APW)	26
3.3	Linearized Augmented Plane Wave Method (LAPW)	29

3.4	The Augmented Plane Wave Plus Local Orbitals (APW +LO)	31
3.5	The Full Potential Calculation	33
3.6	WIEN2K code	34
3.7	Self-Consistent Cycles (SCF)	34
3.8	Mechanisms used to explain magnetic properties	35
	Chapter IV: Computational Details, Results and Discussions	38
4.1	Convergence Tests	39
4.1.1	k-points Test	40
4.1.2	$R_{MT} \cdot K_{max}$ Cutoff Test	51
4.1.3	Optimization	61
4.2	Structural properties	62
4.2.1	GaN in Wurtzite Structure	62
4.2.2	$Ga_{1-x}Fe_xN$ Zinc-blend Structure (ZB)	68
4.2.2.1	GaN compound	68
4.2.2.2	$x=0.25, 0.5, 0.75$	71
4.2.2.3	FeN Binary Compound	76
4.3	Electronic Properties of $Ga_{1-x}Fe_xN$	82
4.3.1	Band structure and band gap energy	82
4.4	Magnetic Properties of $Ga_{1-x}Fe_xN$ alloys	91
	Chapter V : Conclusions	95
	References	97
	الملخص	ب

List of Tables

4.1.1	K -points tests for GaN in wurtzite structure for both LSDA and GGA methods	40
4.1.2	K-points tests for GaN in ZB structure for both LSDA and GGA methods	41
4.1.3	K-points for $\text{Ga}_{0.75}\text{Fe}_{0.25}\text{N}$ in ZB structure for both LSDA and GGA methods	41
4.1.4	K-points for $\text{Ga}_{0.5}\text{Fe}_{0.5}\text{N}$ in ZB structure for both LSDA and GGA methods	42
4.1.5	K-points for $\text{Ga}_{0.25}\text{Fe}_{0.75}\text{N}$ in ZB structure for both LSDA and GGA methods	42
4.1.6	K-points for FeN in ZB structure for both LSDA and GGA methods	43
4.1.7	The total K_{mesh} and K_{irred} that is sufficient to perform the calculation for $\text{Ga}_{1-x}\text{Fe}_x\text{N}$ in ZB structure.	44
4.1.8	$R_{\text{MT}} \cdot K_{\text{max}}$ cutoff test for GaN in Wurtzite structure	51
4.1.9	$R_{\text{MT}} \cdot K_{\text{max}}$ cutoff test for $\text{Ga}_{1-x}\text{Fe}_x\text{N}$ ($x=0$) in ZB structure	52
4.1.10	$R_{\text{MT}} \cdot K_{\text{max}}$ cutoff test for $\text{Ga}_{1-x}\text{Fe}_x\text{N}$ ($x=0.25$) in ZB structure	52
4.1.11	$R_{\text{MT}} \cdot K_{\text{max}}$ cutoff test for $\text{Ga}_{1-x}\text{Fe}_x\text{N}$ ($x=0.50$) in ZB structure	53
4.1.12	$R_{\text{MT}} \cdot K_{\text{max}}$ cutoff test for $\text{Ga}_{1-x}\text{Fe}_x\text{N}$ ($x=0.75$) in ZB structure	53
4.1.13	$R_{\text{MT}} \cdot K_{\text{max}}$ cutoff test for $\text{Ga}_{1-x}\text{Fe}_x\text{N}$ ($x=1.0$) in ZB structure	54
4.1.14	$R_{\text{MT}} \cdot K_{\text{max}}$ for $\text{Ga}_{1-x}\text{Fe}_x\text{N}$ in ZB structure using LSDA and GGA methods.	61
4.2.1	c/a ratio of GaN in wurtzite structure by LSDA approximation method.	63
4.2.2	c/a ratio of GaN in wurtzite structure by GGA approximation method	63

4.2.3	u-test for GaN in wurtzite structure using LSDA and GGA methods	64
4.2.4	Lattice parameters, Bulk modulus, and pressure first derivative of GaN in wurtzite structure using LSDA and GGA approximations with other calculations	65
4.2.5	Lattice parameters, Bulk modulus, and pressure first derivative of GaN in ZB structure using LSDA and GGA approximations, with other calculation and experimental results	70
4.2.6	Lattice parameters, Bulk modulus, and pressure first derivative of $\text{Ga}_{1-x}\text{Fe}_x\text{N}$ in ZB structure using LSDA and GGA approximations	75
4.2.7	Lattice parameters, Bulk modulus, and pressure first derivative of FeN in ZB structure using LSDA and GGA approximations	78
4.3.1	Direct and indirect band gap energy of $\text{Ga}_{1-x}\text{Fe}_x\text{N}$ alloys for different concentrations at equilibrium volume	89
4.4.1	Total and local Magnetic Moment in $\text{Ga}_{1-x}\text{Fe}_x\text{N}$ system in ZB structure using LSDA and GGA approximations	92

List of Figures

1.1	Schematic magnetic phase of a) FM. b) AFM, and c) FIM.	9
2.1	Flow chart of the n^{th} iteration in the self consistent procedure to solve Hartree-Fock or Kohn-Sham equations	23
3.1	adaption of the basis set by dividing the unit cell into atomic spheres and interstitial regions	27
3.2.	Impurity levels of magnetic transition metal impurities in semiconductors: For Fe on the III-site in III-V semiconductors, the double degenerate e^+ state and one of the three degenerate of t^+ states are occupied	36
4.1	<i>GaN k-points test in wurtzite structure using: (a) LSDA (b) GGA methods</i>	45
4.2	<i>GaN k-points test in ZB structure using (a) LSDA (b) GGA methods</i>	46
4.3	<i>Ga_{0.75}Fe_{0.25}N k-points test in ZB structure using: (a) LSDA (b) GGA methods</i>	47
4.4	<i>Ga_{0.5}Fe_{0.5}N k-points test in ZB structure using: (a) LSDA (b) GGA methods</i>	48
4.5	<i>Ga_{0.25}Fe_{0.75}N k-points test in ZB structure using (a) LSDA (b) GGA methods</i>	49
4.6	<i>FeN k-points test in ZB structure using (a) LSDA (b) GGA methods</i>	50
4.7	<i>R_{MT}·K_{max} cutoff test for GaN in wurtzite structure using: a) LSDA and b) GGA methods.</i>	55
4.8	<i>R_{MT}·K_{max} cutoff test for Ga_{1-x}Fe_xN (x=0) in ZB structure using: a) LSDA and b) GGA methods</i>	56
4.9	<i>R_{MT}·K_{max} cutoff test for Ga_{1-x}Fe_xN (x=0.25) in ZB structure using: a) LSDA and b) GGA methods</i>	57
4.10	<i>R_{MT}·K_{max} cutoff test for Ga_{1-x}Fe_xN (x=0.5) in ZB structure using: a) LSDA and b) GGA methods</i>	58
4.11	<i>R_{MT}·K_{max} cutoff test for Ga_{1-x}Fe_xN (x=0.75) in ZB structure using: LSDA and b) GGA methods</i>	59

4.12	$R_{MT} \cdot K_{max}$ cutoff test for $Ga_{1-x}Fe_xN$ ($x=1$) in ZB structure using: a) LSDA and b) GGA methods	60
4.13	GaN volume optimization in wurtzite structure using: a) LSDA and b) GGA methods	67
4.14	GaN volume optimization in ZB structure using: a) LSDA b) GGA methods	69
4.15	$Ga_{0.75}Fe_{0.25}N$ volume optimization in ZB structure using: a) LSDA b) GGA methods	72
4.16	$Ga_{0.5}Fe_{0.5}N$ volume optimization in ZB structure using: a) LSDA b) GGA methods	73
4.17	$Ga_{0.25}Fe_{0.75}N$ volume optimization in ZB structure using: a) LSDA b) GGA methods	74
4.18	FeN volume optimization in ZB structure using: a) LSDA b) GGA methods	77
4.19	lattice constant variation with Fe concentration for $Ga_{1-x}Fe_xN$ using : (a) LSDA (b) GGA methods	80
	Bulk modulus variation with concentration for $Ga_{1-x}Fe_xN$ using: (c)LSDA (d) GGA method	81
4.3.1	The spin polarized band structure for GaN in Zincblende structure using LSDA approximation: A) Minority spin B) Majority spin	83
4.3.2	The spin polarized band structure for GaN in Zincblende structure using GGA approximation: A) Minority spin B) Majority spin	83
4.3.3	The spin polarized band structure for $Ga_{0.75}Fe_{0.25}N$ in Zincblende structure using LSDA approximation: A) Minority spin B) Majority spin	84
4.3.4	The spin polarized band structure for $Ga_{0.75}Fe_{0.25}N$ in Zincblende structure using GGA approximation: A) Minority spin B) Majority spin	84

4.3.5	The spin polarized band structure for $\text{Ga}_{0.5}\text{Fe}_{0.5}\text{N}$ in Zincblende structure using LSDA approximation: A) Minority spin B) Majority spin	85
4.3.6	The spin polarized band structure for $\text{Ga}_{0.5}\text{Fe}_{0.5}\text{N}$ in Zincblende structure using GGA approximation: A) Minority spin B) Majority spin	85
4.3.7	The spin polarized band structure for $\text{Ga}_{0.25}\text{Fe}_{0.75}\text{N}$ in Zincblende structure using LSDA approximation: A) Minority spin B) Majority spin	86
4.3.8	The spin polarized band structure for $\text{Ga}_{0.25}\text{Fe}_{0.75}\text{N}$ in Zincblende structure using GGA approximation: A) Minority spin B) Majority spin	86
4.3.9	The spin polarized band structure for FeN in Zincblende structure using LSDA approximation: A) Minority spin B) Majority spin	87
4.3.10	The spin polarized band structure for FeN in Zincblende structure using GGA approximation: A) Minority spin B) Majority spin	87
4.3.11	direct band gap energy versus concentration of $\text{Ga}_{1-x}\text{Fe}_x\text{N}$ using : a) LSDA	89
	direct band gap energy versus concentration of $\text{Ga}_{1-x}\text{Fe}_x\text{N}$ using : b) GGA method	90
	Indirect band gap energy versus concentration of Fe in $\text{Ga}_{1-x}\text{Fe}_x\text{N}$ using: c) LSDA	90
	Indirect band gap energy versus concentration of Fe in $\text{Ga}_{1-x}\text{Fe}_x\text{N}$ using: d) GGA method	91
4.4.1	MMTOT using : a)LSDA b) GGA method	94

**Structural, Electronic and Magnetic properties of $\text{Ga}_{1-x}\text{Fe}_x\text{N}$
($x = 0, 0.25, 0.5, 0.75, 1$) Alloys in Zincblende Structure:
First-Principles Study**

By

Mahmoud Mohammed Eissa

Supervisors

Dr. Mohammed S. Abu-Jafar

Dr. Abdel-Rahman M. Abu-Labdeh

Abstract

A First-Principles method is used to calculate the electronic, structural, and magnetic properties of the semiconductors $\text{Fe}_x\text{Ga}_{1-x}\text{N}$ alloys by taking the concentrations

$x = 0, 0.25, 0.50, 0.75, 1.0$ in the zincblende structure (ZB), using a self-consistent full-potential linearized augmented plane-wave (FP-LAPW) method within the local-spin-density functional approximation (LSDA) and the generalized gradient approximation (GGA).

The program used in our calculation is WIEN2K-code, which is written in Fortran 90 that works under Linux system.

The evolution of the band structure was studied in addition to the magnetic moment as a function of the lattice parameter of the FeN compounds and the ternary alloys $\text{Fe}_x\text{Ga}_{1-x}\text{N}$.

It is found that the binary GaN has a (Γ - Γ) direct band gap energy ~ 1.9 eV, and a (Γ -x) indirect band gap energy ~ 3.2658 eV using LSDA method, it is a semiconductor with no magnetic moment for the zincblende structure.

It is found also that the band gap energy of the ternary alloys $\text{Fe}_x\text{Ga}_{1-x}\text{N}$ depend strongly on the concentration of Fe.

The binary compound FeN is found to be non magnetic, while the total magnetic moment of the ternary alloys $\text{Fe}_x\text{Ga}_{1-x}\text{N}$ depend on the concentration of Fe.

The lattice constant and the total magnetic moments of the ternary alloys $\text{Fe}_x\text{Ga}_{1-x}\text{N}$ calculated using GGA method and found to be larger than those obtained using LSDA, while the bulk modulus for the ternary alloys $\text{Fe}_x\text{Ga}_{1-x}\text{N}$ obtained using GGA method are found to be smaller than those obtained using LSDA.

Chapter I

Introduction

Currently, semiconductor materials form basic building blocks of emitters, cellular, receivers, satellite, and fiber glass communication. With respect to III-V semiconductors, the group III-nitride semiconductors have attracted much attention due to their great potential for technological applications [1-3]. The agitation generated by recent developments, arises from the fact that the nitride semiconductors belong to a family of common anion and common cation group III-V semiconductors [1, 2, 4].

The series of group III-nitrides has a high melting point, a high thermal conductivity, a large bulk modulus, and a wide band-gap. These properties are closely related to strong ionic and covalent bonding. Therefore, such materials can be used for short-wavelength light emitting diodes (LEDs), laser diodes and optical detectors as well as for high-temperature, high-power and high-frequency electronic devices. This makes them applicants for carefully tailored optoelectronic devices operating anywhere within the visible wavelength range, particularly for visible light emitters (blue and green parts of the spectrum) [5].

The direct gap of the nitrides alloys continuously extends from infrared to UV region, offering potential for new applications of these materials [6- 8].

Gallium nitride (GaN) is well recognized to hold substantial, promise for a wide range of technological applications, such as optoelectronic and electronic devices [9]. Due to promising applications, many experimental and theoretical groups have strived for a more fundamental understanding of this covalent compound. For example, it was found that GaN has a phase transition from zincblende (ZB) to rocksalt (RS) structure under high pressure using both FP-LAPW and Pseudopotential methods[10,11]. Structural, electronic, and relative stability of GaN have also been studied in depth using Pseudopotential

within GGA-PBE approximation, Full Potential-Linearized Augmented Plane waves (FP-LAPW), and ab initio method within LDA and GGA approximations [12-16].

Abu-Jafar *et al* [16] studied the structural phase transformations of GaN under high pressure using FP-LAPW and Pseudopotential within the LDA and GGA approximations. They found that the transition pressure from zincblende to rocksalt occur at 38.15 GPa, 40.80 GPa, 42.60 GPa using FP-LAPW:LDA, FP-LAPW:GGA, and PP-PW:LDA respectively. Also, they found that the transition pressure from wurtzite to rocksalt is 38.10 GPa using FP-LAPW-LDA method, and 42.30 GPa using FP-LAPW-GGA method. In addition, they found that the band gap of wurtzite structure is 2.08 eV, while for rocksalt structure is 1.7 eV using LDA approach.

Gao *et al* [17] studied the pressure dependence of structural, electronic, and optical properties for GaN using ab initio plane-wave pseudopotential density functional theory within the generalized gradient approximation for the exchange-correlation potential. They found that the wurtzite to rocksalt phase transition occurs at pressure 48.5 GPa. They also found that the band gap energy of wurtzite GaN at 48.5 GPa pressure is a direct (Γ - Γ) band gap semiconductor of 2.1 eV, while for rocksalt at the same pressure is indirect (L-X) gap of 1.9 eV.

Xiao *et al* [10] also investigated the structural phase transformations of GaN under high-pressure using ab initio method based on density functional theory within the frame work of localized density approximation using SIESTA code. They found that a structural phase transition from ZB to RS structure takes place at a pressure of 34 GPa.

Tan Li-Na *et al* [11] investigated the structure and the high pressure phase transition in GaN using the first principle plane wave pseudopotential density functional method combined with the ultra soft pseudopotential scheme in the generalized gradient approximation (GGA) correction. They found that the phase transition from wurtzite structure and the zincblende structure to the rocksalt structure occur at pressures 41.1 GPa and 45.2 GPa, respectively. They also found that lattice parameters for the wurtzite structure are $a=3.204 \text{ \AA}$, $c=5.216 \text{ \AA}$, $B_0=178.5\text{GPa}$, $B_0'=4.502$, and for the zincblende structure are $a= 4.525 \text{ \AA}$,

$B_0 = 177.6$ GPa, $B_0' = 4.414$, but for the rocksalt structure are

$a = 4.248$ Å, $B_0 = 217.5$ GPa, $B_0' = 4.71$.

Structural and electronic properties of GaN have also been investigated by Daoudi *et al* [12] using the full potential linearized augmented plane wave (FP-LAPW) approach within the density functional theory (DFT) in the local density approach (LDA) and the generalized gradient approximation (GGA) for the exchange correlation potential. Within the LDA approximation, they found that the wurtzite structure of GaN has lattice parameters

$a = 3.1555$ Å, $c = 5.1528$ Å, $B_0 = 205.42$ GPa, $B_0' = 4.37$ and

$E = 2.091$ eV ; while within the GGA approximation the lattice parameters are $a = 3.2241$ Å, $c = 5.2487$ Å, $B_0 = 172.38$ GPa, $B_0' = 5.23$, and $E = 1.68$ eV.

For zincblende structure and within the LDA approximation, they found that GaN has a lattice parameters $a = 4.4637$ Å, $B_0 = 205.3$ GPa, $B_0' = 4.29$, and $E = 1.922$ eV; while within the GGA approximation the lattice parameters are $a = 4.5564$ Å, $B_0 = 173.95$ GPa, $B_0' = 3.75$, and

$E = 1.517$ eV.

Arbouche *et al* [13] studied the structural and electronic properties of GaN compound using the first-principle full-potential augmented plane wave approach within the generalized gradient approximation. They found that the wurtzite structure is preferred at ambient pressure. Also, they found that

the lattice parameters for wurtzite structure are $a=3.221 \text{ \AA}$, $c/a= 1.616$, $B_0=176.54\text{GPa}$, $B_0'=4.37$, for zincblende structure are $a=4.525 \text{ \AA}$, $B_0=175.32\text{GPa}$, $B_0'=3.51$, and for rocksalt structure are $a=4.26 \text{ \AA}$, $B_0=224.7\text{GPa}$, $B_0'=3.99$. The band gap they found is direct for both wurtzite and zincblende structures and equal to 1.886 eV and 1.7 eV, respectively. However, for rocksalt structure they found that it is indirect and equals to 1.9036 eV.

Saib *et al* [15] studied the structural phase transformations of GaN under high pressure using the local density and generalized gradient approximations for the exchange-correlation potential for the wurtzite, zincblende, and rocksalt structures. They found that the lowest-energy state is that of the wurtzite structure.

Iron nitride (FeN) systems have also been of great importance in the field of magnetism and magnetic materials since the early 1970's, when Kim and takahashi found giant magnetic moments in evaporated Fe_{16}N_2 polycrystalline films [18]. The existence of nitrogen (N) atoms can influence charge transfer between 4s, 4p, and 3d bands of iron atoms and is liable for the change in magnetic moment[19]. In addition, iron nitride films have received attention for many years. Initially, they have been studied due to their ability to improve surface hardness and wear resistance.

Houari *et al* [20] investigated the magnetic moment of pure FeN compound using the scalar-relativistic augmented spherical wave method (ASW).

They found that it has a zero magnetic moment in ZB structure. In another work [21] they used the same method with a generalized gradient GGA and investigated the structural and magnetic properties of FeN in RS, ZB, and wurtzite (WZ) structures. They found that RS structure is more stable than others, and the ground state of FeN-RS is ferromagnetic with a high moment, while ZB-FeN and W-Fe are non magnetic.

The electronic structures of a number of binary 3d transition metal and iron nitrides, have been investigated by means of spin-polarized first principles band structure calculations using the tight binding (TB) version of the linear muffin-tin orbital (LMTO) method [22] " The binary transition metal nitride set includes ScN, TiN, VN, CrN, MnN, FeN, CoN and NiN, both in the sodium chloride as well as in the zinc blende structure type. Antibonding metal–metal interactions for higher electron counts are significantly weaker in the zinc blende type, thus favoring this structural alternative for the later transition metal nitrides".

Experimentally[23], FeN is reported to be antiferromagnetic (i.e., zero magnetic moment). However, it is possible for FeN to have magnetic moment by growing it on different types of substrates, or by alloying it with other nitrides such as GaN.

Iron nitrides, having different complex phases (such as Fe_{16}N_2 , Fe_8N , Fe_4N , Fe_3N_2 , Fe_2N , and FeN), are attractive due to their high magnetic moments, their resistance to oxidation and corrosion, and their potential

properties[24]. Analyzing the properties of a separate phase of FeN system faces a problem, because it was very difficult to prepare FeN films having a single phase. So it is useful to explore growth of high quality single phase epitaxial FeN films. While the more Fe-rich phases are expected and have been found to be magnetic, FeN systems are also interesting due to their potential applications.

Wenzhi *et al* studied the growth of iron nitride on gallium nitride using molecular beam epitaxy with Fe e-beam evaporation and rf N-plasma growth[25]. The samples were analyzed using a variety of techniques including x-ray diffraction, Rutherford backscattering, and atomic force microscopy. They found that the lattice constant of FeN lies in the range 4.29 - 4.34Å, which is in good agreement with the lattice constant (4.33Å) reported experimentally for Zincblende[26].

Kong investigated the structure dependent magnetic moment of FeN using the tight binding (TB) version of the linear muffin-tin orbital (LMTO) method. He found that the antiferromagnetic sodium chloride (NaCl) structure have the lowest energy at the theoretical equilibrium volume. Also he found that the ferromagnetic NaCl phase lies only 1 mRyd higher. Indeed he found that the equilibrium lattice constant for nonmagnetic ZnS-type of FeN agrees quite with the experimental value (4.33Å), but the lattice constant of antiferromagnetic NaCl phase (4.2Å) is 6.7% smaller than the experimental value[27].

Semiconductors can be grouped into three classes:

Conventional (CSs), magnetic (MSs), and dilute magnetic semiconductors (DMSs). Magnetic semiconductors differs from conventional by doping with high concentration of magnetic ions; so these compounds have ferromagnetic properties in addition to semiconducting. Much efforts done to combine the benefits of the magnetic, electronic, and optoelectronic areas. Hence new class of material has recently been demonstrated. On the other hand, DMSs are conventional semiconductors (i.e., GaAs, GaN, AlN, etc.) which doped with low concentration of magnetic ions (i.e., Mn, Co, Ni, Fe, etc.).

In DMSs and MSs the host semiconductor is doped with magnetic impurities, usually a transition metal (TM) such as manganese, iron, cobalt, etc. The main attraction of MSs and DMSs is the potential establishment into presently used semiconductor-based devices. Because of their half-metallicity and structural similarity to conventional semiconductors, they are hopeful materials for a future spin-polarized electronics (or simply called spintronics). Therefore, spintronics is a field which uses the spin of carriers in addition to their charges to achieve new functionalities in electronic device[28].

The discovery of ferromagnetic in dilute magnetic semiconductors has attracted much interest in understanding the microscopic origin of the magnetic interactions in these systems [29]. It is commonly assumed that

ferromagnetic (FM) or antiferromagnetic (AFM) is the most stable magnetic structure for DMSs. In a FM phase (Figure 1.1a), the magnetic moments of the magnetic ions are aligned in the same direction and this leads to the maximum total magnetization. In the AFM phase (Figure 1.1b), magnetic moments of ions have the same magnitude but align in opposite direction to each other. Therefore, the total magnetic moment for the AFM phase is zero. In contrast, the ferrimagnetic phase (FIM) has a substantial net magnetization resulting from antiparallel alignment of a non equivalent spins of neighboring ions as shown in (Figure 1.1c)[30].

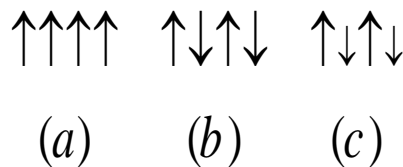


Figure 1.1: Schematic magnetic phases of (a) FM, (b) AFM, and (c) FIM

In 1980, Ohno [31] successfully introduced Mn into nonmagnetic semiconductor GaAs host, and found that the Curie temperature (T_c) of that compound was 110K. Since then, there have been numerous theoretical and experimental studies of DMSs for II-IV, III-V, and IV semiconductors.

Sato and Katayama [32] investigated the materials designed for new DMSs, whose magnetic properties can be controlled by changing carrier density, using first principle calculation. They found that high T_c ferromagnetic DMSs are realized with ZnS-, ZnSe-, and ZnTe-based DMSs doped with V or Cr; and ZnO-based DMSs doped with V, Cr, Fe, Co, or Ni. Also they

found that GaAs- and GaN-based DMSs doped with V, Cr, or Mn are candidates for high T_c ferromagnets. While Mn-doped ZnO changes its magnetic state from the spin glass state to ferromagnetic state with increasing hole concentration, it is also possible to raise T_c of Co-, Fe-, or Ni-doped ZnO by electron doping. In addition, Sato and Katayama showed that DMS of Fe doped GaN has a stability in the spin glass state more than ferromagnetic state[33].

Dalpian *et al* [30] studied the magnetic properties of GaN-Fe using the all electron-projected augmented wave (PAW) method and density-functional theory (DFT) within the generalized gradient approximation of Perdew-Burke-Ernzerhof (GGA-PBE), as implemented in the Vienna ab initio simulation package (VASP). They found that the magnetic interaction in this compound is AFM (Figure 1.1b) when the system is neutral. However, when holes are inserted into the system, the magnetic interaction becomes FIM (Figure 1.1c). In this case, nearest Fe atoms tend to have spin aligned in opposite direction but with non-equal magnetic moments. It was found that the system has net magnetization, but the total magnetic moment per Fe is much smaller than that expected for a ferromagnetic GaN: Fe system. They also found that for GaN- Fe the total magnetization increases when more hole carrier introduced, which is opposite to the observed trends in conventional ferromagnetic DMS system.

The Fe impurity in III-V and II-VI compound semiconductors has been the subject of research of several decades. In the past, it was studied as a

certain defect providing experimental information of interest for outlook of group theory. Fe is also introduced intentionally into semiconductors used in electronic and optoelectronic devices to achieve semi-insulating substrate material[34].

Today transition metal (TM) doped semiconductor materials are the main subject of recent attempts to realize ferromagnetic semiconductors for spintronics applications [31, 35-37]. High Curie temperature and room temperature ferromagnetism have been predicted in GaN-doped with TM elements, such as Mn, Fe, and Cr. This open the door for room temperature, semiconductor-based spintronics applications. Fe-doped GaN films are becoming increasingly popular in their highly resistive form for use as insulating buffer layers or substrates in GaN-based device technology.

Seung-Cheol *et al* [38] investigated the electronic and magnetic structure of the TM doped GaN using the Vienna ab initio simulation package within GGA approximation. They found that the magnetic moments were concentrated on TM in the cases of V, Cr, and Mn doped GaN, which cannot be used for DMS. The probable mechanism for these elements could be the short-ranged double exchange. Since Fe and Ni doped GaNs are intrinsic insulators because of the crystal field splitting and exchange splitting of d-like bands in tetrahedral environment, Fe and Ni doped GaNs could not be used for DMS materials unless additional dopants are introduced.

Choi and Chang [39] investigated the stability of the cubic phase in GaN doped with 3d TM ions. They found that the stability of the ZB phase is attributed to the stronger p-d repulsion between the impurity 3d state and the N-derived valance band maximum in the ZB structure. In the GaFeN alloys the stabilization of ZB phase occurs at a higher concentration in the GGA calculation.

Fong *et al* [40] studied the electronic and magnetic properties of DMSs for iron and manganese doping zinc-blende GaN by the LMTO-TB method. Fe magnetic moment was found to be $3.5\mu_B$ and $1.0\mu_B$ for cation and anion substitution, respectively. While the magnetic moments of Mn were found to be $3.3\mu_B$ and $1.9\mu_B$.

Ranber Singh [41] investigated the local magnetic structure around substitutional 3d TM impurities at cation sites in ZB structure of III-V (GaN, GaAs) and II-VI (ZnTe) semiconductor materials using a spin polarized density functional theory (VASP). He found that Cr-, Co-, Cu-doped GaN, Cr-, Mn-doped GaAs, and Cr-, Fe-, Ni-doped ZnTe are half metallic with 100% spin polarization. Also, he found that the total magnetic moment of Fe-doped GaN is $4.35\mu_B$ for iron concentration at 6.25% .

Bonanni *et al* [42] investigated the magnetic properties of Fe-doped GaN experimentally. They found that a ferromagnetic like response is shown to arise from the (Ga,Fe)N epilayers. It increases with the iron concentration.

The DMS materials-based spintronics devices are proposed to use both s and p electrons of host semiconductors and d electrons of TM impurities to perform their semiconducting and magnetic function [43]. So the magneto-optical effect in DMSs is directly related to the interaction between the electrons of these states [44].

In order to help understanding and complete the lack in the investigated properties of $\text{Ga}_{1-x}\text{Fe}_x\text{N}$, we have studied the structural, electronic, and magnetic properties of this alloy for $x=0, 0.25, 0.5, 0.75,$ and 1 . In this work we use one of the most accurate methods, which is the full-potential linearized augmented plane wave (FP-LAPW) [45, 46] approach based on the density functional theory [47] within the local (spin) density approximation (L (S) DA) and generalized gradient approximation (GGA) using scheme of Perdew-Bruke-Ernzerhof [48]. In the current work we study the ground states properties of $\text{Ga}_{1-x}\text{Fe}_x\text{N}$ and compare between LSDA and GGA calculations. To our knowledge, no one studied these alloys with iron concentrations of 25%, 50%, 75%.

The layout of this work is as follows: Chapter II presents the basics of Density Functional Theory (DFT) and FP-LAPW+lo. Chapter III presents the methodology details. In chapter IV we report and discuss our obtained results for the system of interest. Conclusions are summarized in chapter V.

Chapter II

Density Functional Theory

2.1 Introduction:

In solids, one often starts his study with an ideal crystal that studied on atomic scale at zero temperature. The unit cell may contain several atoms at certain positions and is repeating with periodic boundary conditions. The theorists face a many-body problem, and because these particles are so light relative to the classical scale, so it is a quantum many body problem.

In principle, to study the material and its properties governed by quantum mechanics (such as relative stability, chemical bonding, phase transition, optical or magnetic properties), theorists have to solve the time independent Schrödinger equation

$$\hat{H} \Psi = E \Psi , \quad 2.1$$

where Ψ is the wave function of all participating particles, and \hat{H} is the Hamiltonian of many-particle system.

\hat{H} can be written as

$$\hat{H} = \hat{H} = \hat{T}_n + \hat{T}_e + V_{en} + V_{ee} + V_{nn} , \quad 2.2$$

where \hat{T}_n , \hat{T}_e , V_{en} , V_{ee} , and V_{nn} are given by

$$\hat{T}_n = -\frac{\hbar^2}{2} \sum_i \frac{\nabla_{\vec{R}_i}^2}{M_i}, \quad 2.3$$

$$\hat{T}_e = -\frac{\hbar^2}{2} \sum_i \frac{\nabla_{\vec{r}_i}^2}{m_e}, \quad 2.4$$

$$V_{en} = -\frac{1}{4\pi\epsilon_0} \sum_{i,j} \frac{e^2 z_i}{|\vec{R}_i - \vec{r}_j|}, \quad 2.5$$

$$V_{ee} = +\frac{1}{8\pi\epsilon_0} \sum_{i \neq j} \frac{e^2}{|\vec{r}_i - \vec{r}_j|}, \quad 2.6$$

$$V_{nn} = +\frac{1}{8\pi\epsilon_0} \sum_{i \neq j} \frac{e^2 z_i z_j}{|\vec{R}_i - \vec{R}_j|}. \quad 2.7$$

In the above equations, M_i is the mass of the ion at position \vec{R}_i and m_e is the mass of the electron at position \vec{r}_i . The first two terms in equation 2.1 represents the kinetic energy operator of the nuclei (\hat{T}_n) and the electrons (\hat{T}_e); while the last three terms correspond to coulomb electron- nuclear attraction (V_{en}), electron-electron repulsion (V_{ee}), nuclear-nuclear repulsion (V_{nn}), respectively.

The solution of equation 2.1 faces a problem due to the dependences of its wave functions on the coordinates of each particle, so we have to solve this problem using some approximations.

2.2.1 Born-Oppenheimer approximation

This approximation is one of the most important approximations. It began with the idea that nuclei are much heavier than electrons, and therefore much slower, so we can ‘freeze’ them at fixed positions. In other words, only the electrons are kept as players in our many body problem [49].

The nuclei are reduced to a given source of positive charges; they become ‘external’ to the electron cloud. After having applied this approximation, we are left with a collection of NZ interacting negative particles, moving in the ‘external’ potential of the ‘fixed’ nuclei, so the first term in equation 2.2 will be neglected and the last term will be reduced to a constant.

So the new many body Hamiltonian can be formally written as

$$\hat{H} = \hat{T}_e + V_{ee} + V_{\text{ext}} \quad 2.8$$

The many body problem obtained after Born-Oppenheimer approximation is much simpler than the original one, but the problem still difficult to be solved. It needs more simplifications.

2.2.2 Hartree and Hartree-Fock Approximation

In Hartree approximation [50], the solution of many-electron problems can be solved by assuming that the electron is free; electrons are independent from each other. By this approximation the total wave function for the electrons can be written as

$$\Psi(r_1, r_2, r_3, \dots, r_N) = \Psi_1 \Psi_2 \Psi_3 \dots \Psi_N \quad 2.9$$

where $\Psi_i(r_i)$ is the i^{th} electron wave function. With this approximation the electron density can be represented by

$$\rho(r) = \sum_{i=1}^N |\Psi_i(r)|^2 \quad 2.10$$

and time independent Schrödinger equation can be written as

$$(\hat{T}_s + \hat{V}_H + \hat{V}_{ext}) \Psi(r) = E \Psi(r) \quad 2.11$$

where \hat{T}_s is the single particle kinetic energy, \hat{V}_H is the Hartree potential; the classical component of the electron-electron potential, and is given by

$$V_H = \frac{1}{8\pi\epsilon_0} \sum_{ij} \frac{|\psi(r_i)|^2 |\psi(r_j)|^2 d^3r_i d^3r_j}{|\vec{r}_i - \vec{r}_j|} \quad 2.12$$

In Hartree approximation the electrons are non-interacting; so there exists a non-zero probability of finding two electrons occupying the same point in space.

This wave function was modified to include the spin of each electron by Hartree-Fock approximation [51]. So this is an extension of the above Hartree approximation to include the permutation symmetry of the wave function that leads to the exchange interaction caused due to Pauli exclusion principle, which states that the total wave function for a system must be anti symmetric under particle exchange. Hence, no two electrons

can have the same quantum numbers, and electrons with the same spin cannot occupy the same state simultaneously.

2.2.3 Density Functional Theory (DFT)

DFT history goes back to the early thirties of the 20th century, it is a more modern and more powerful than Hartree-Fock approximation. DFT has been formally established in 1964 by two theorems due to Hohenberg and Kohn[49], who demonstrated that the total ground state energy E of a system of interacting particles is completely determined by the electron density ρ . Therefore, E can be expressed as a functional of electron density and the functional $E(\rho)$ satisfies the variational principle[52]. Hohenberg and Kohn showed that the real ground state density is the one that minimizes $E(\rho)$ and the other ground state properties are also functional of the ground state density. In addition, this will be treated as a spin polarized system. So, the energy and other ground state properties become functional of both spin up and spin down densities.

$$E = E(\rho \downarrow, \rho \uparrow) \quad 2.13$$

The non-interacting particles of this system move in an effective local one-particle potential. This potential composed of two parts, one is the classical mean-field (Hartree) part, the second is a quantum mechanical part which is an exchange-correlation part V_{xc} , that includes all correlation effects exactly. So $E(\rho)$ can be formally written as

$$E(\rho) = T_s(\rho) + E_c(\rho) + E_H(\rho) + E_{ii}(\rho) + E_{xc}(\rho) \quad 2.14$$

where $T_s(\rho)$ represents the single particle kinetic energy, $E_c(\rho)$ is the coulomb interaction energy between the electron and the nuclei, $E_{ii}(\rho)$ term represents the interaction of the nuclei with each other, $E_H(\rho)$ is the Hartree component of the electron – electron energy given by

$$E_H(\rho) = \frac{e^2}{2} \int d^3r d^3r' \frac{\rho(\vec{r})\rho(\vec{r}')}{|\vec{r} - \vec{r}'|}, \quad 2.15$$

and $E_{xc}(\rho)$ is the exchanged-correlation energy given by

$$E_{xc}(\rho) = \int \rho(r) \varepsilon_{xc} d\rho(r) \quad 2.16$$

where $\varepsilon_{xc}(\rho)$ is the exchange-correlation energy per particle of the homogeneous electron gas.

According to the variation principle, a set of effective one-particle Schrödinger equation, (the so-called Kohn-Sham (KS) equations [53]) must be solved. Its form is

$$\{T_s + V_{\text{ext}}(\mathbf{r}) + V_H(\rho(\mathbf{r})) + V_{xc}(\rho(\mathbf{r}))\} \Phi_i(\mathbf{r}) = \varepsilon_i \Phi_i(\mathbf{r}) \quad 2.17$$

here ε_i is the one particle energy, and $\Phi_i(\mathbf{r})$ is the electron wave function. T_s represents the kinetic energy operator, V_H is the Hartree potential, V_{ext} is the coulomb potential, and V_{xc} is the exchange-correlation potential.

$V_H(\rho(\mathbf{r}))$ can be written as

$$V_H = \int \frac{\rho(\mathbf{r}')}{|\vec{r} - \vec{r}'|} d\mathbf{r}' \quad 2.18$$

and Schrödinger like equations can be written in a new form

$$\left(-\frac{\hbar^2}{2m}\nabla^2 + V_{eff}(\vec{r})\right)\psi(\vec{r}) = E\psi(\vec{r}) \quad 2.19$$

where $\psi(\vec{r})$ is the total wave function (Eigen vector) of all electrons, E is the energy (Eigen value) and V_{eff} is the effective potential given by

$$V_{eff}(\vec{r}) = V_{ext}(\vec{r}) + \int \frac{\rho(\vec{r}')}{|\vec{r} - \vec{r}'|} d\vec{r}' + \frac{\delta E_{xc}(\rho)}{\delta \rho} \quad 2.20$$

where the second term in equation 2.20 represents the Hartree potential, and the third term represents the exchange-correlation potential V_{xc} .

The Kohn-Sham equation must be solved iteratively until self-consistency is reached. The iteration cycles are needed because of the interdependence between orbitals and potential.

From equation 2.10 (the electron density equation) the V_{ext} and V_{xc} potential for the next iteration can be calculated, which defines the Kohn-Sham orbitals. This closes the self-consistent loop. The exact functional form of V_{xc} potential is not known, so we need more approximation. Local (spin) density approximation (L(S) DA) find the solution for this problem and it acts well with systems having a slowly varying density .

Generalized Gradient approximation (GGA) improves the L (S) DA by making the exchange-correlation potential depending on the local density of local volume, and on the density of the neighboring volume by adding

gradient term on the L (S) DA electron density, and it reaches to a high accuracy.

2.3 Single particle Kohn-Sham equation

Almost all approaches that have proposed for solids, involving linearized augmented plane wave method (LAPW), which will be discussed later in this chapter depend on a basis set expansion for the Kohn-Sham (KS) orbitals, with Hartree-Fock (HF) or DFT one ends with an infinite set of single electron equations of the form of equation (2.17).

The similarity between HF and KS equations means that they can be solved using the same mathematical techniques.

The theorem of Kohn and Sham can now be formulated as follows: The precise ground-state density $\rho(\vec{r})$ of an N-electron system is

$$\rho(\vec{r}) = \sum_{i=1}^N \Phi_i(\vec{r})^* \Phi_i(\vec{r}) \quad 2.21$$

where $\Phi_i(\vec{r})$ are the single-particle wave functions that represent the N lowest-energy solution of the KS equation, and

$$\Phi_n(\vec{r}) = \sum_i C_{in} \Phi_i(\vec{r}) \quad 2.22$$

Solving the equation means we want to find the C_{in} coefficients to express Φ_n given by equation (2.22). The solution of the KS equation orbital enables us to determine the C_{in} for the occupied orbital that minimize the

total energy. Φ_n cannot be described exactly because one works with a limited set of basis functions, but one can try to find a basis that can generate a function that is 'close' to Φ_n . We are dealing with a self-consistency problem: the solutions (Φ_i) determine the original equation, and the equation cannot be written down and solved before its solution is known. An iterative procedure is needed to overcome this problem (see Figure 2.1). Some starting density ρ_0 is guessed, and

a Hamiltonian H_{KS1} [53] is constructed with it. The eigen value problem is solved, and results in a set of Φ_1 from which density ρ_1 can be derived. Most probably ρ_0 will differ from ρ_1 . Now ρ_1 is used to construct H_{KS2} , which will yield a ρ_2 , etc. The procedure can be set in such a way so this series will converge to a final density ρ_f which generates a Hamiltonian H_{KSf} which gives ρ_f as a solution again.

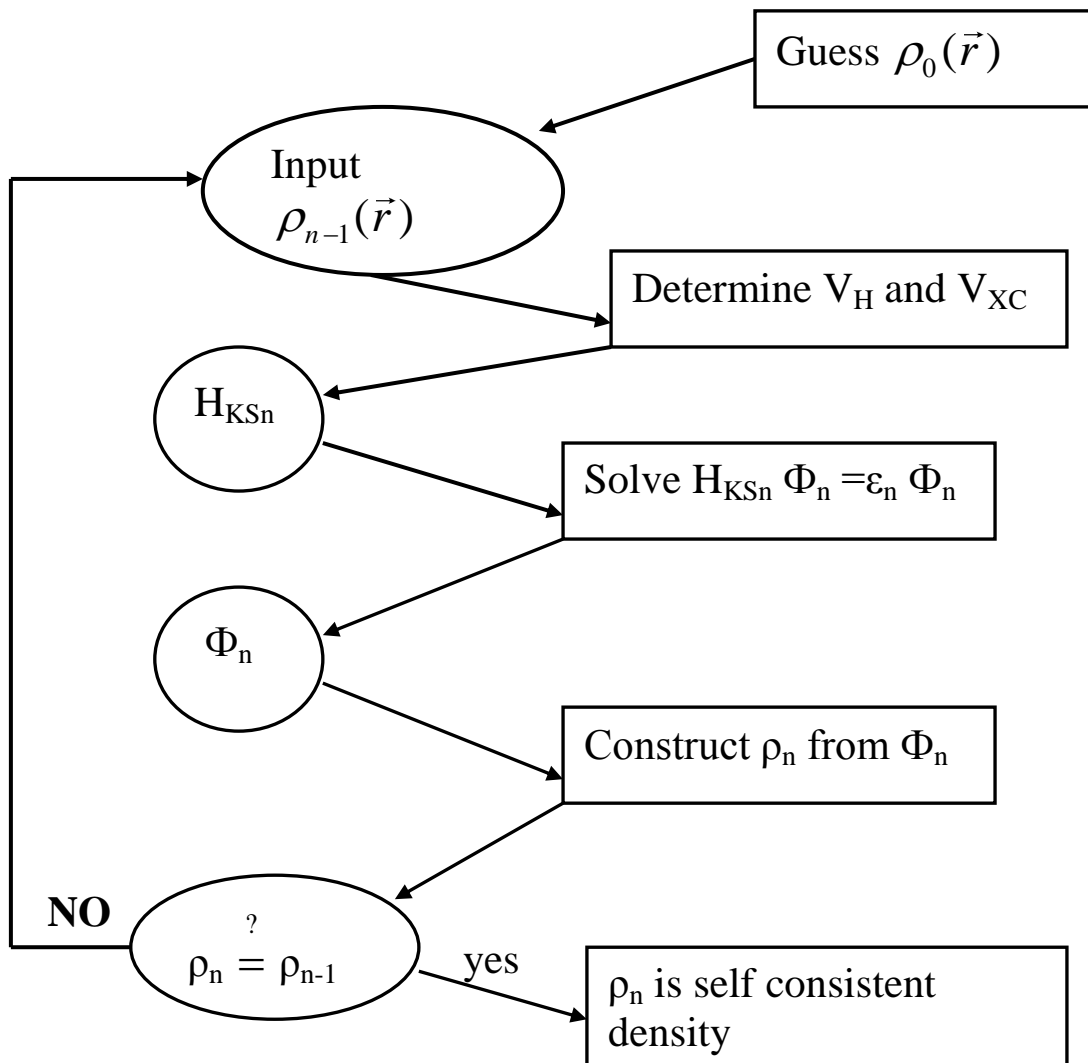


Fig. 2.1:Flow chart of the n^{th} iteration in the self consistent procedure to solve Hartree-Fock or Kohn-Sham equations.

2.4.1 The local spin density approximation LSDA

This approximation is an approximation of the exchange-correlation (XC) energy functional in density functional theory (DFT) by taking the XC energy of an electron in a homogeneous electron gas of a density equal to the density at the electron in the inhomogeneous system being calculated. Since it divides the inhomogeneous system into a small set of regions containing a homogeneous interacting electron gas with density $\rho_v(\vec{r})$, where v is the spin up or spin down; and the total density

$$\rho(\vec{r}) = \rho_{\downarrow}(\vec{r}) + \rho_{\uparrow}(\vec{r}) \quad 2.23$$

The exchange-correlation energy per particle in each homogeneous gas region can be represented as

$$\varepsilon_{xc}(\rho_{\uparrow}, \rho_{\downarrow}) = \varepsilon_x(\rho_{\uparrow}, \rho_{\downarrow}) + \varepsilon_c(\rho_{\uparrow}, \rho_{\downarrow}) \quad 2.24$$

The expression for the exchange energy $\varepsilon_x(\rho_{\uparrow}, \rho_{\downarrow})$, can be obtained from the HF approximation [53,54]. The total exchange-correlation energy E_{XC}^{LDA} is the sum of the donation of all regions [55] which is based on the quantum Monte-Carlo result of the ground-state energy for the homogeneous electron gas [56]. E_{XC}^{LDA} is given by

$$E_{XC}^{LDA}(\rho_{\uparrow}, \rho_{\downarrow}) = \int \rho(\vec{r}) \varepsilon_{XC}(\rho_{\uparrow}(\vec{r}), \rho_{\downarrow}(\vec{r})) d^3\vec{r} \quad 2.25$$

and the exchange-correlation potential is calculated from the relation

$$\begin{aligned}
 V_{XC}^{LDA}(x) &= \frac{\delta E_{XC}}{\delta \rho_v(\vec{r})} \\
 &= \varepsilon_{XC}(\rho_\uparrow, \rho_\downarrow) + \frac{\delta \varepsilon_{XC}(\rho_\uparrow, \rho_\downarrow)}{\delta \rho_v(\vec{r})} (\rho_\uparrow(\vec{r}) + \rho_\downarrow(\vec{r}))
 \end{aligned} \tag{2.26}$$

2.4.2 Generalized Gradient Approximation:

Many modern codes using DFT now use more benefit approximations to enhance accuracy for certain physical properties. Generalized gradient approximation came as a modification of (LSDA). It inserts another parameter to the exchange-correlation energy E_{XC} , the gradient of the local electron spin density is the added term so E_{XC} can be written as

$$E_{XC}^{GGA}(\rho_\uparrow, \rho_\downarrow) = \int \varepsilon_{XC}(\rho_\uparrow(\vec{r}), \rho_\downarrow(\vec{r})) \rho(\vec{r}) \nabla \rho(\vec{r}) d^3\vec{r} \tag{2.27}$$

Because of the incorporation of the local gradient, a better description of the system is expected [56-57]. The GGA improve the ground state of the light atoms, molecules, and solids and tends to produce larger equilibrium lattice parameters with respect to LSDA.

Chapter III

Methodology

3.1 Introduction:

In this chapter, we attempt to present the basic concepts of the linearized / augmented plane wave plus local orbitals (L/APW+lo). We display also the different versions of (L/APW+lo) and their principal developing steps in terms of linearization, full potential, local orbitals and mixed basis sets.

Once the DFT equations are defined in terms of the functional, there are different techniques to solve them. One of these techniques is plane waves (PWs) corresponding to Bloch functions labeled by the k -vector of the first Brillouin zone (BZ). PWs are a very inefficient basis set in describing the wave functions closed to the nuclei. To solve this problem one can eliminate oscillations due to the presence of the core electrons, as done in pseudopotential calculations or one can augment the PW basis set. This has led to the linearized / augmented plane wave plus local orbitals (L/APW+lo) method that is now one of the most accurate schemes.

3.2 The Augmented Plane Wave Method (APW):

This method is a procedure for solving KS equations by introducing a basis set which is fitted to the problem. This acceptance is achieved by dividing the space into two regions as shown in Figure 3.1.

1) The Muffin Tin region (II): where a sphere of radius $R_{MT}(\alpha)$ is drawn around each atom. The spheres are non overlapping spheres and centered at the atomic sites, r_α .

2) An interstitial region (I), which fill all the space outside the spheres. In this case the wave functions are expanded into PWs each of which is augmented by atomic solutions in the form of partial waves, i.e. a radial function times spherical harmonics. In particular, radial solutions of Schrödinger equation are employed inside non overlapping atom centered spheres and plane waves in the remaining interstitial zone.

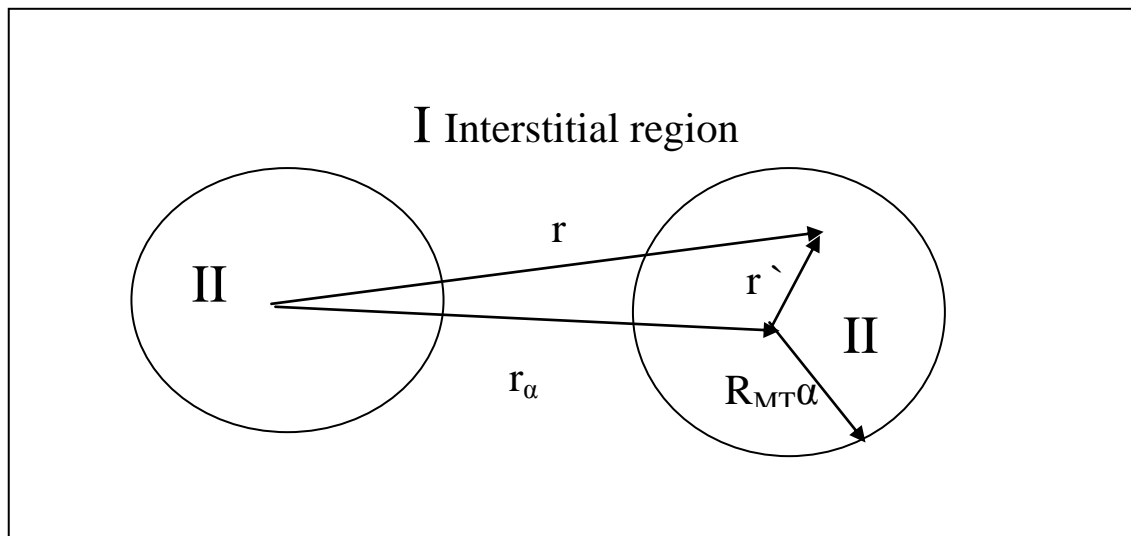


Figure 3.1: adaption of the basis set by dividing the unit cell into atomic spheres and interstitial regions.

The presence of such a basis set is due to the fact that close to the nuclei the potential and wave functions are similar to those in an atom, while between the atoms are smoother. The APWs consist of:

$$\Phi(\vec{r}) = \begin{cases} \sum_{lm} a_{lm}^{\alpha} u_{lm}^{\alpha}(r, \varepsilon) Y_{lm}(\vec{r}), & r < R_{\alpha} \\ \Omega^{-\frac{1}{2}} \sum_G C_G \exp(i(\vec{k} + \vec{G}) \cdot \vec{r}), & r \in I \end{cases} \quad 3.1$$

Where $\Phi(r)$ is the wave function, Ω is the unit cell volume, \vec{r} is the position inside sphere α with the polar coordinates \vec{r} , \vec{k} is a wave vector in irreducible Brillouin zone and u_{lm} is the numerical solution of the radial Schrodinger equation at the energy ε . The KS orbitals $\Psi(\vec{r})$ are expressed as a linear combination of APWs ($\Phi(r)$).

Inside the Muffin Tin spheres a Kohn-Sham orbital can be described accurately if the energy ε in the APW basis function equals to the eigen-energy, ε_i . So, a different energy dependent set of APW basis functions must be found for each of the eigen-energy. C_G and a_{lm} are expansion coefficients, E_1 is a parameter (set to be equal to the band energy) and V is the spherical component of the potential in the sphere.

The use of these functions has been driven by Slater[54] who noted that the plane waves are the solutions of Schrodinger's equation in a constant potential and radial functions are the solution in a spherical potential. The dual representation defined by equation 3.1 is not guaranteed to be continuous on the sphere boundary, as it must be for the kinetic energy to be well defined. So, it is necessary to impose this constraint. In the APW these conditions were done by defining the u_{lm} in terms of C_G in the spherical harmonic expansion of the plane waves.

$$u_{lm} = \frac{4\pi i^l}{\Omega^2 u_l(R)} \sum_G C_G J_l(|k + g|) Y_{lm}^*(\vec{k} + \vec{G}) \quad 3.2$$

where J_l is the Bessel function of order l . The coefficient of each lm is matched at the boundary of the sphere and the origin is taken at the centre of the sphere. The u_{lm} are determined by C_G ; coefficients of the plane wave, and E_l ; the energy parameters, which are the variational coefficients in APW method. The functions labeled G are the APWs; it consists of single plane waves in the interstitial zone, which are matched to the radial functions in the spheres.

A more accurate band structure calculational scheme is the LAPW method (discussed in the next section) where the basis functions and their derivatives are made continuous by matching to a radial function at fixed energy parameter E_l plus its derivative with respect to E_l .

3.3 Linearized Augmented Plane Wave Method (LAPW):

In the LAPW, the basis functions and their first derivatives are required to be continuous at the boundary between the sphere and the interstitial region. This means that if we calculate u_{lm} at some energy E_l , we can make a Taylor expansion to find it at energies not far from it:

$$u_{lm}(r, \varepsilon) = u_{lm}(r, E_l) + (E_l - \varepsilon) \frac{\partial u_{lm}}{\partial E} \Big|_{E=E_l} + \dots \quad 3.3$$

Substituting the first two terms of the expansion of the APW for a fixed energy E_l gives the definition of the LAPW.

This has a price; the energy difference ($E_l - \varepsilon$) is not known, hence an undetermined B_{lm} has to be introduced:

$$\Phi(\vec{r}) = \begin{cases} \sum_{lm} \left[A_{lm}^{\alpha} u_{lm}^{\alpha}(r, \varepsilon) + B_{lm} \frac{\partial u_{lm}}{\partial E} \right] Y_{lm}(\vec{r}), & r < R_{\alpha} \\ \frac{1}{\sqrt{V}} \sum_G C_G \exp(i(\vec{k} + \vec{G}) \cdot \vec{r}), & r \in I \end{cases} \quad 3.4$$

where B_{lm} are the coefficients for the energy derivative. The basis functions inside the spheres are linear combinations of radial functions and their energy derivatives. The u_l functions and its derivative satisfy the following equation:

$$\left[-\frac{d^2}{dr^2} + \frac{l(l+1)}{r^2} + V(r) - E_l \right] r \frac{\partial u_{lm}}{\partial E} = r u_{lm}(r) \quad 3.5$$

This scheme allows us to obtain all eigen-energies with a single diagonalization in contrast to APW. The LAPWs are plane waves in the interstitial zone (I) of the unit cell which match the numerical radial functions inside the spheres with the necessity, that the basis functions and their derivatives are continuous at the boundary of the spheres. Inside the spheres a linear combination of the radial functions times the harmonics,

$Y_{lm}(r)$, is used. The linear combination of the functions u_{lm} and their derivatives form the so-called "linearization" of the radial function.

The LAPWs have more freedom than APWs because of the presence of two radial functions instead of one as in APWs; the non-spherical potentials inside spheres (region II) can be treated with no difficulty.

The solution of the KS equations is expanded in this combined basis according to the linear variation method:

$$\Psi_k = \sum_n c_n \Phi_{k_n} \quad 3.6$$

C_n coefficients that can be determined by the Rayleigh-Ritz variational principle. The convergence of this basis set can be controlled by the cut-off energy $R_{MT} \times K_{Max}$, where R_{MT} is the smallest atomic radius in the unit cell and K_{Max} is the largest value of K_n vector in equation (3.6).

3.4 The Augmented Plane Wave Plus Local Orbitals (APW +LO)

Using LAPW method, it was not explicitly stated which electron states are calculated. Is it helpful to calculate the 1s electron in Fe atom in bcc structure? No, because this electron is well bounded to the nucleus (-514 Ry), such a state is called a core state. The criterion is that this state does not participate directly in chemical bonding with other atoms. Therefore, it must be contained in the muffin tin spheres. The states that leak out of these spheres, are called valence states. These states participate in chemical

bonds, and are treated in LAPW. Core states are treated as in free atoms, but it subjects to the potential due to the valence states.

Fe atom in bcc, due to hybridization, will have a non-negligible amount of 4p-character in its valence states about 0.2 Ry below the Fermi level, while the 3p-states have amount about 4.3 Ry below Fermi level. Such low-lying valence states are called semi-core states. It is not clear how $E_{l,(l=1)}^{Fe}$ should be chosen: close to 3p, close to 4p, at an intermediate value...? None of the choices is optimal. This difficult situation is solved by adding another type of basis function to the LAPW basis set, called a local orbital (*lo*). This can be defined as:

$$\Phi(\vec{r}) = \begin{cases} \left[A_{lm}^{\alpha,lo} u_{lm}^{\alpha}(r) + B_{lm}^{\alpha,lo} \frac{\partial u_{lm}}{\partial E} \right] Y_{lm}(\vec{r}), & r \in II \\ 0, & r \in I \end{cases} \quad 3.7$$

A_{lm} and B_{lm} are determined by the normalization and the new condition; the local orbital has zero value at the sphere boundary. So there is no dependence between $\frac{\partial u_{lm}}{\partial E}$ and the PWs, since it is included only in few local orbitals (e.g., p and d states) and not associated with energy plane wave. This scheme can reach the same accuracy as LAPW, but the highest efficiency was found for a mixed basis set using APW+LO in treating the low l -quantum numbers, but the higher l by LAPW.

3.5 The Full Potential Calculation:

One of the schemes that solved Kohn-Sham equation accurately is the full-potential linearized augmented plane wave (FP-LAPW) method suggested by Anderson [58] on which WIEN code is based. FP-LAPW method combines the choice of LAPW basis set with the treatment of the full-potential and charge density without any shape approximations in region I (interstitial) and region II (inside the muffin tin spheres). This generalization is achieved by relaxing the constant interstitial potential V_I and the spherical muffin tin approximation $V_{MT}(r)$ due to the inclusion of a distorted interstitial $\sum V_l^k e^{ikr}$, where k are the reciprocal lattice vectors up to the largest value k_{Max} .

$$V(\vec{r}) = \begin{cases} \sum_K V e^{i\vec{k} \cdot \vec{r}}, & \text{Interstitial - region} \\ \sum_{lm} V_{lm}(r) Y_{lm}(\vec{r}), & \text{muffin - tin} \end{cases} \quad 3.8$$

FP-LAPW method become possible with the evolution of a technique for obtaining the coulomb potential for a periodic charge density without shape-approximation and with the incorporation of the Hamiltonian matrix elements caused by the distorted interstitial and non-spherical terms of the potential.

3.6 WIEN2K code

This is a package of several programs that reduces efforts and money; it allows us to perform a computation of electronic and magnetic structure of solids using density functional theory (DFT). It is based on the FP-(L) APW+LO method, one of the most accurate schemes for band structure calculations. In DFT the (spin) density approximation (L (S) DA) or the improved Generalized Gradient Approximation (GGA) can be used. In new versions of WIEN2K [47] (APW+lo) is used inside the muffin tin spheres for the chemically important orbitals, while LAPW is used for the others.

3.7 Self-Consistent Field (SCF)

The WIEN2K package consists of several independent programs, its procedure shown in figure 2.1, initialization and self-consistent cycle programs. The first program is used to determine the space group of the structure, generates free atomic densities, generates a k-mesh in the irreducible part of the Brillouin zone and generates a starting density for the SCF cycle by a super position of the atomic densities generated for the free atom. In the second program, the potential constructed from the charge density which is used to build the Hamiltonian that used to calculate the eigen values and the eigen vectors for the valance electrons. So, a new valance electron density is obtained from the calculated eigen vectors. The core states and the densities, which are determined by a fully-relativistic self-consistent calculation, are mixed with the input density to yield a

refined input for the next iteration. A simple mixing scheme is expressed as:

$$\rho_{input}^{i+1} = (1 - x) \rho_{input}^i + x \rho_{out}^i \quad 3.9$$

Where i refers to the iteration number and x is the mixing factor.

The self-consistent cycle is repeated until convergence is achieved, when old and new electron densities are within our computational tolerance.

3.8 Mechanisms used to explain magnetic properties

III-nitrides semiconductors (e.g. GaN) are alloyed by transition metals (e.g. Fe) to form magnetic semiconductor compounds; these metals have incomplete inner electron orbits. When they loose their outermost electrons, the remaining ones in the d-shells have spins pointing in the same direction in order to minimize their energies, and these metals act as magnetic ions.

Ferromagnetism based on the interaction between d-shells in transition metals described by Zener[59]; according to Hund's rule the lowest energy for the d-shell occurs when all levels are occupied with electrons that have the same spin direction. Since each electron that has an uncompensated spin carries a magnetic moment of one Bohr magneton μ_B , the over all atom will have a finite magnetic moment associated with the number of these electrons.

Fe has 6 valance electrons and substitute for a Ga atom, 3 of the 6 electrons can replace the 3 Ga electrons in the valance band. The remaining 3 electrons have to be put in new localized d-states in the band gap, the orientation of the electrons in the 3d shells is $\text{Fe}^{+2} \uparrow\uparrow\uparrow$ with total magnetic moment $3 \mu_B$. Therefore the electronic structure of the transition metals impurities in semiconductors is dominated by d-states in the gap; only the majority states are occupied. The impurity levels are schematically indicated in figure (2.3) two different impurity levels have to be distinguished:

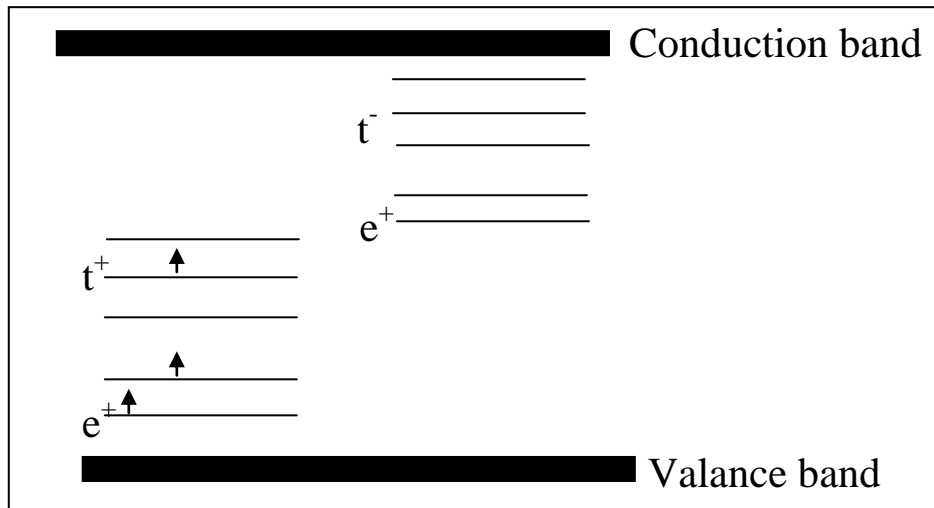


Figure 3.2: Impurity levels of magnetic transition metal impurities in semiconductors: For Fe on the III-site in III-V semiconductors, the double degenerate e^+ state and one of the three degenerate of t^+ states are occupied.

A two fold degenerate e-state ($d_{z^2}, d_{x^2-y^2}$), the wave functions for symmetry reasons hybridize very little with the valance band p-states, and a three fold degenerate t-state (d_{xy}, d_{yz}, d_{zx}) which strongly hybridize with the p-states.

In the neutral configuration only two of the e-states and one of the three t-states in the majority band are occupied, while in the minority gap states are empty. The Fermi level falls into the majority t-impurity band, such that for each Fe atom exactly two e-states and one t-state are occupied, leaving two of the majority t-states and all the minority d-states empty. Therefore the considered system is a half-metallic ferromagnetic, with a total moment of $3 \mu_B$ per Fe atom.

Chapter IV

Computational Details, Results and Discussions

When dealing with super cells and studying the magnetic properties of alloys, it is important to remember that super cell is connected to the bulk. This indicates that characteristic features of the bulk material will probably have a strong effect on the super cell properties and behavior. For example, the lattice constants for bulk material are very important to build up the super cell.

Calculating the bulk properties for the ternary alloys for the system of interest must be made after making necessary tests. K-points and $R_{MT}K_{max}$ tests are very important procedures to get best results in a short time.

In the following section we present methodical convergence tests for the system GaN in both wurtzite and zinc-blende structures, then the convergence tests for FeN, $Ga_{1-x}Fe_xN$ ($x=0.25, 0.5, 0.75$) in zinc-blende structure within LSDA and GGA methods are presented. The calculated bulk properties of the ternary alloys of $Ga_{1-x}Fe_xN$ for different concentrations $x= (0, 0.25, 0.5, 0.75, 1)$ are presented in the second section. Section three, contains electronic properties. Section four, contains the magnetic properties for the ternary alloys, by using the FP-LAPW method as executed by the WIEN2K program package. The procedure for calculating the equilibrium lattice parameters will be also discussed for every material.

4.1 Convergence Tests

The results depend on some input factors. In order to obtain reliable calculations, one must perform some convergence tests to optimize the input parameters, which have to be tested, these tests are:

1- K-points: the number of necessary irreducible k-points in the Brillouine zone (BZ) is needed to accurate structural properties, total energy, magnetic momentsetc.

2- $R_{MT}K_{max}$ tests: in the interstitial region, a plane wave expansion of the wave function and the potential should be done.

In this work, these tests are performed for determining the equilibrium lattice constants for the ternary alloys of system of interest for all concentrations. For GaN wurtzite calculations, the lattice constants $a = 3.18 \text{ \AA}$ and $c = 5.18 \text{ \AA}$ are performed as a trial values for both LSDA and GGA methods, for the k-points as well as cutoff energy convergence tests [1]. The goal of that is to get the minimum energies. However, for zincblende ternary alloys the trial values of the lattice constants that has been performed are $a = 4.52 \text{ \AA}$, 4.5 \AA , 4.35 \AA , 4.3 \AA , 4.2 \AA for concentrations $x = (0, 0.25, 0.5, 0.75, 1)$ respectively for both LSDA and GGA methods. It must be noted here that muffin-tin radii (R_{MT}) of 1.78 Bohr is used for Ga, while 1.6 Bohr for N, and 1.4 Bohr for Fe in order to insure that the spheres do not overlap.

4.1.1 k-points Test

In the k-points test, the initial $R_{\text{MT}}K_{\text{max}}$ value used 7 (where R_{MT} is the average radius of the muffin-tin spheres and K_{max} is the maximum modulus for the reciprocal lattice vector). The maximum value of l for the wave function expansion inside the atomic spheres is limited to $l_{\text{max}}=10$. The number of k-points is increased in a way that the Monkhorst-Pack grids go successfully with values of K_{mesh} as shown in tables 4.1.1, 4.1.2, 4.1.3, 4.1.4, 4.1.5, 4.1.6. The total energy dependence on the k-points at the lattice constant is also displayed.

Table 4.1.1: K -points tests for GaN in wurtzite structure for both LSDA and GGA methods.

K_{tot}	K_{mesh}	K_{irred}	$E_{(\text{LSDA})}$ eV	$E_{(\text{GGA})}$ eV
8	2*2*1	2	-7983.136162	-7995.726920
27	3*3*1	3	-7983.174891	-7995.764447
64	4*4*2	8	-7983.191983	-7995.783851
125	6*6*3	21	-7983.194554	-7995.786139
216	7*7*3	24	-7983.194972	-7995.785732
343	8*8*4	40	-7983.194752	-7995.786602
512	9*9*5	60	-7983.194805	-7995.786512
729	11*11*5	80	-7983.194762	-7995.785925
1000	12*12*6	114	-7983.194787	-7995.785999

Table 4.1.2: K-points tests for GaN in ZB structure for both LSDA and GGA methods.

K_{tot}	K_{mesh}	K_{irred}	$E_{(\text{LSDA})}$ eV	$E_{(\text{GGA})}$ eV
8	2*2*2	3	-3991.511119	-3997.811501
27	3*3*3	5	-3991.594206	-3997.878361
64	4*4*4	10	-3991.603195	-3997.903494
125	5*5*5	14	-3991.604335	-3997.904622
216	6*6*6	22	-3991.604485	-3997.904771
343	7*7*7	30	-3991.604419	-3997.904707
512	8*8*8	43	-3991.604527	-3997.904814
729	9*9*9	55	-3991.604596	-3997.904882
1000	10*10*10	73	-3991.604434	-3997.904722

Table 4.1.3: K-points for $\text{Ga}_{0.75}\text{Fe}_{0.25}\text{N}$ in ZB structure for both LSDA and GGA methods

K_{tot}	K_{mesh}	K_{irred}	$E_{(\text{LSDA})}$ eV	$E_{(\text{GGA})}$ eV
8	2*2*2	2	-14624.257090	-14648.286392
27	3*3*3	5	-14624.274593	-14648.290152
64	4*4*4	8	-14624.261698	-14648.295229
125	5*5*5	14	-14624.272129	-14648.295993
216	6*6*6	20	-14624.328091	-14648.296163
343	7*7*7	30	-14624.276415	-14648.295200
512	8*8*8	40	-14624.226031	-14648.310651
729	9*9*9	55	-14624.176196	-14648.295167

Table 4.1.4: K-points for Ga_{0.5}Fe_{0.5}N in ZB structure for both LSDA and GGA methods

K_{tot}	K_{mesh}	K_{irred}	$E_{(\text{LSDA})}$ eV	$E_{(\text{GGA})}$ eV
8	2*2*2	2	-13282.610371	-13305.560933
27	3*3*3	7	-13282.619301	-13305.563559
64	4*4*4	12	-13282.621599	-13305.575908
125	5*5*5	24	-13282.622589	-13305.589997
216	6*6*6	36	-13282.624901	-13305.595252
343	7*7*7	58	-13282.624733	-13305.594642
512	8*8*8	80	-13282.624574	-13305.594563

Table 4.1.5: K-points for Ga_{0.25}Fe_{0.75}N in ZB structure for both LSDA and GGA methods

K_{tot}	K_{mesh}	K_{irred}	$E_{(\text{LSDA})}$ eV	$E_{(\text{GGA})}$ eV
8	2*2*2	2	-11940.957414	-11962.800881
27	3*3*3	5	-11941.160139	-11962.892342
64	4*4*4	8	-11941.204521	-11962.892521
125	5*5*5	14	-11941.171428	-11962.892275
216	6*6*6	20	-11941.171884	-11962.902336
343	7*7*7	30	-11941.170746	-11962.915668
512	8*8*8	40	-11941.168974	-11962.907699
729	9*9*9	55	-11941.169088	-11962.907660

Table 4.1.6: K-points for FeN in ZB structure for both LSDA and GGA methods

K_{tot}	K_{mesh}	K_{irred}	$E_{(LSDA)} \text{ eV}$	$E_{(GGA)} \text{ eV}$
8	2*2*2	3	-2649.891608	-2655.036634
27	3*3*3	5	-2649.924683	-2655.079004
64	4*4*4	10	-2649.934683	-2655.083328
125	5*5*5	14	-2649.936729	-2655.077125
216	6*6*6	22	-2649.938146	-2655.078550
343	7*7*7	30	-2649.937017	-2655.080109
512	8*8*8	43	-2649.936185	-2655.083232
729	9*9*9	55	-2649.935677	-2655.086259

As a result of the total energy versus K_{irred} , figures for all concentrations were performed, figures 4.1-a, b for GaN in wurtzite structure, figures 4.2-a,b for x= 0, figures 4.3-a,b for x= 0.25, figures 4.4-a,b for x= 0.5, figures 4.5-a,b for x= 0.75, and figures 4.6-a,b for x= 1.0.

It is found that the K_{mesh} and K_{irred} which are enough to perform the calculations for LSDA and GGA for all concentrations are summarized in table 4.1.7

Table 4.1.7: The total K_{mesh} and K_{irred} which are sufficient to perform the calculations for $\text{Ga}_{1-x}\text{Fe}_x\text{N}$ in ZB structure.

Concentration (x)	K_{mesh} LSDA	K_{irred} LSDA	K_{mesh} GGA	K_{irred} GGA
0	9*9*9	50	9*9*9	55
0.25	6*6*6	20	8*8*8	40
0.50	6*6*6	36	6*6*6	36
0.75	6*6*6	20	7*7*7	30
1.0	6*6*6	22	9*9*9	55

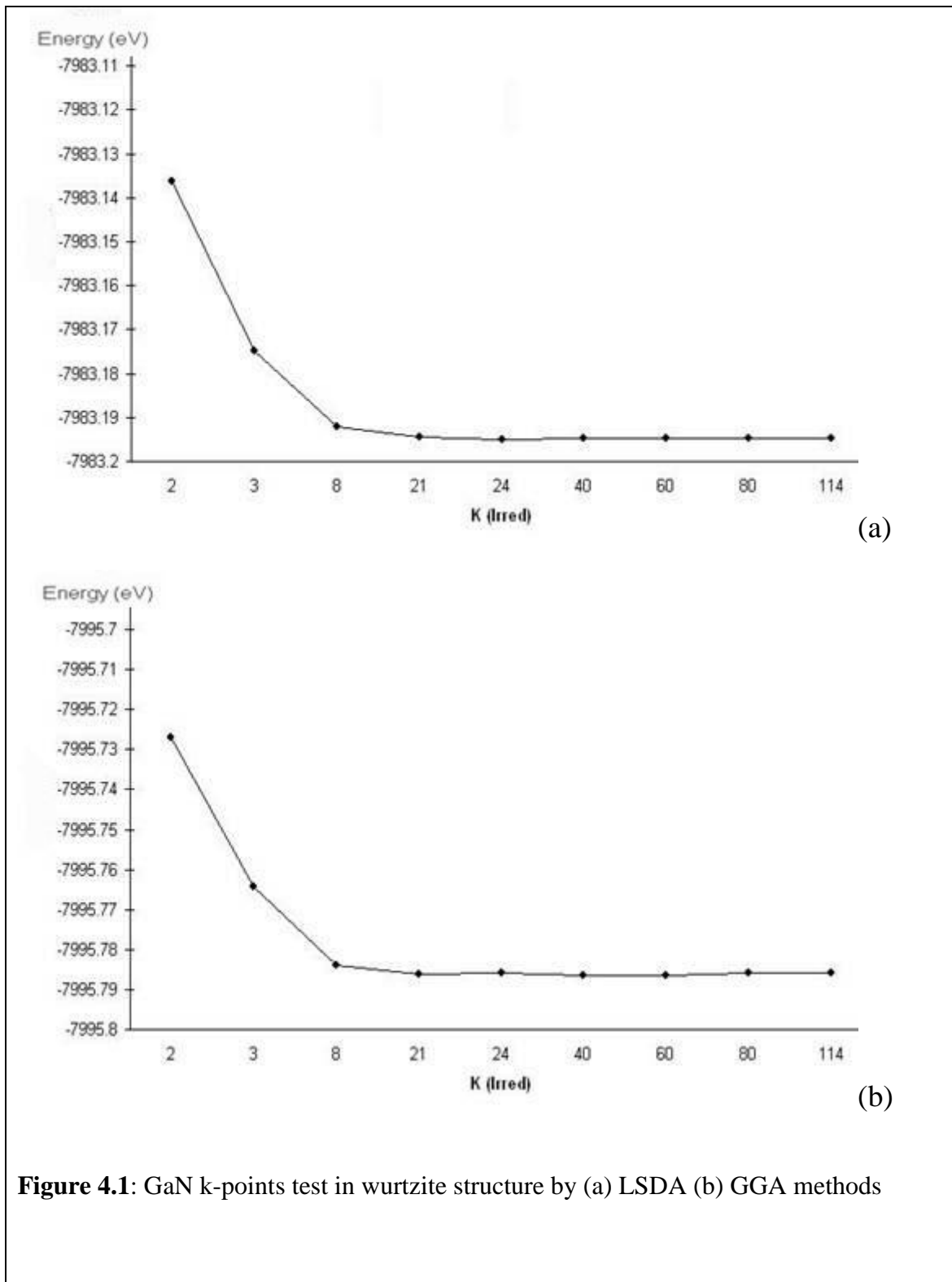


Figure 4.1: GaN k-points test in wurtzite structure by (a) LSDA (b) GGA methods

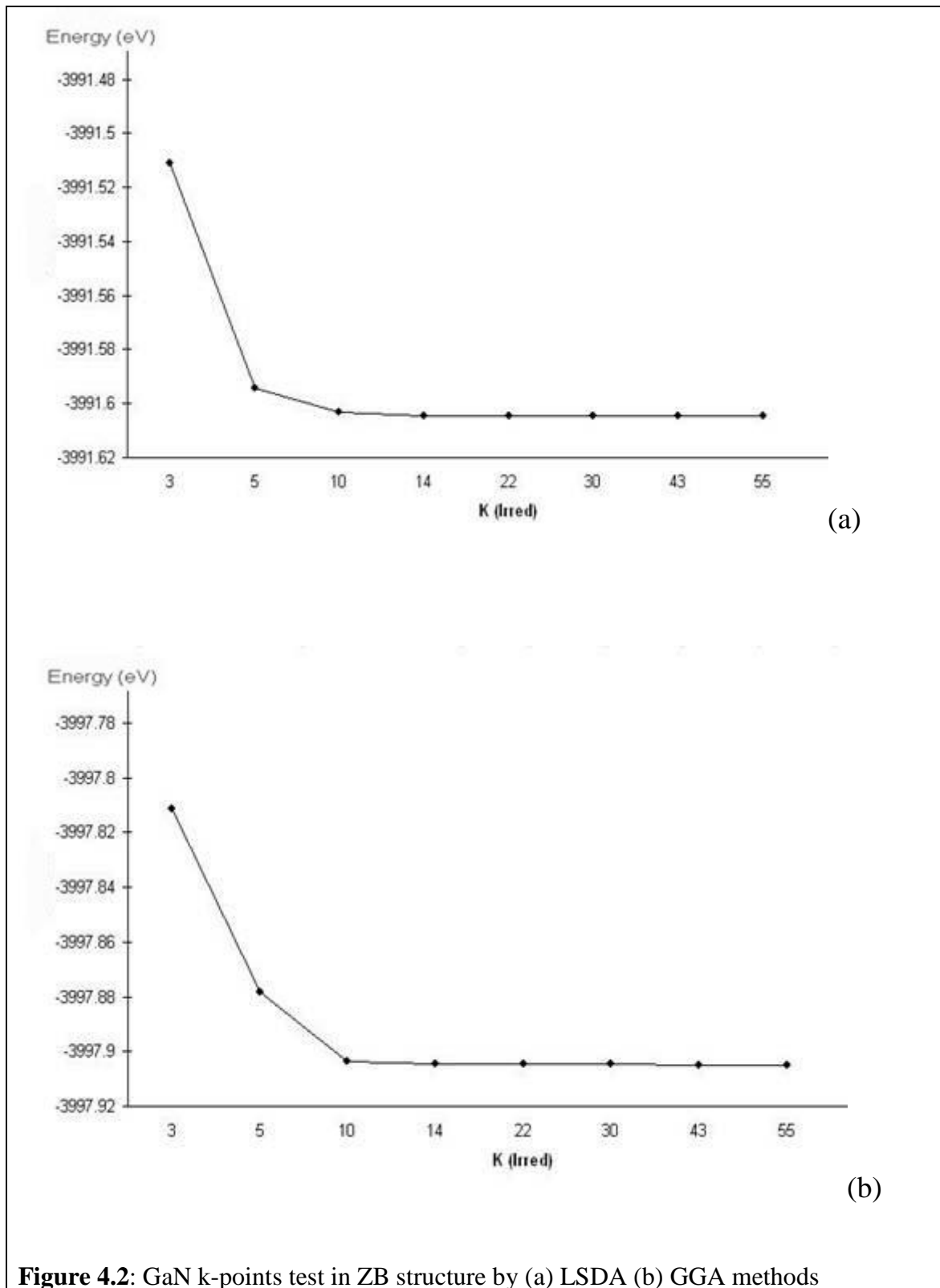


Figure 4.2: GaN k-points test in ZB structure by (a) LSDA (b) GGA methods

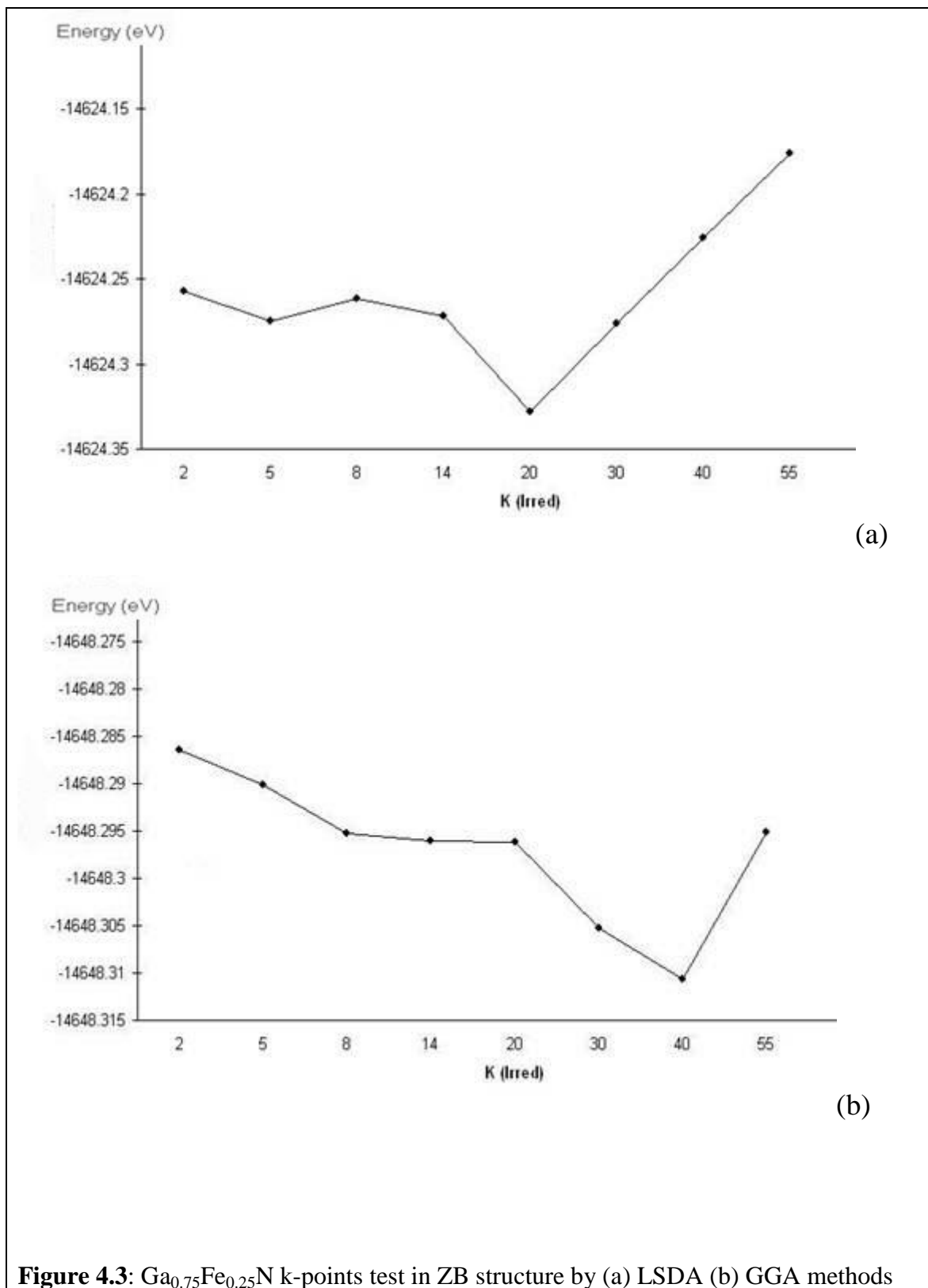


Figure 4.3: Ga_{0.75}Fe_{0.25}N k-points test in ZB structure by (a) LSDA (b) GGA methods

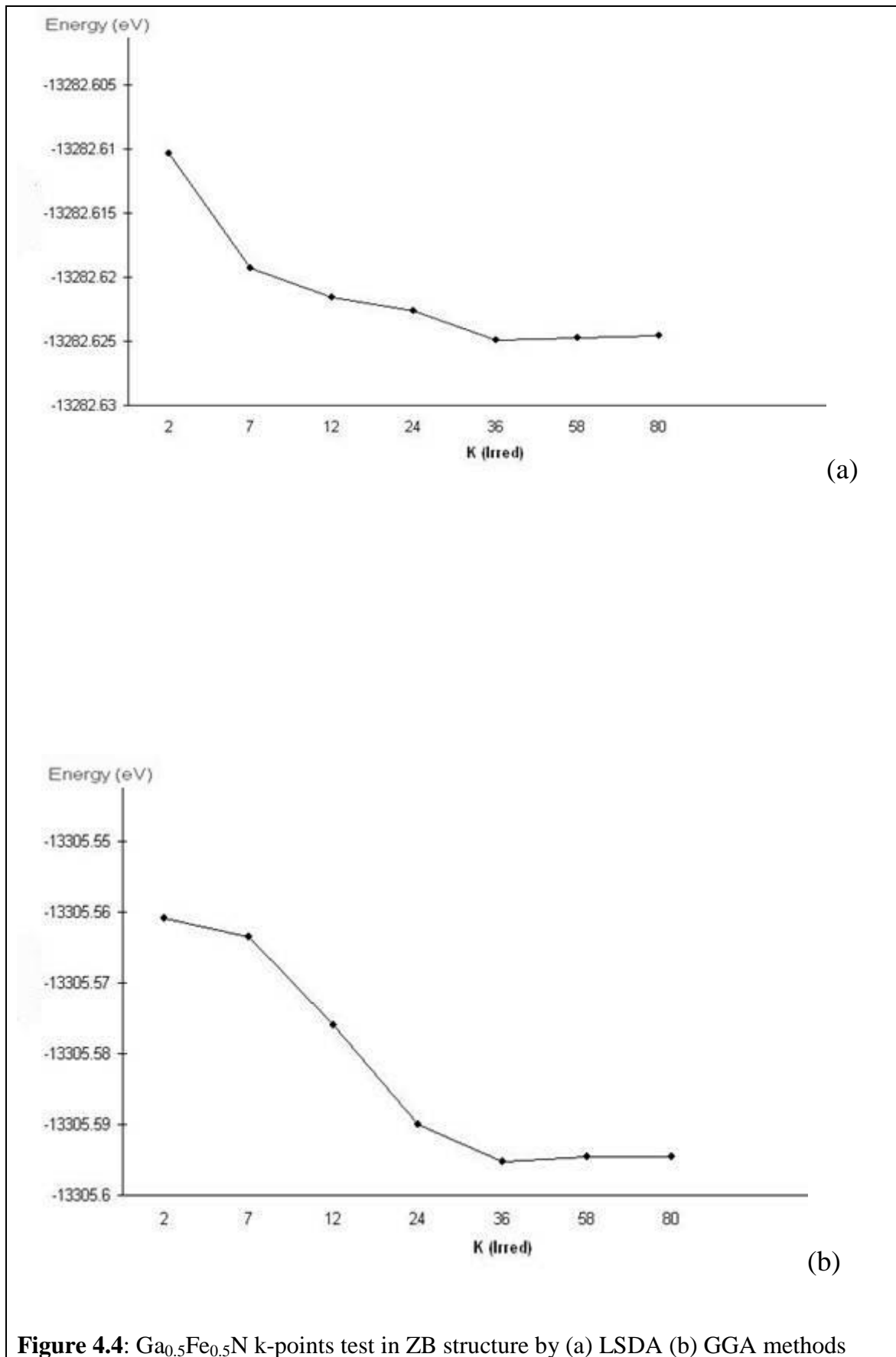
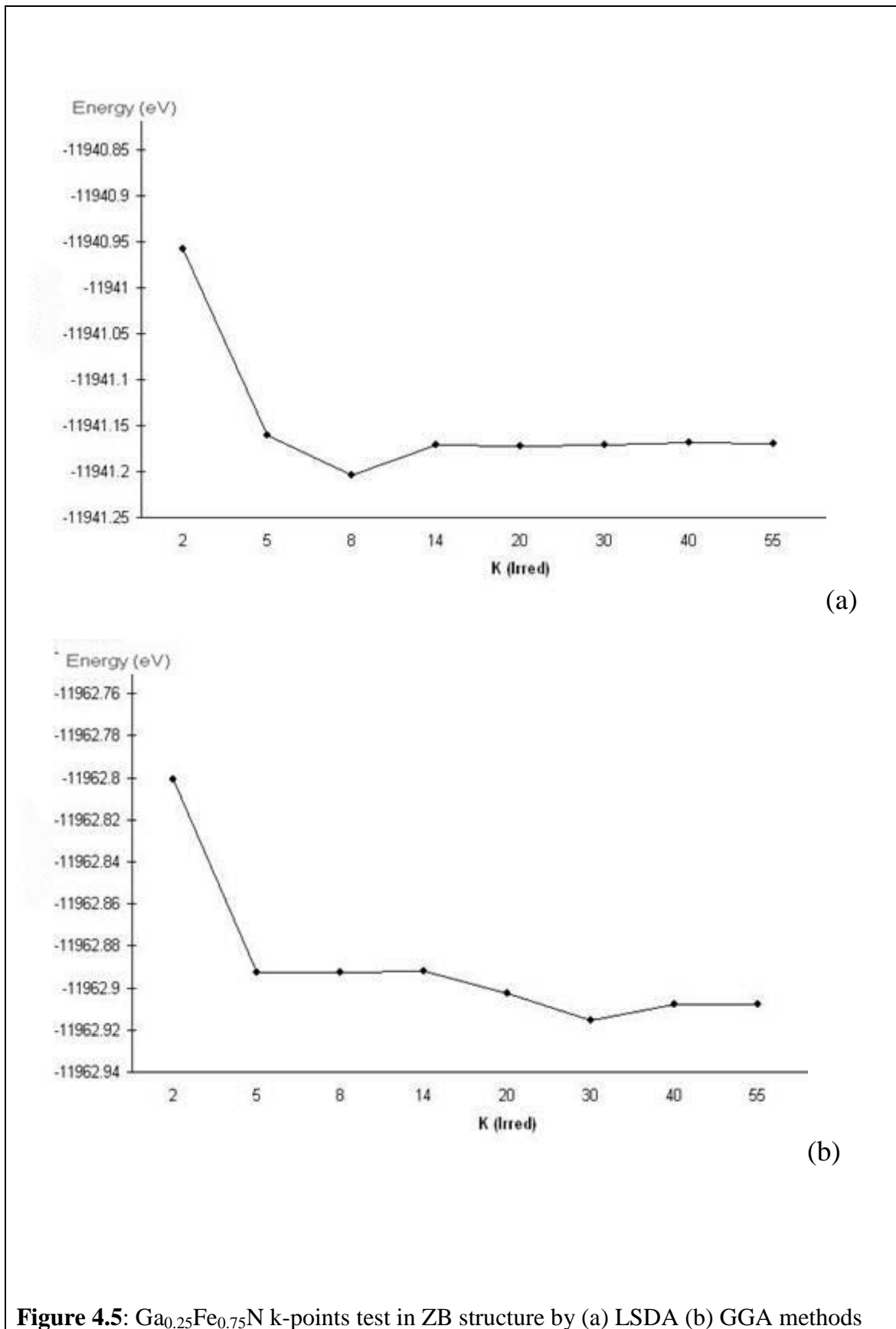


Figure 4.4: Ga_{0.5}Fe_{0.5}N k-points test in ZB structure by (a) LSDA (b) GGA methods



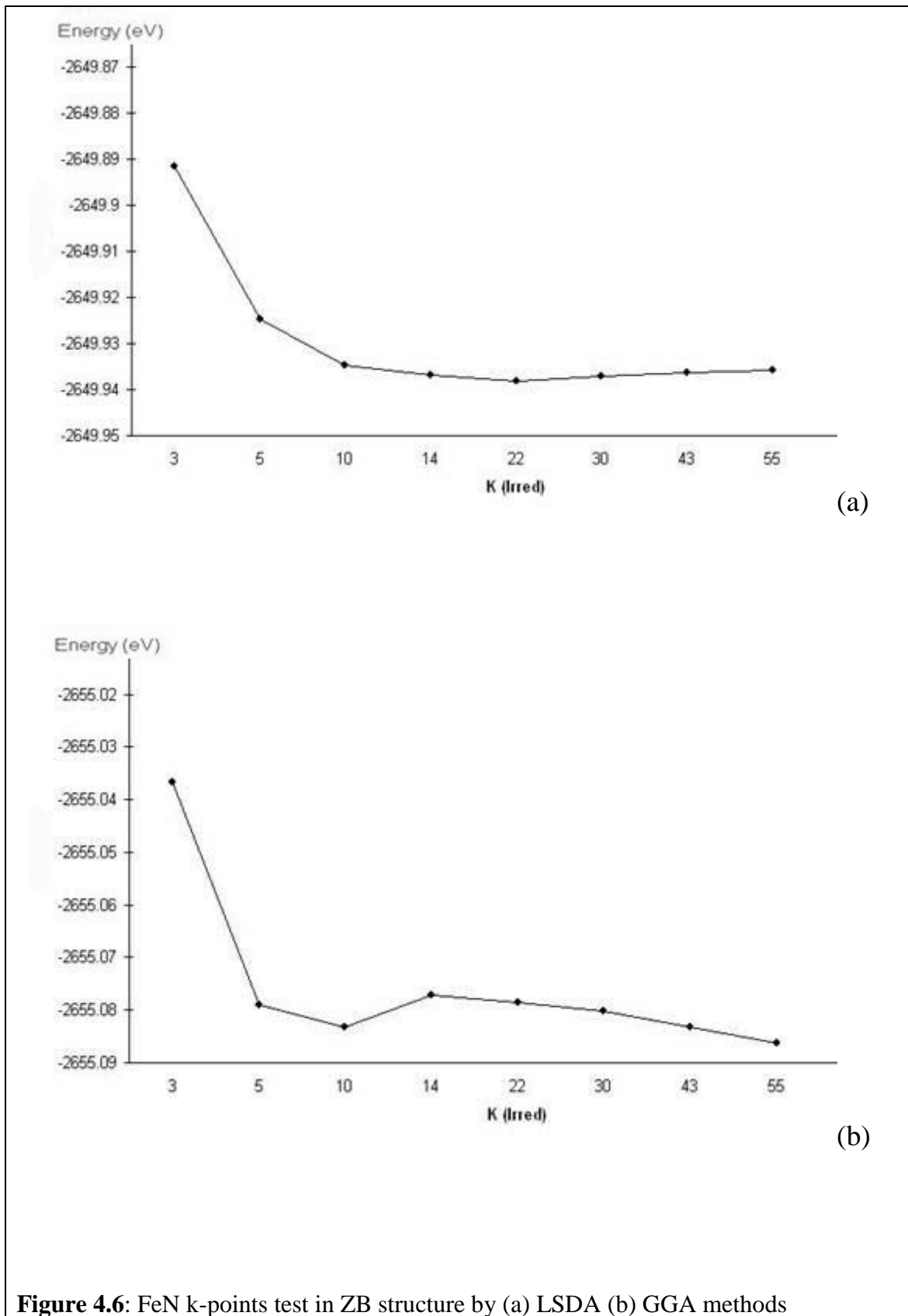


Figure 4.6: FeN k-points test in ZB structure by (a) LSDA (b) GGA methods

4.1.2 $R_{MT} \cdot K_{max}$ Cutoff Test

In this test, the dependence of the total energy on the $R_{MT} \cdot K_{max}$ cutoff is checked. Calculations of the total energy dependence on the cutoff energy were performed using the trial lattice constants mentioned above using the total K_{mesh} and K_{irred} listed in table 4.1.7. The total energy dependence on the $R_{MT} \cdot K_{max}$ cutoff is displayed in table 4.1.8 for GaN in wurtzite structure, and in tables 4.1.9, 4.1.10, 4.1.11, 4.1.12, and 4.1.13 for

$Ga_{1-x}Fe_xN$ for $x = 0, 0.25, 0.50, 0.75, 1.0$ respectively.

Table 4.1.8: $R_{MT} \cdot K_{max}$ cutoff test for GaN in Wurtzite structure

$R_{MT} \cdot K_{max}$	ENE^{LSDA} (eV)	ENE^{GGA} (eV)
5.5	-7982.897232	-7995.281924
6.0	-7983.069898	-7995.376139
6.5	-7983.154504	-7995.736120
7.0	-7983.194805	-7995.605045
7.5	-7983.212897	-7995.802463
8.0	-7983.250621	-7995.811514
8.5	-7983.224170	-7995.815453
9.0	-7983.255378	-7995.817163
9.5	-7983.255953	-7995.817858
10	-7983.226373	-7995.816455

Table 4.1.9: $R_{MT}.K_{max}$ cutoff test for $Ga_{1-x}Fe_xN$ ($x=0$) in ZB structure

$R_{MT}.K_{max}$	ENE^{LSDA} (eV)	ENE^{GGA} (eV)
6.0	-3991.519489	-3997.820092
6.5	-3991.581348	-3997.866867
7.0	-3991.604596	-3997.904882
7.5	-3991.614997	-3997.900217
8.0	-3991.604900	-3997.904758
8.5	-3991.606922	-3997.900584
9.0	-3991.607774	-3997.907627
9.5	-3991.608127	-3997.922884
10	-3991.606241	-3997.910834

Table 4.1.10: $R_{MT}.K_{max}$ cutoff test for $Ga_{1-x}Fe_xN$ ($x=0.25$) in ZB structure

$R_{MT}.K_{max}$	ENE^{LSDA} (eV)	ENE^{GGA} (eV)
6.0	-14623.033448	-14648.002036
6.5	-14623.228752	-14648.202174
7.0	-14623.328091	-14648.310651
7.5	-14623.471130	-14648.448737
8.0	-14623.386255	-14648.364534
8.5	-14623.396290	-14648.597342

Table 4.1.11: $R_{MT}.K_{max}$ cutoff test for $Ga_{1-x}Fe_xN$ ($x=0.50$) in ZB structure :

$R_{MT}.K_{max}$	ENE^{LSDA} (eV)	ENE^{GGA} (eV)
6.0	-13282.109997	-13305.073322
6.5	-13282.453101	-13305.418661
7.0	-13282.624901	-13305.595252
7.5	-13282.698250	-13305.677740
8.0	-13282.735557	-13305.716147
8.5	-13282.682542	-13305.716141

Table 4.1.12: $R_{MT}.K_{max}$ cutoff test for $Ga_{1-x}Fe_xN$ ($x=0.75$) in ZB structure

$R_{MT}.K_{max}$	ENE^{LSDA} (eV)	ENE^{GGA} (eV)
6.0	-11940.447632	-11962.666567
6.5	-11940.934697	-11962.786623
7.0	-11941.171884	-11962.915668
7.5	-11941.351130	-11963.063385
8.0	-11941.369313	-11963.105281
8.5	-11941.170746	-11963.105571

Table 4.1.13: $R_{MT}.K_{max}$ cutoff test for $Ga_{1-x}Fe_xN$ ($x=1.0$) in ZB structure

$R_{MT}.K_{max}$	ENE^{LSDA} (eV)	ENE^{GGA} (eV)
6.0	-2649.703275	-2654.845913
6.5	-2649.861953	-2655.005958
7.0	-2649.937017	-2655.080109
7.5	-2649.975278	-2655.124121
8.0	-2649.993606	-2655.145444
8.5	-2649.976427	-2655.140529

As a result of the total energy versus $R_{MT}.K_{max}$ cutoff, plot is shown in Figures 4.6a,b for GaN in wurtzite structure. It is found that the $R_{MT}.K_{max}$ cutoff of 9.5 is sufficient to perform the calculations for both LSDA, and GGA approximation methods,

while tables 4.1.8 to 4.1.13 show the $R_{MT}.K_{max}$ cutoff of

$Ga_{1-x}Fe_xN$ for all concentrations that have been studied and then plotted in the figures 4.7 a, b to 4.12 a, b.

The values of the $R_{MT}.K_{max}$ cutoff of $Ga_{1-x}Fe_xN$ at equilibrium are listed finally in table 4.1.14 .

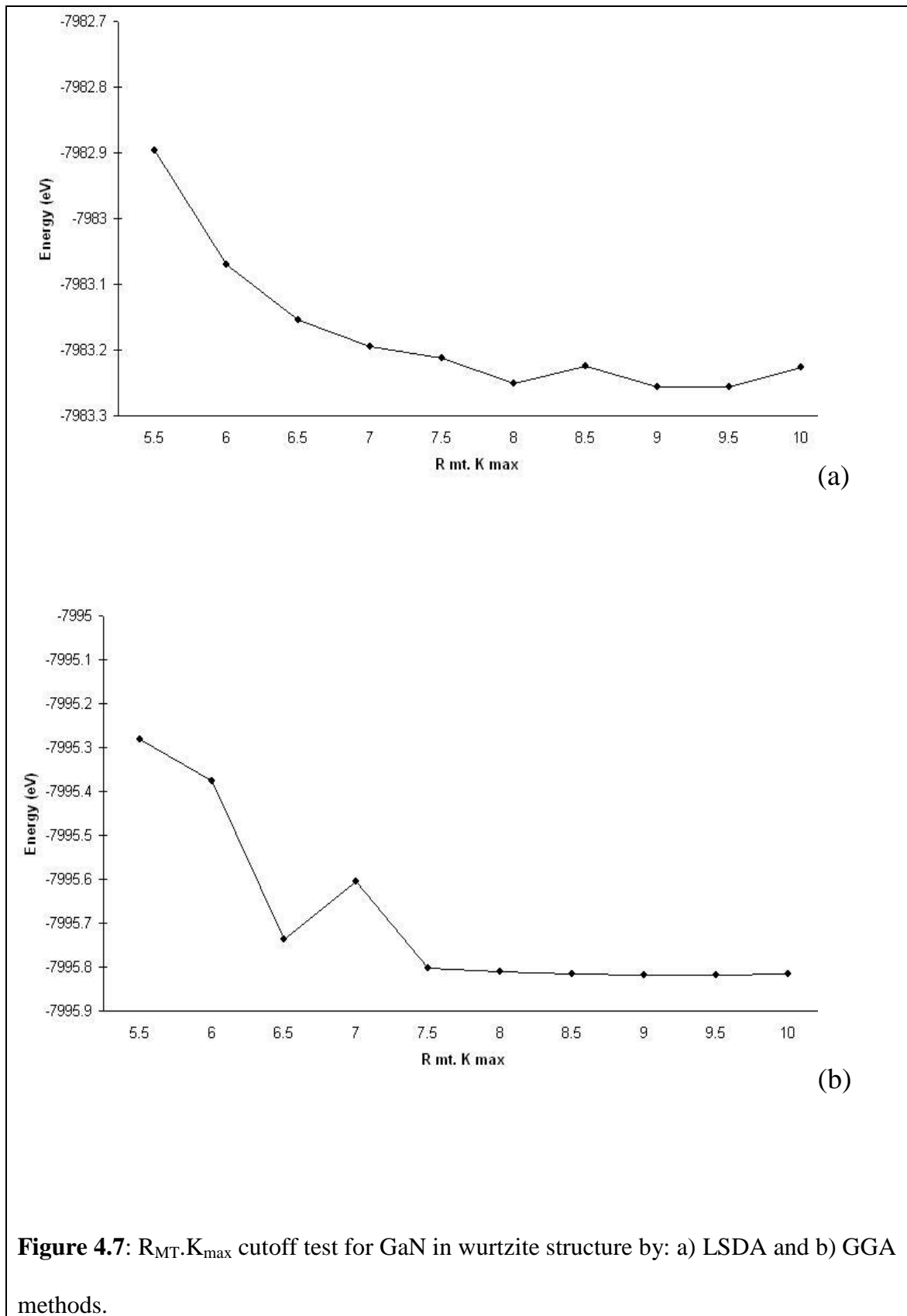
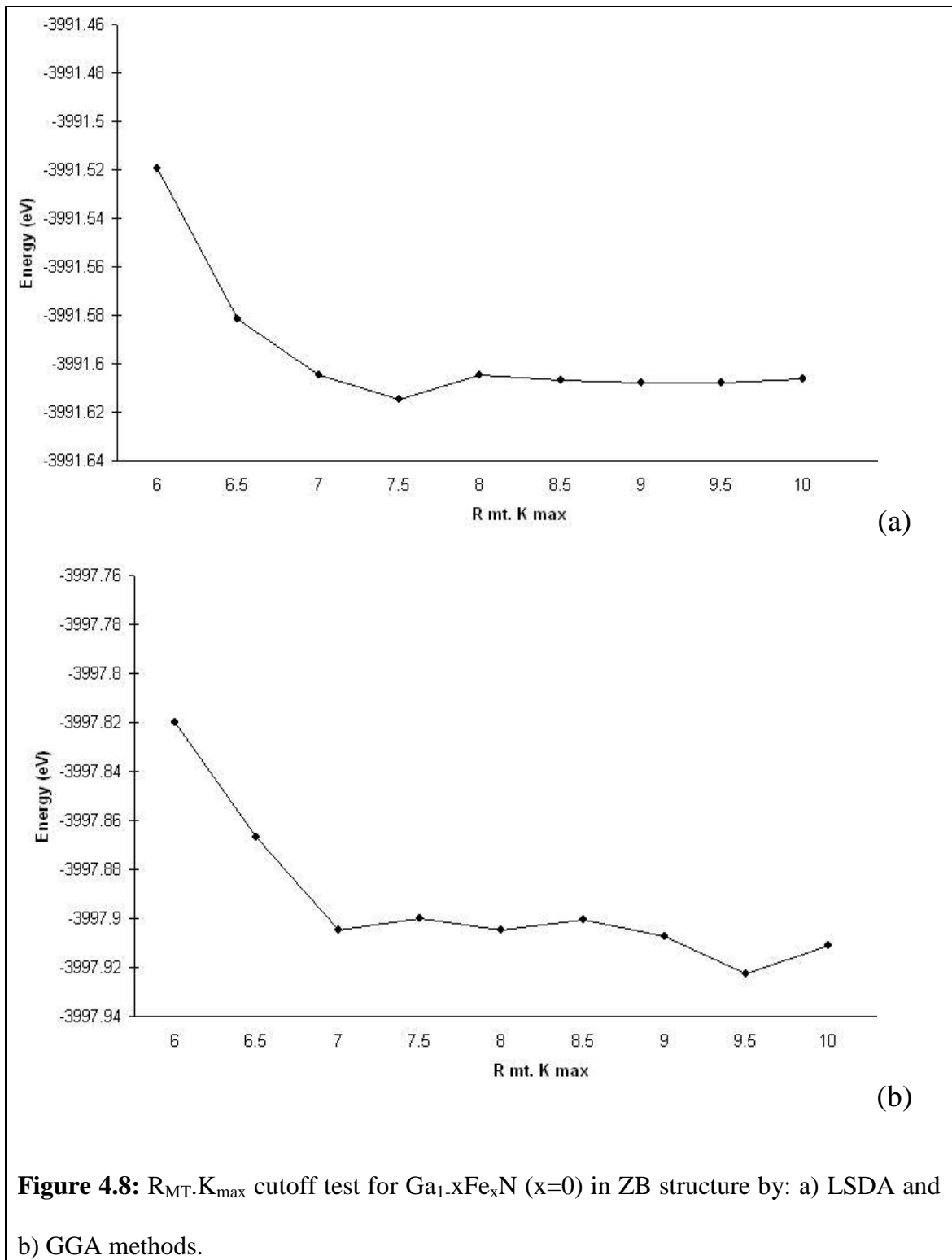


Figure 4.7: $R_{MT} \cdot K_{max}$ cutoff test for GaN in wurtzite structure by: a) LSDA and b) GGA methods.



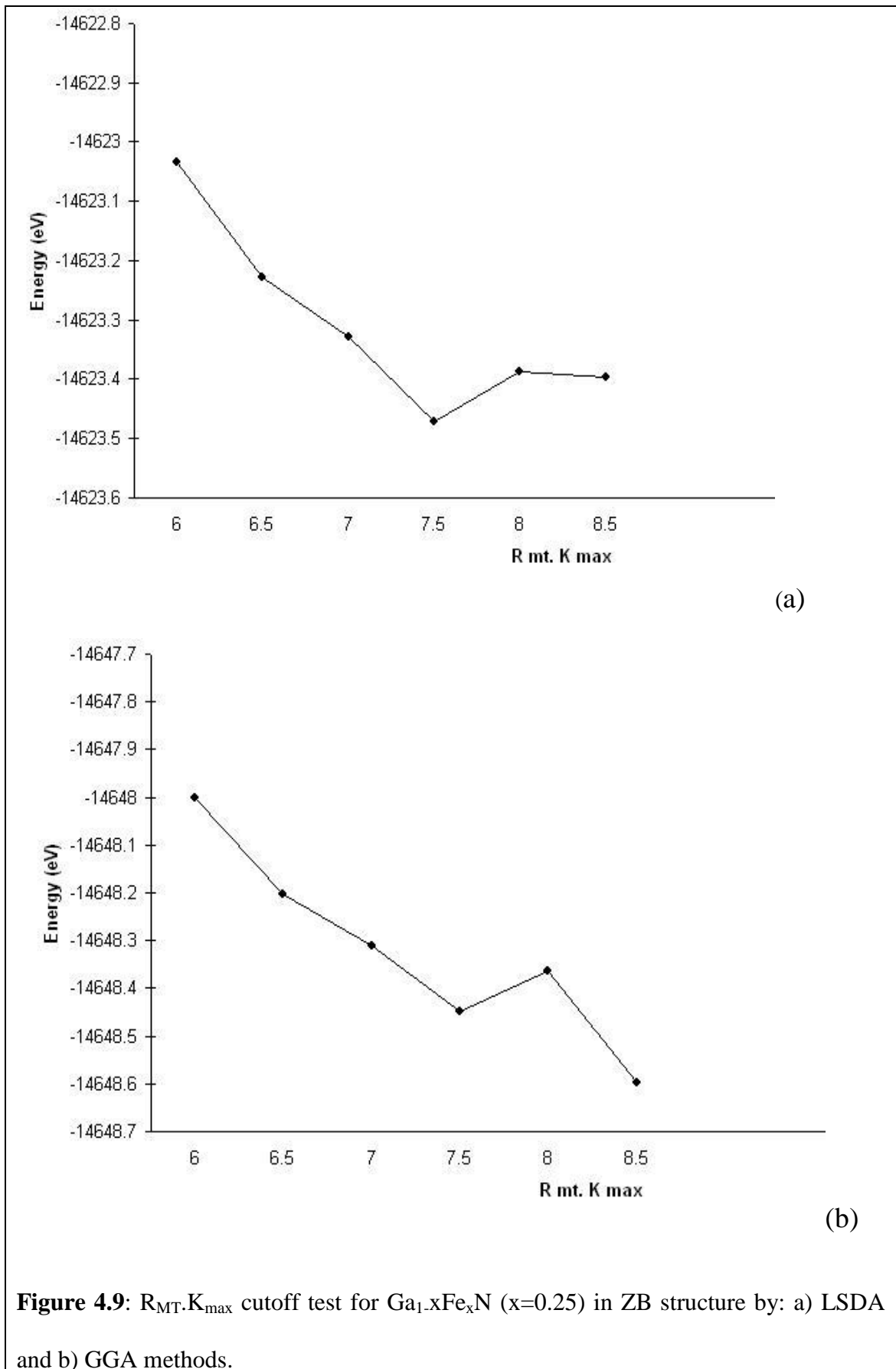


Figure 4.9: $R_{MT}.K_{max}$ cutoff test for $Ga_{1-x}Fe_xN$ ($x=0.25$) in ZB structure by: a) LSDA and b) GGA methods.

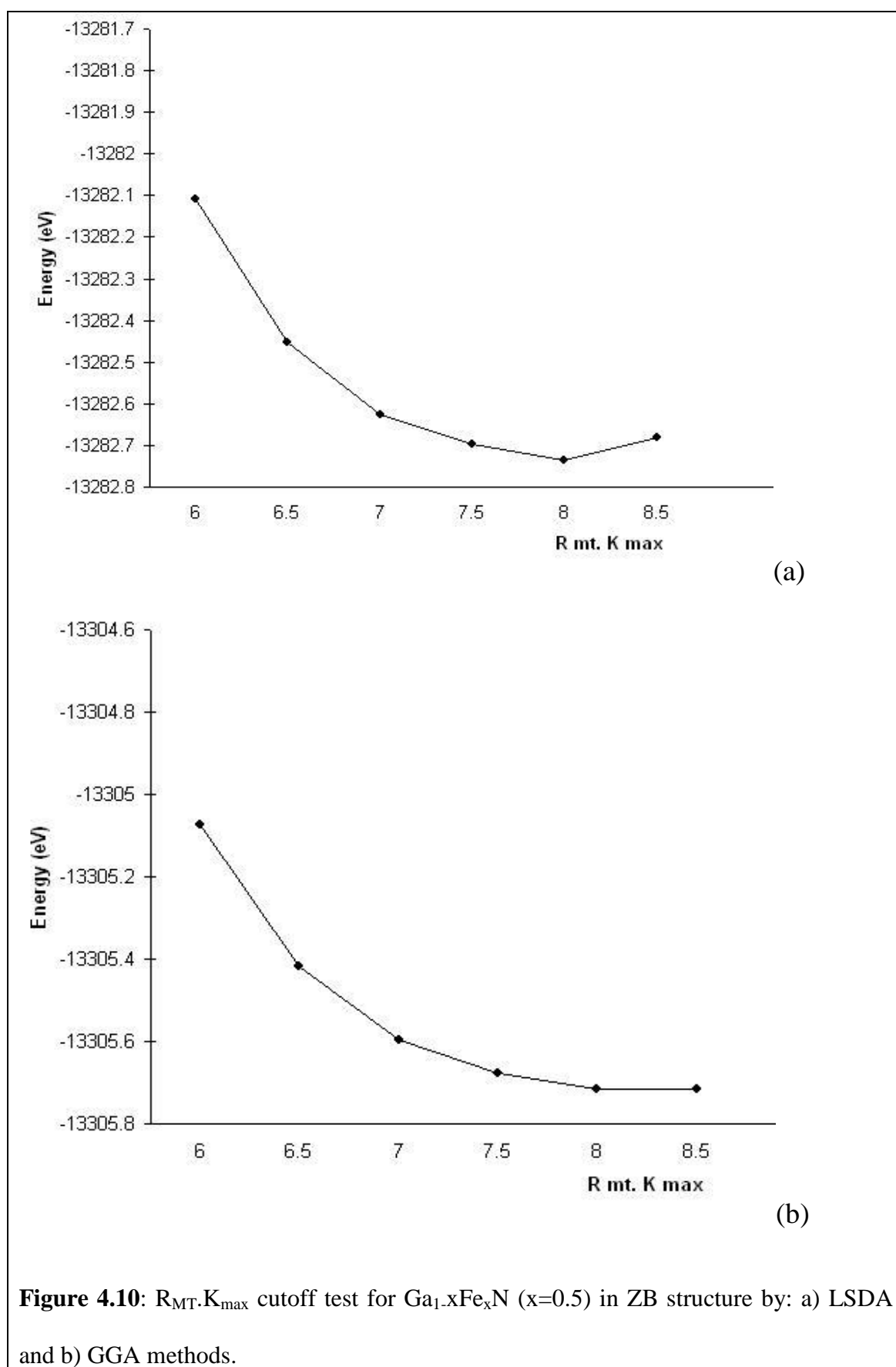


Figure 4.10: $R_{MT}.K_{max}$ cutoff test for $Ga_{1-x}Fe_xN$ ($x=0.5$) in ZB structure by: a) LSDA and b) GGA methods.

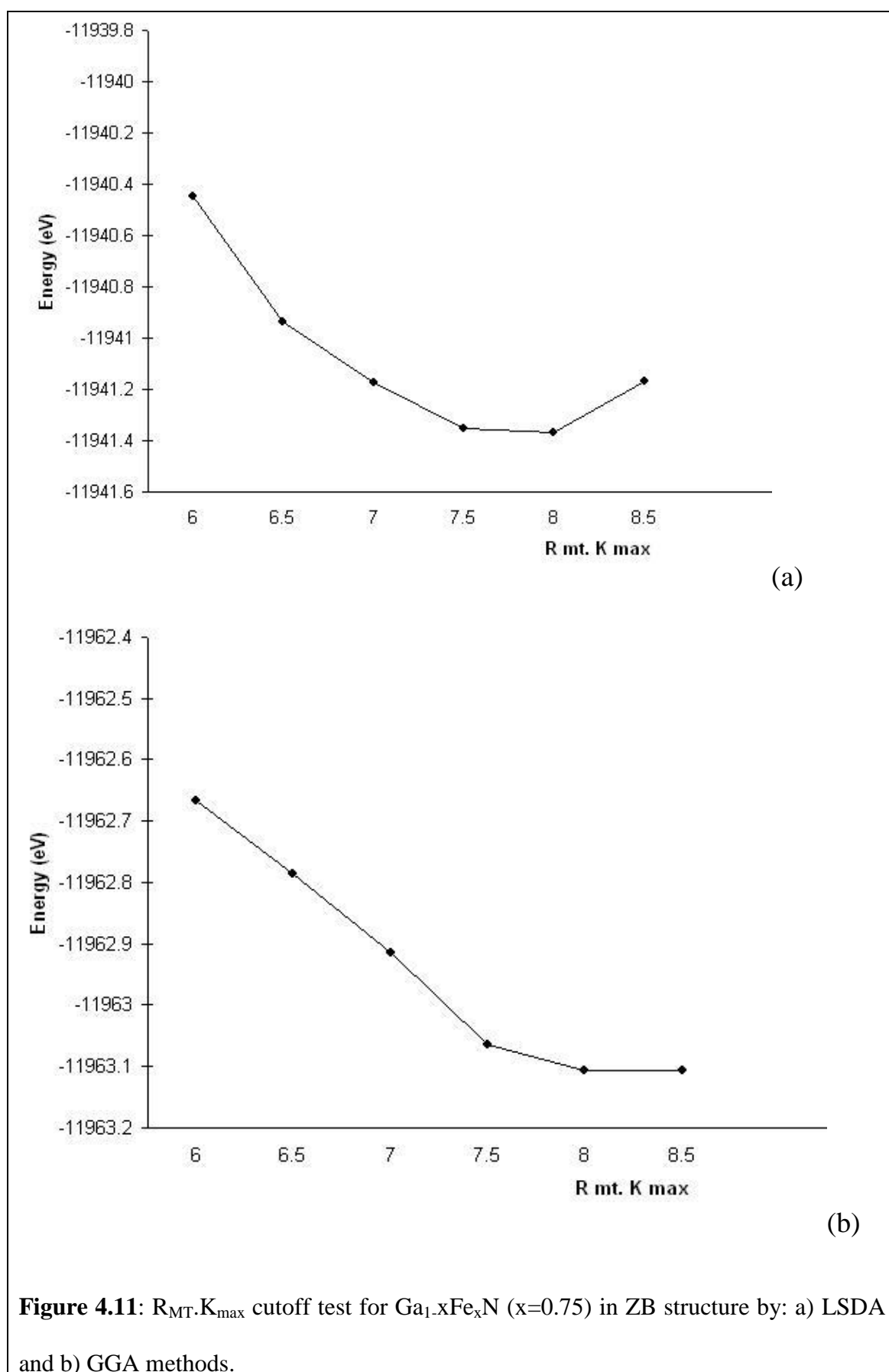


Figure 4.11: $R_{MT}.K_{max}$ cutoff test for $Ga_{1-x}Fe_xN$ ($x=0.75$) in ZB structure by: a) LSDA and b) GGA methods.

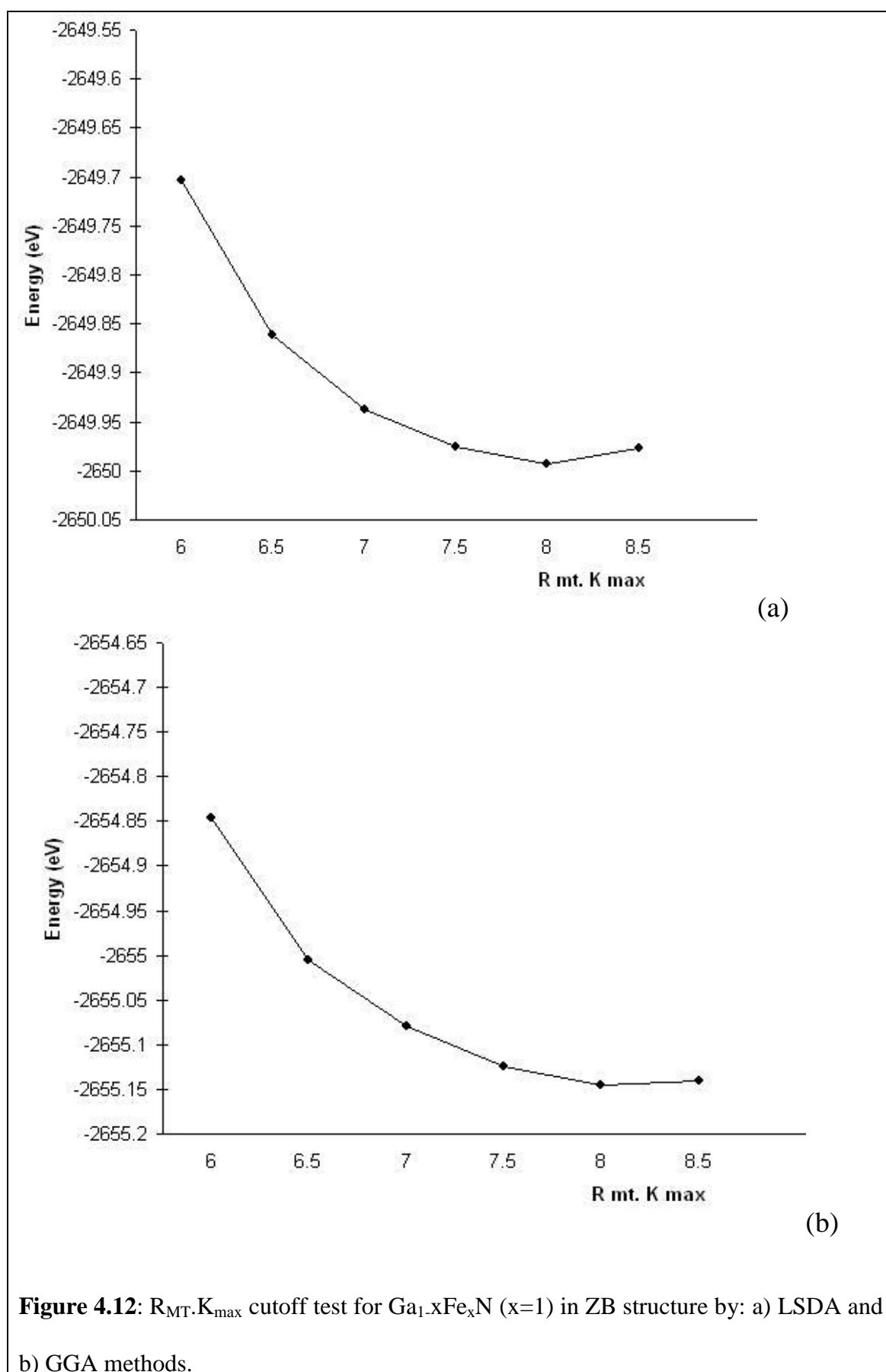


Figure 4.12: $R_{MT} \cdot K_{max}$ cutoff test for $Ga_{1-x}Fe_xN$ ($x=1$) in ZB structure by: a) LSDA and b) GGA methods.

Table 4. 1. 14: $R_{MT} \cdot K_{max}$ for $Ga_{1-x}Fe_xN$ in ZB structure using LSDA and GGA.

Concentration x	$R_{MT} \cdot K_{max}^{LSDA}$	$R_{MT} \cdot K_{max}^{GGA}$
0	9.5	9.5
0.25	7.5	7.5
0.50	8	8
0.75	8	8
1	8	8

4.1.3 Optimization

Most of the complex structures have free internal structural parameters, which can be chosen from experiment.

Some suggestion about how to do the optimization in WIEN2K:

- 1) Start the calculations by generating struct.file using arbitrary parameters.
- 2) Initialize your file by introducing $R_{MT} \cdot K_{max}$, G_{max} , and number of k-points.
- 3) Run SCF cycle.
- 4) Choose optimize (V, c/a) job, then x-optimize and choose vary volume with constant a, b, c for optimizing volume to find the lattice constant, bulk modulus, and pressure first derivative or choose vary c/a with constant volume to find the ratio c/a of wurtzite structure, in both cases we must enter volume difference values like (-8, -4, -2, 2, 4, 8) %.

- 5) After doing this job we plot energy curves versus volume or c/a
- 6) For wurtzite structure we will find the values of a and c for each energy value in files carrying name of the job and the difference in volume you have chosen, from these values c/a vs. energy and using polyfit program we can find the value of c/a at equilibrium volume.

4.2 Structural properties

4.2.1 GaN in Wurtzite Structure

The optimal values of c/a ratio and the internal parameter, u , at a specific volume (V), were determined as follows.

First, the total energy is calculated at several values of c/a ratio at fixed volume and a guessed value of u . The obtained results are then fitted to parabola to find $(c/a)_{eq}$. Second, the optimal value of u similarly determined, using the obtained $(c/a)_{eq}$. Third, the first step is repeated to ensure that the $(c/a)_{eq}$ determination was properly done. It has been found that $(c/a)_{eq}$ is V -independent. The value of c/a at equilibrium volume using LSDA is 1.632494 (table 4.2.1) and using GGA is 1.625391 (table 4.2.2).

Table 4. 2. 1: c/a ratio of GaN in wurtzite structure using LSDA approximation method.

a=b(a. u.)	c(a. u.)	c/a	Energy (eV)
5.990403	9.779340	1.632494	-7983.022205
6.072510	9.516780	1.567191	-7983.035370
6.030910	9.648510	1.599843	-7983.038093
5.990403	9.779340	1.632494	-7983.038470
5.951020	9.909300	1.665143	-7983.036757
5.912630	10.038410	1.697791	-7983.033192
5.838710	10.294180	1.763092	-7983.021103

Table 4. 2. 2: c/a ratio of GaN in wurtzite structure using GGA approximation method.

a=b(a. u.)	c(a. u.)	c/a	Energy (eV)
6.028230	9.798230	1.625391	-7995.610637
6.110820	9.535170	1.560375	-7995.627410
6.068960	9.667150	1.592884	-7995.631557
6.028230	9.798230	1.625391	-7995.633248
5.988570	9.928450	1.657900	-7995.632679
5.949930	10.957810	1.690408	-7995.630107
5.875550	10.314080	1.755424	-7995.619592

The value of the internal parameter (u) which determines the position of the atom in the unit cell is calculated, using different values of u, and running SCF calculation for each value and getting the value of u at equilibrium energy. Table 4.2.3 shows the values of u and energies corresponding to each value for both LSDA and GGA methods giving values of u=3.8 and u= 3.75 respectively.

Table 4.2.3: u-test for GaN in wurtzite structure using LSDA and GGA methods.

u	$E_{(LSDA)}$ eV	$E_{(GGA)}$ eV
3.6	-7983.189137	-7995.781800
3.7	-7983.193953	-7995.603886
3.73	-7983.194369	-7995.604739
3.74	-7983.194701	-7995.604918
3.75	-7983.194742	-7995.605045
3.8	-7983.194554	-7995.604944
3.9	-7983.192111	-7995.601628

After finding the values of c/a, a and c will be found by plotting the energy versus volume, fitting the results with Murnaghan equation of state, the values of equilibrium volume, bulk modulus, and its first derivative are calculated.

The volume of a unit cell for wurtzite structure is given by:

$$V = \frac{\sqrt{3}}{2} a^2 c \quad \text{or} \quad V = \frac{\sqrt{3}}{2} a^3 (c/a) \quad \dots\dots\dots (1)$$

Substituting the volume from fig. 4.13 and c/a in equation (1) we can find the values of (a) and then (c).

a) For LSDA, $V= 299.2129$ (a. u)³, $c/a= 1.632494$,

$$a=3.153\text{\AA}, c=5.148\text{\AA}$$

b) For GGA, $V=317.639$ (a. u)³, $c/a= 1.625391$,

$$a= 3.22 \text{ \AA}, c= 5.23\text{\AA}.$$

Table 4.2.4: Lattice parameters, Bulk modulus, and pressure first derivative of GaN in wurtzite structure using LSDA and GGA methods compared with other theoretical calculations.

Parameter	Magnitude	reference	method
a (Å)	3.153	Present	LSDA FP-LAPW
	3.22	Present	GGA FP-LAPW
	3.155	[12]	LDA FP-LAPW
	3.224	[12]	GGA FP-LAPW
	3.221	[13]	LDA FP-LAPW
	3.18	[15]	LDA ab initio (Pseudo)
	3.25	[15]	GGA ab initio (Pseudo)}
	3.154	[60]	LDA FP-LAPW
	3.15	[60]	GGA FP-LAPW
	3.163	[11]	LDA FP-LAPW
	3.226	[11]	GGA FP-LAPW
c/a	3.19	[61]	Experiment
	1.632494	Present	LSDA FP-LAPW
	1.62539	Present	GGA FP-LAPW
	1.633	[12]	LDA FP-LAPW
	1.628	[12]	GGA FP-LAPW
	1.616	[13]	LDA FP-LAPW

	1.63	[15]	LDA ab initio (Pseudo)
	1.63	[15]	GGA ab initio (Pseudo)
	1.628	[60]	LDA FP-LAPW
	1.626	[60]	GGA FP-LAPW
	1.704	[11]	LDA FP-LAPW
	1.734	[11]	GGA FP-LAPW
	1.627	[61]	Experiment
B (GPa)	201.96	Present	LSDA FP-LAPW
	172.73	Present	GGA FP-LAPW
	205.42	[12]	LDA FP-LAPW
	172.38	[12]	GGA FP-LAPW
	176.54	[13]	LDA FP-LAPW
	194.66	[15]	LDA ab initio (Pseudo)
	167.07	[15]	GGA ab initio (Pseudo)
	203.13	[60]	LDA FP-LAPW
	171.52	[60]	GGA FP-LAPW
	208.3	[11]	LDA FP-LAPW
	172.4	[11]	GGA FP-LAPW
	188-245	[61]	Experiment
B`	4.53	Present	LSDA FP-LAPW
	4.317	Present	GGA FP-LAPW
	4.37	[12]	LDA FP-LAPW
	5.23	[12]	GGA FP-LAPW
	4.37	[13]	LDA FP-LAPW
	4.43	[15]	LDA ab initio (Pseudo)
	4.16	[15]	GGA ab initio (Pseudo)
	4.58	[60]	LDA FP-LAPW
	3.83	[60]	GGA FP-LAPW
	5.79	[11]	LDA FP-LAPW
	4.86	[11]	GGA FP-LAPW

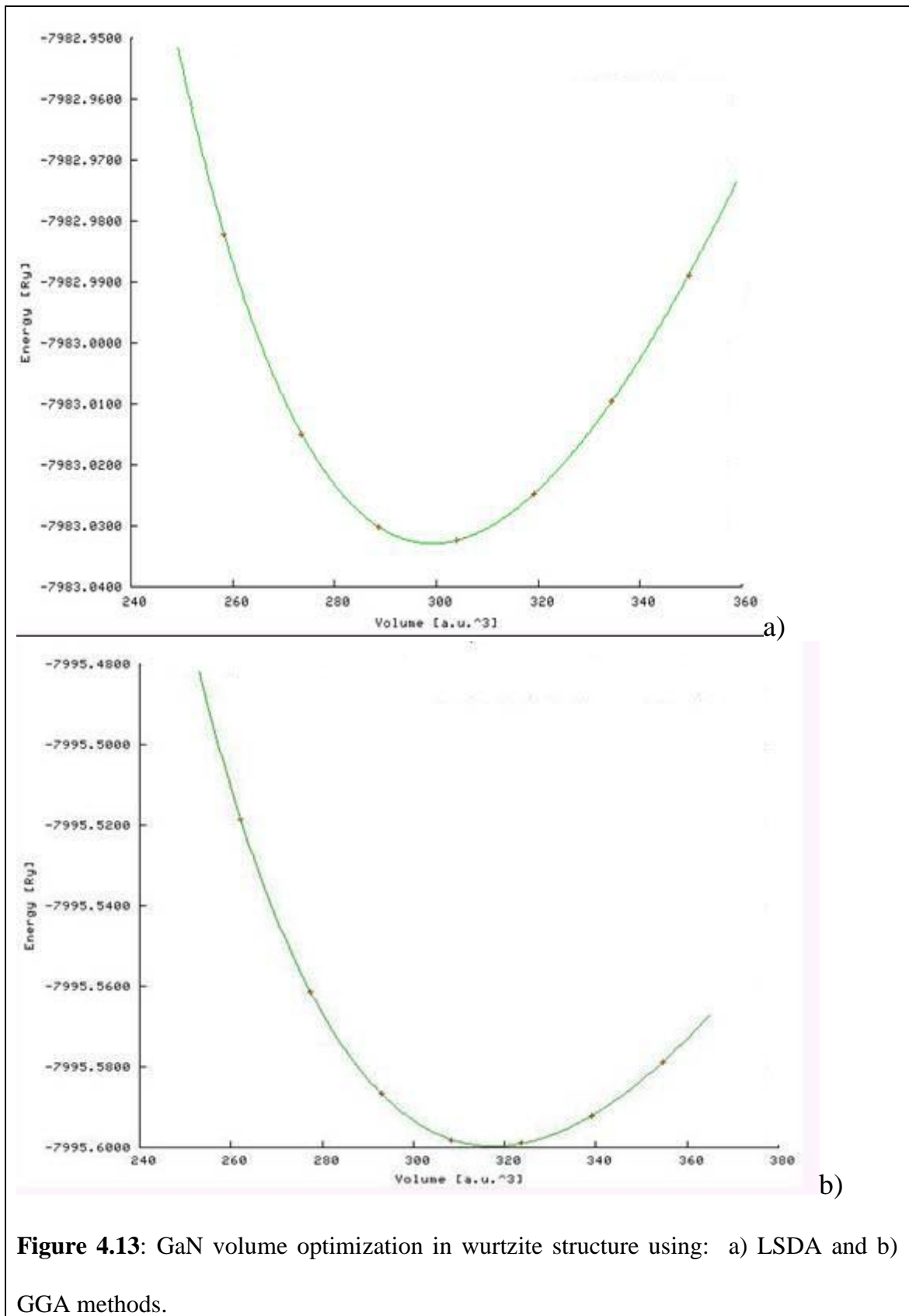


Figure 4.13: GaN volume optimization in wurtzite structure using: a) LSDA and b) GGA methods.

4.2.2 Ga_{1-x}Fe_xN Zincblende Structure (ZB)

4.2.2.1 x=0 (GaN compound)

In (ZB) structure the same way is used to find the lattice constant, the number of K-points for Ga_{1-x}Fe_xN where x=0 is 729 with reduced K_{irred}= 50 for LSDA and K_{irred}= 55 for GGA and matrix of 9×9×9, the Ga atom sets at (0, 0, 0) a.u, while N atom sets at (0.25, 0.25, 0.25) a.u positions, and for both LSDA, and GGA R_{MT}K_{max}=9.5, G=14.

The volume of the unit cell for Zinc-Blende (FCC) is $V = \frac{a^3}{4}$

So,

$$a = (4*V)^{1/3} \dots\dots\dots(1)$$

Using equation (1) and substitute V from the graphs in Fig. 4.14 we get:

a- $V = 150.5812 \text{ (a. u.)}^3$, $a = 4.469 \text{ \AA}^\circ$, using LSDA method.

b- $V = 159.1776 \text{ (a. u.)}^3$, $a = 4.552 \text{ \AA}^\circ$, using GGA method.

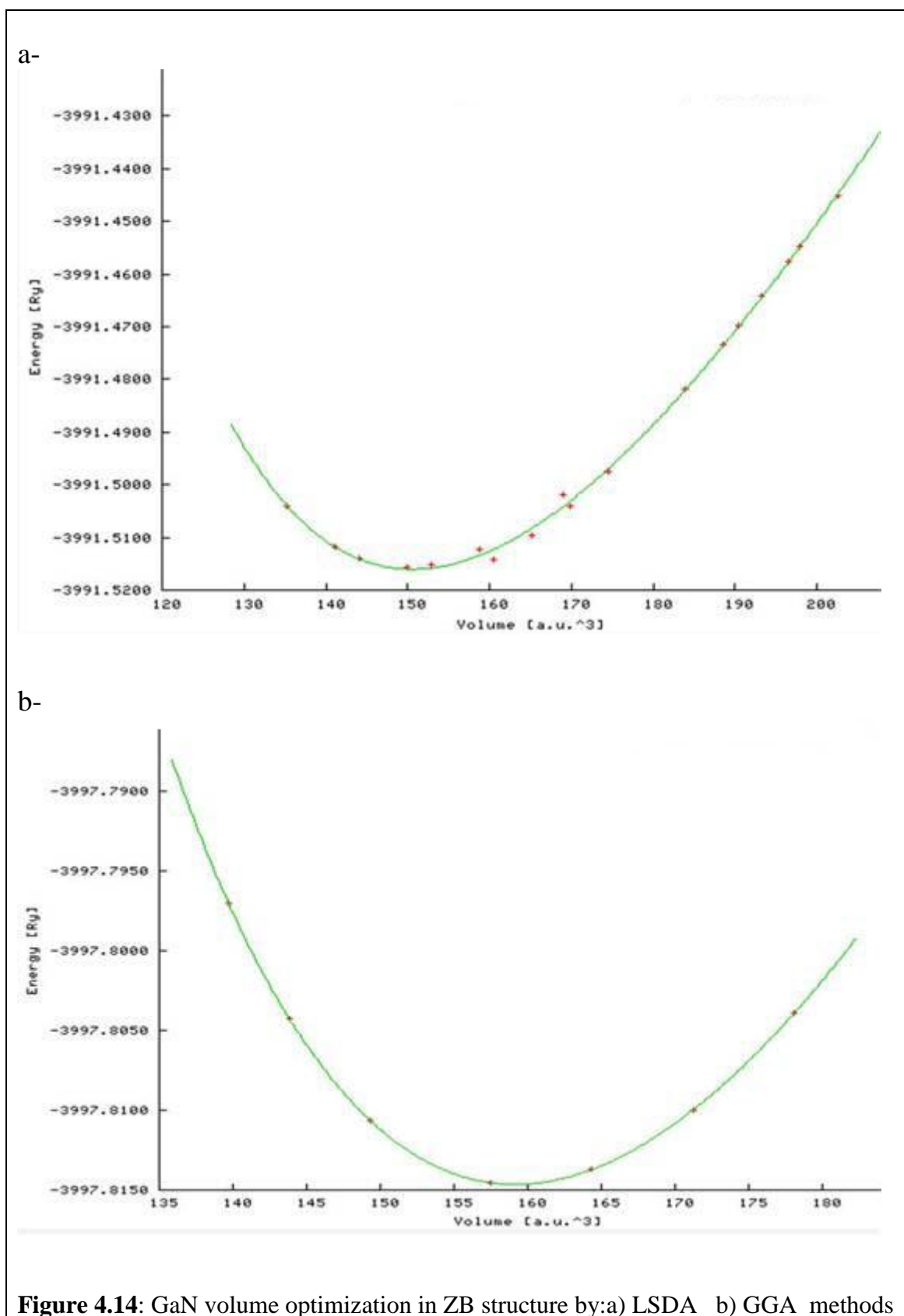


Table 4.2.5: Lattice parameters, Bulk modulus, and pressure first derivative of GaN in ZB structure using LSDA and GGA approximations compared with other theoretical and experimental results

Compound	Method	a (Å)	B (GPa)	B'
GaN (Or Ga _{1-x} Fe _x N, with x=0)	LSDA	4.476 ^a	188.3487 ^a	4.0696 ^a
	GGA	4.557 ^a	171.1114 ^a	4.3478 ^a
	LDA	4.463 ^b ,	204 ^b ,	4.68 ^b ,
		4.4738 ^c ,	205.38 ^d	4.8 ^d
		4.475 ^d ,	205.3 ^f ,	4.29 ^f ,
	4.5 ^e ,	203.6566 ^g	4.6835 ^g	
	4.4637 ^f ,			
	4.463 ^g ,			
GGA	4.553 ^b ,	179.2 ^b	3.57 ^b ,	
4.4794 ^c ,	,173.95 ^f	3.75 ^f		
4.556 ^f , 4.553 ^g	179.18 ^g	3.569 ^g		
4.552 ^h	175.32 ^h	3.51 ^h		
Pseudo potential-LDA	4.5 ⁱ			
Pseudo potential-LDA &GGA	LDA	4.50 ^j	194.4 ^j	4.42 ^j
	GGA	4.55 ^k	162 ^k	4.53 ^k
	GGA	4.59 ^j	165.59 ^j	4.24 ^j
Exp.	4.52 ^l , 4.5 ^m	190 ^l		

a : present work b : [62] c : [63] d : [14], e: [64], f: [65], g: [12], h= [66], i: [67], j= [68], k: [69], l: [70], m: [71].

From table 4.2.5 we observe that our calculation is very close to experimental results and better than almost all other theoretical calculations.

4.2.2.2: x=0.25, 0.5, 0.75

The number of K-points for $\text{Ga}_{1-x}\text{Fe}_x\text{N}$ where $x=0.25, 0.5, 0.75$ is 216 with reduced $K_{\text{irred}}= 20, 36, 20$ respectively and matrix of $6 \times 6 \times 6$ using LSDA method, while using GGA method, the number of K-points is 512 with $K_{\text{irred}}= 40$ and matrix of $8 \times 8 \times 8$ for $x=0.25$, 216 K-points with $K_{\text{irred}}= 36$ and matrix of $6 \times 6 \times 6$ for $x=0.5$, and 343 K-points with $K_{\text{irred}}= 30$ and matrix $7 \times 7 \times 7$ for $x=0.75$.

The coordinates of the atoms for $x=0.25$ are set as follows. Fe atom set at (0, 0, 0), and 3 Ga atoms set at (0.5, 0.5, 0), (0.5, 0, 0.5), and (0, 0.5, 0.5), while N atoms set at (0.25, 0.25, 0.25), (0.25, 0.75, 0.75), (0.75, 0.25, 0.75), (0.75, 0.75, 0.25) positions.

For $x=0.75$ Ga atoms are replaced with Fe atoms and vice versa using the same space group (215) P43m, while for $x=0.5$ the space group is (111-P42m) with coordinates Ga1 atom at (0, 0, 0), Ga2 atom (0.5, 0, 0.5), Fe atoms at (0.5, 0.5, 0) and (0, 0.5, 0.5), while N atoms set at (0.25, 0.25, 0.25), (0.25, 0.75, 0.75), (0.75, 0.25, 0.75), (0.75, 0.75, 0.25) positions, for $x= 0.25, 0.5, 0.75$ for both LSDA, and GGA, $R_{\text{MT}}K_{\text{max}}=7.5, 8, 8$, respectively and $G=14$.

The volume of the unit cell for Zinc-Blende (FCC) is $V = a^3$

So,

$$a = (V)^{1/3} \dots\dots\dots(2)$$

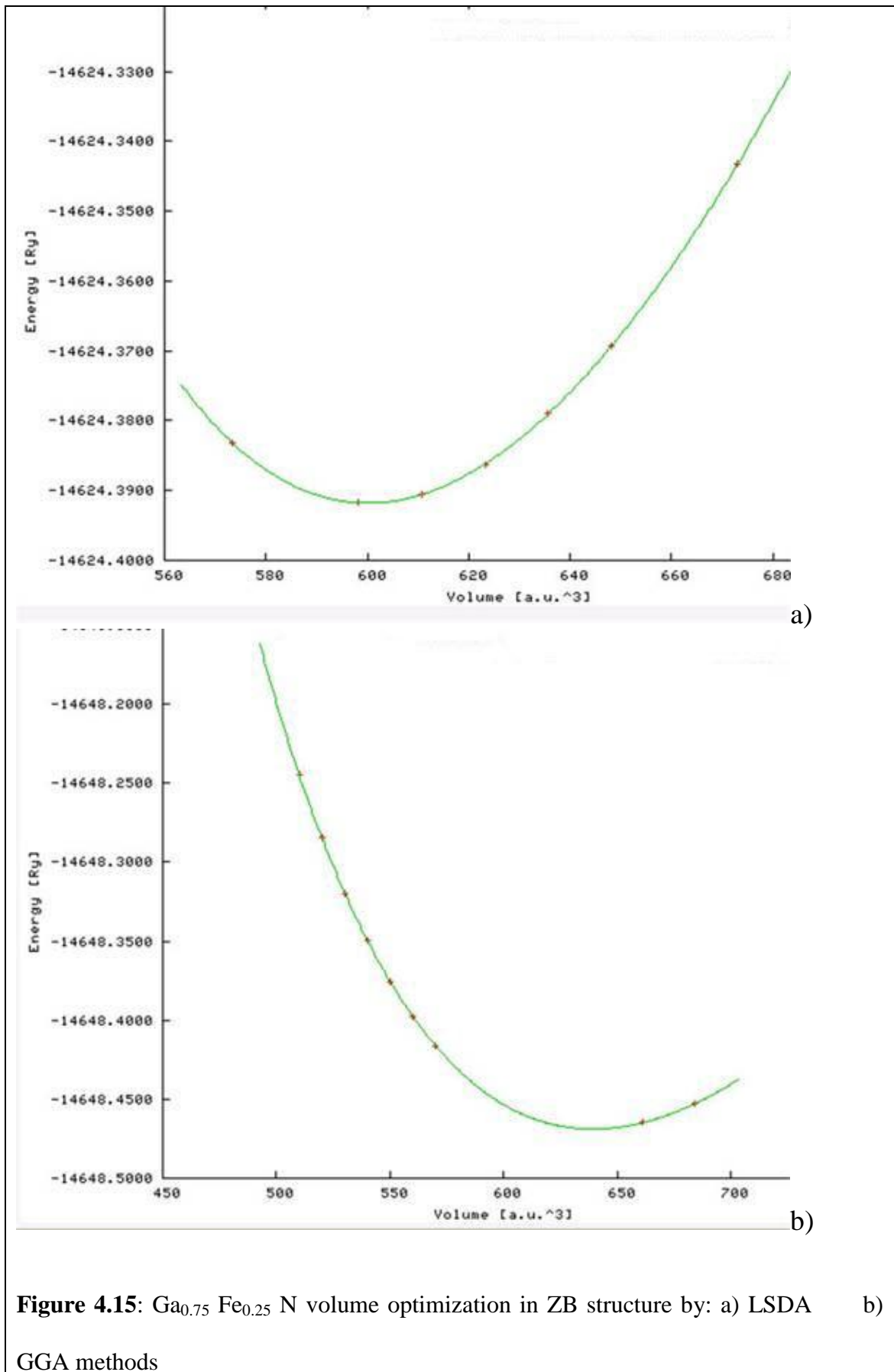


Figure 4.15: $\text{Ga}_{0.75}\text{Fe}_{0.25}\text{N}$ volume optimization in ZB structure by: a) LSDA b) GGA methods

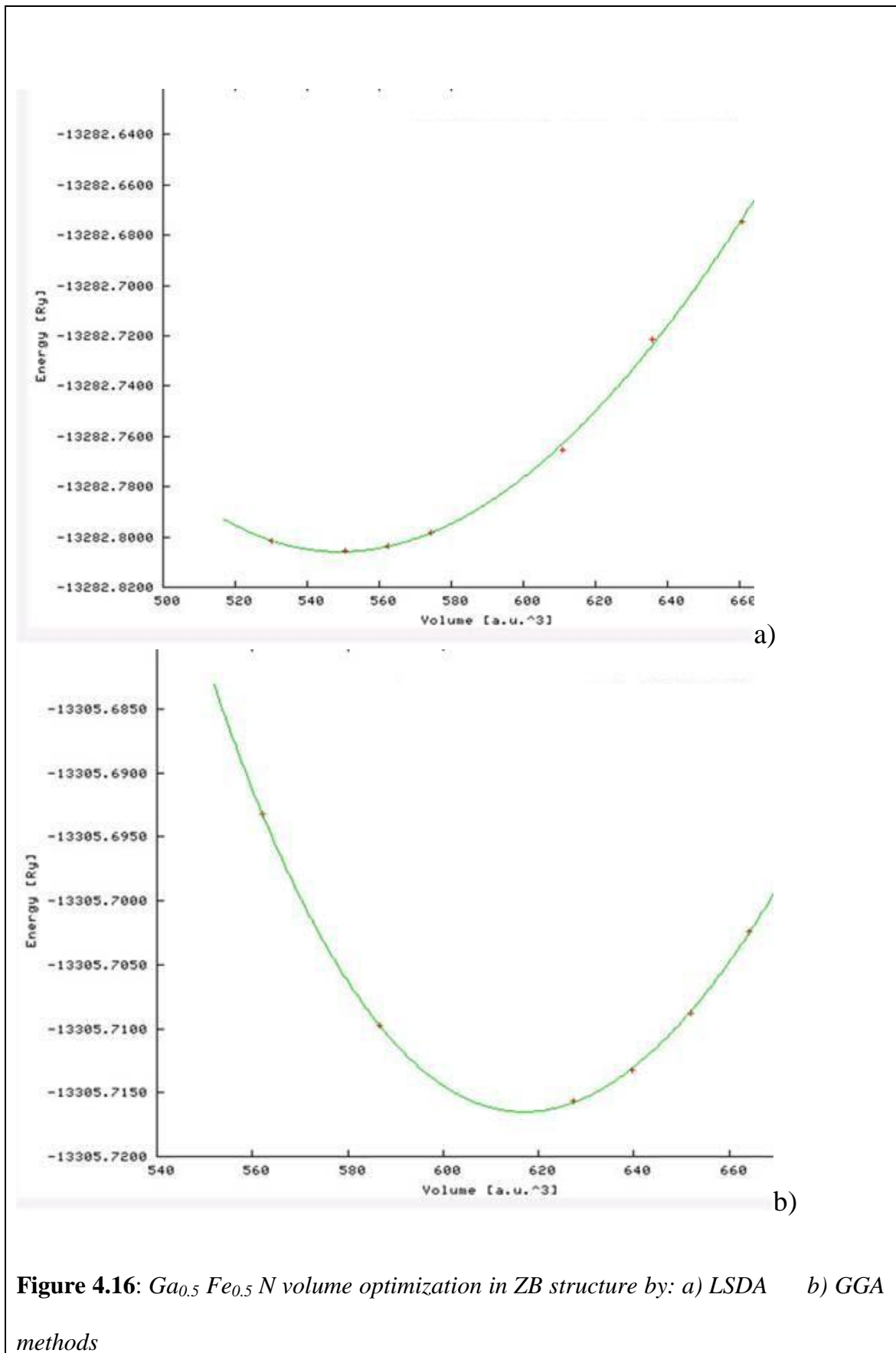


Figure 4.16: $Ga_{0.5}Fe_{0.5}N$ volume optimization in ZB structure by: a) LSDA b) GGA methods

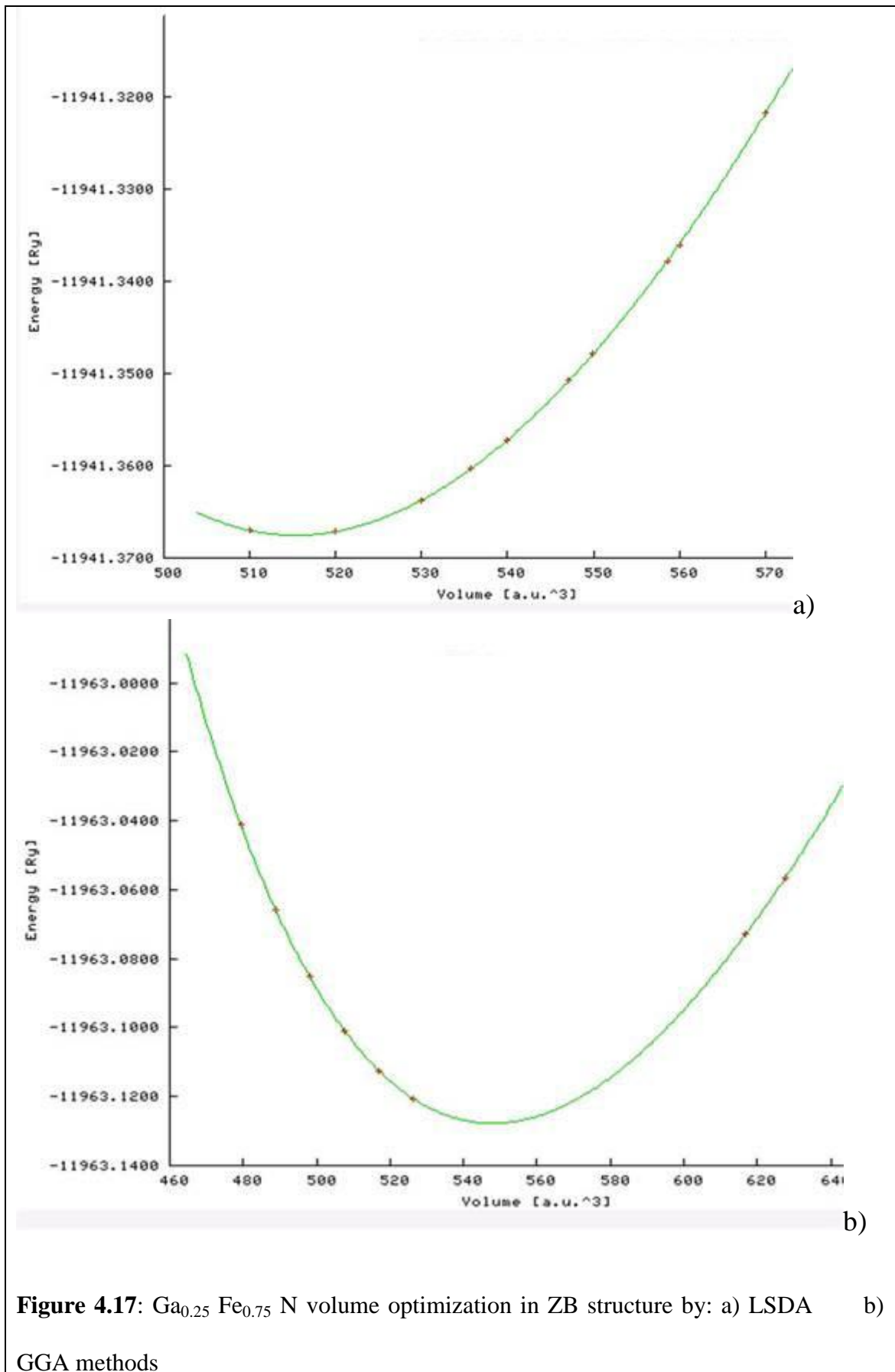


Figure 4.17: Ga_{0.25}Fe_{0.75}N volume optimization in ZB structure by: a) LSDA b) GGA methods

Using equation (2) and substitute V from the graphs in Figures 4.15-4.17, we get :

For $x = 0.25$

$$V = 600.078 \text{ (a. u.)}^3, a = 4.46 \text{ \AA}, \text{ using LSDA method.}$$

$$V = 639.198 \text{ (a. u.)}^3, a = 4.55 \text{ \AA}, \text{ using GGA method.}$$

For $x = 0.5$

$$V = 549.048 \text{ (a. u.)}^3, a = 4.33 \text{ \AA}, \text{ using LSDA method.}$$

$$V = 616.981 \text{ (a. u.)}^3, a = 4.50 \text{ \AA}, \text{ using GGA method.}$$

For $x = 0.75$

$$V = 515.275 \text{ (a. u.)}^3, a = 4.24 \text{ \AA}, \text{ using LSDA method.}$$

$$V = 547.869 \text{ (a. u.)}^3, a = 4.33 \text{ \AA}, \text{ using GGA method.}$$

Table 4.2.6: Lattice parameters, Bulk modulus, and pressure first derivative of $\text{Ga}_{1-x}\text{Fe}_x\text{N}$ in ZB structure using LSDA and GGA methods:

Alloy	Method	a(A°)	B(GPa)	B'
$\text{Ga}_{0.75}\text{Fe}_{0.25}\text{N}$	LSDA	4.46	196.81	4.348
	GGA	4.55	169.45	4.077
$\text{Ga}_{0.5}\text{Fe}_{0.5}\text{N}$	LSDA	4.33	200.877	4.534
	GGA	4.50	154.962	4.4666
$\text{Ga}_{0.25}\text{Fe}_{0.75}\text{N}$	LSDA	4.24	219.618	4.8597
	GGA	4.33	230.59	4.51

We observe here that the lattice constant (a) decreases as iron concentration(x) increase, because iron atoms are smaller than gallium atoms, while the bulk modulus increases which means that the hardness of the alloy increases with iron concentration, this increase caused due to decrease in volume of the cell.

The lattice constant obtained using GGA is larger than that obtained using LSDA, while the bulk modulus and its derivative obtained using GGA method is smaller than those obtained using LSDA.

4.2.2.3 $x=1$ (FeN Compound)

In (ZB) structure the same way is used to find the lattice constant, the number of K-points for $\text{Ga}_{1-x}\text{Fe}_x\text{N}$ where $x=1$ is 216 with reduced $K_{\text{irred}}= 22$ with matrix of $6 \times 6 \times 6$ for LSDA and 729 K-points with $K_{\text{irred}}= 55$ for GGA and matrix of $9 \times 9 \times 9$. In this structure, the Fe atom sets at (0,0,0), while N atom sets at (0.25, 0.25, 0.25) positions. For both, LSDA and GGA $R_{\text{MT}}K_{\text{max}}$ and G are 8 and 14, respectively.

The volume of the unit cell for Zinc-Blende (FCC) is $V = \frac{a^3}{4}$

So,

$$a = (4 * V)^{1/3} \dots\dots\dots (3)$$

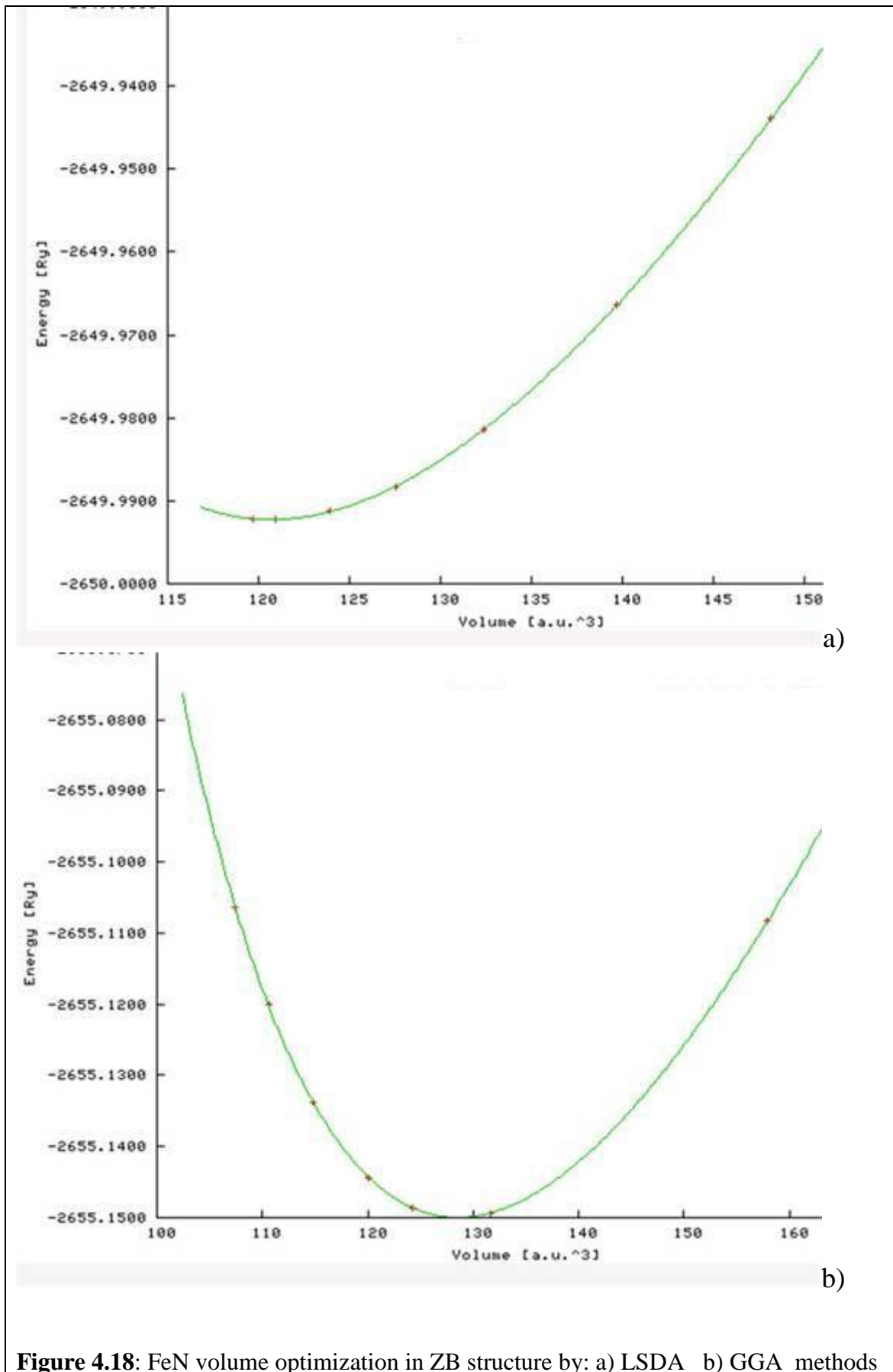


Figure 4.18: FeN volume optimization in ZB structure by: a) LSDA b) GGA methods

From eqn. (3) and graphs in Fig 4.18 we find that:

$V = 120.6636 \text{ (a. u.)}^3$, $a = 4.151 \text{ \AA}$, using LSDA method.

$V = 128.5484 \text{ (a. u.)}^3$, $a = 4.239 \text{ \AA}$, using GGA method.

Table 4.2.7: Lattice parameters, Bulk modulus, and pressure first derivative of FeN in ZB structure using LSDA and GGA methods:

Work	Method	a(A°)	B(GPa)	B'
Present	LSDA	4.151	338.415	5.1645
	GGA	4.239	262.3744	4.4856
Other calculations	ASW	4.35 ^a	-	-
	ASA LDA	4.169 ^c	332 ^c	4.2 ^c
	FP LDA	4.215 ^c	324 ^c	4.6 ^c
	ASA GGA	4.195 ^c	308 ^c	4.3 ^c
Exp.		4.307 ^b		

a: [20], b: [23], c: [66]

Our calculations, show that the GGA lattice constant is smaller than the experimental value by (0.068) A°, while LSDA lattice constant is smaller than the experimental value by (0.156) A°

So, lattice constant using LSDA is smaller than lattice constant using GGA, while bulk modulus using LSDA is greater than GGA bulk modulus.

Usually, in treating alloys, it is assumed that the atoms are located at the ideal sites of the lattice so the lattice constant vary linearly with the concentration (x) according to the so-called Vegard's law [69].

$$a(A_xB_{1-x}C) = x a_{AC} + (1-x) a_{BC}$$

where a_{AC} and a_{BC} are the equilibrium lattice constants of the binary compounds AC and BC respectively, and $a_{(A_xB_{1-x}C)}$ is the alloy lattice constant. However, violation of Vegard's law has been observed in semiconductor alloys theoretically and experimentally, then the lattice constant can be written as:

$$a_{(A_xB_{1-x}C)} = x a_{AC} + (1-x) a_{BC} - x(1-x)b$$

where b is the bowing parameter.

Figure 4.19 (a – d) shows the variation of the lattice constant and the bulk modulus calculated at equilibrium against the concentration x for $Ga_{1-x}Fe_xN$ alloys using LSDA and GGA methods, respectively. It is clear that the values show an increase in the bulk modulus with an increase in the concentration x , this gives an agreement with Veire suggestion [72], which means that adding iron to GaN improves their hardness. A deviation from Vegard's law is clearly seen, with upward bowing parameter for the lattice constant, and downward bowing parameter for the bulk modulus.

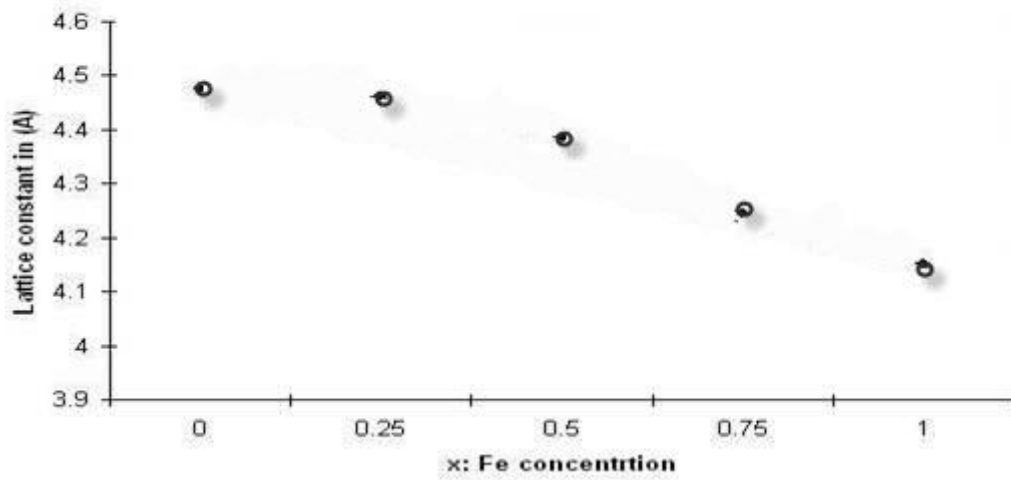
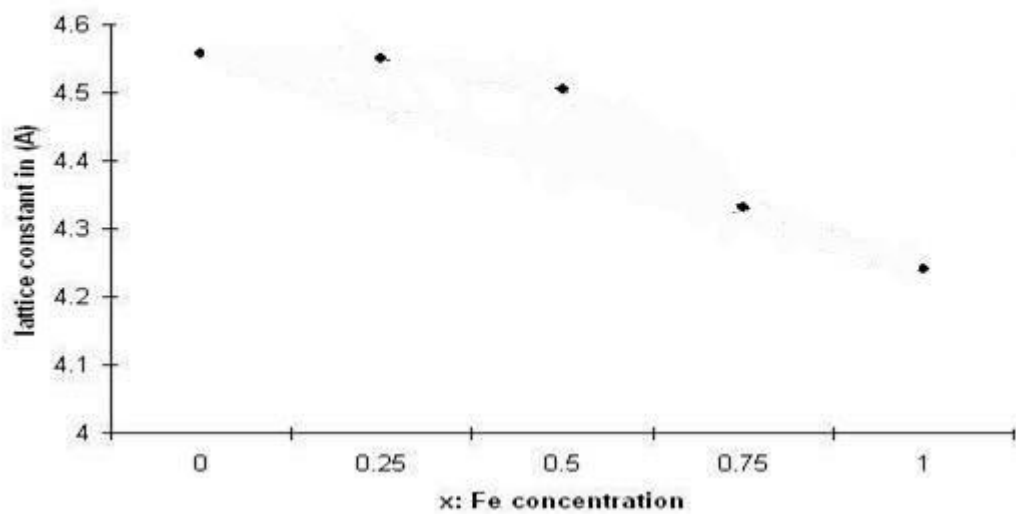
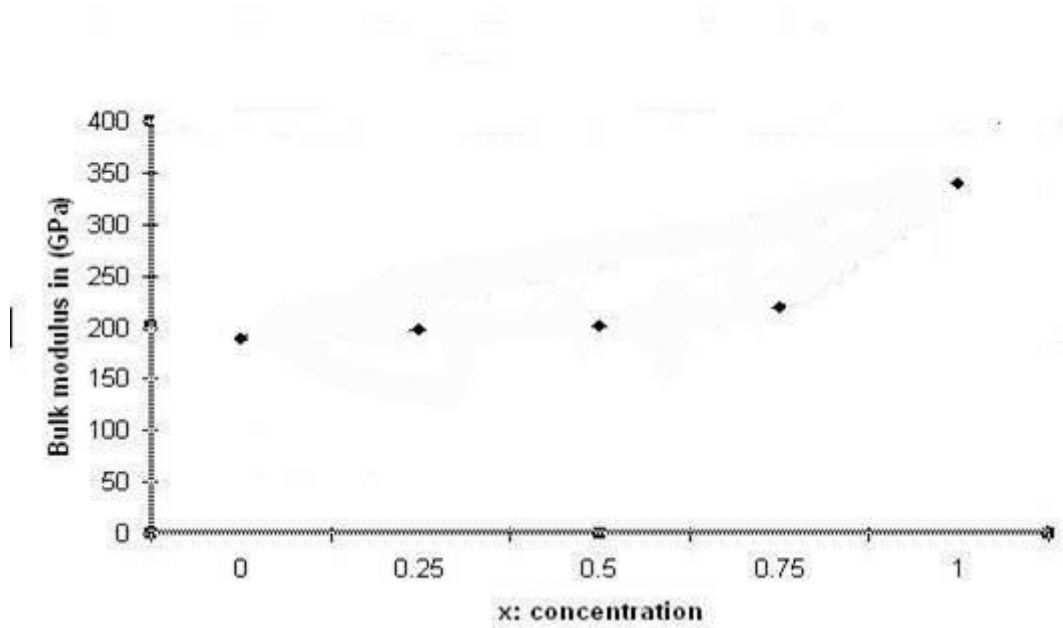


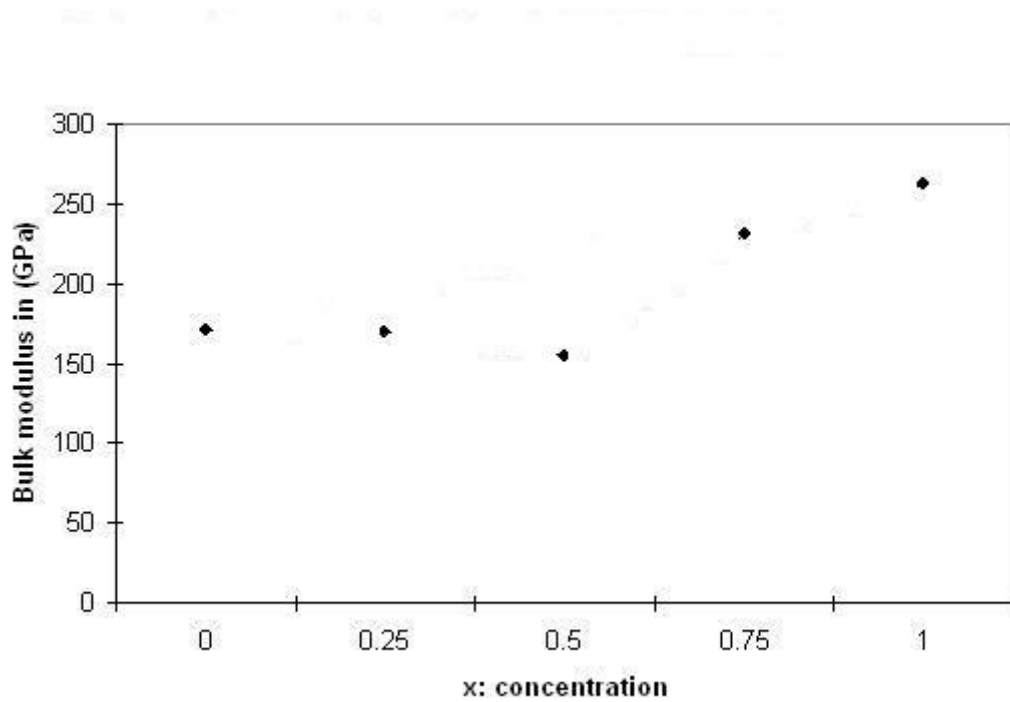
Fig 4.19: (a) lattice constant variation with Fe concentration for Ga_{1-x}Fe_xN using LSDA method.



(b) Lattice constant variation with Fe concentration for Ga_{1-x}Fe_xN using GGA method.



(c) Bulk modulus variation with concentration for Ga_{1-x}Fe_xN using LSDA method.



(d) Bulk modulus variation with concentration for Ga_{1-x}Fe_xN using GGA method.

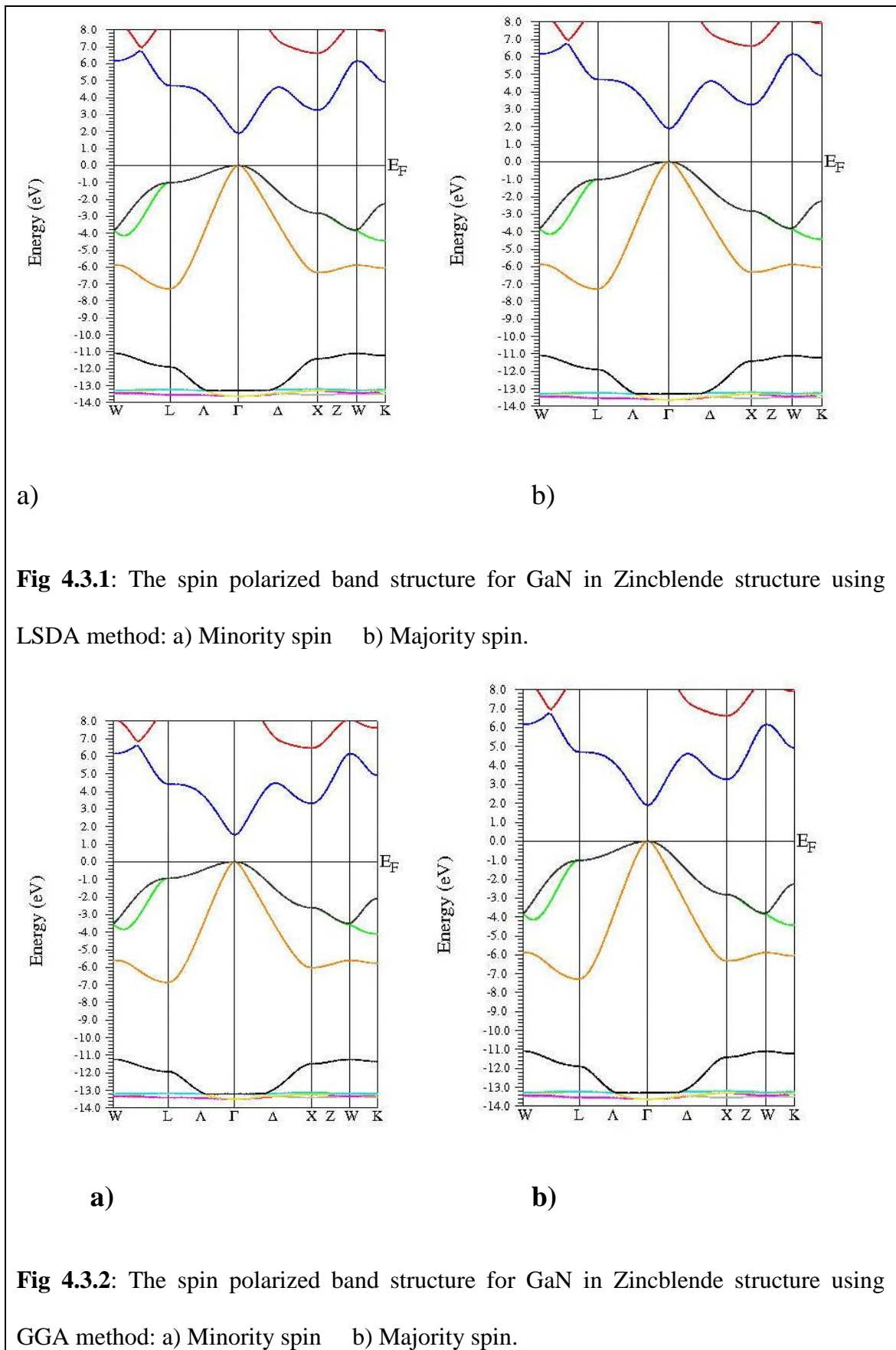
4.3 Electronic Properties of $\text{Ga}_{1-x}\text{Fe}_x\text{N}$

WIEN2K code is used to study the band structure and to calculate the energy band gap for each of $\text{Ga}_{1-x}\text{Fe}_x\text{N}$ alloys.

After finishing the optimization job, and calculating the structural parameters, we use the parameters of equilibrium structure to study the band structure, through generating structural file using the equilibrium values and initialize calculation, then we run SCF calculation. After that we choose band structure from WIEN2K task by editing the Fermi energy and running spaghetti lapw. Then we plot the band structure to get a graph showing the nature of that compound through the width of its band gap from graph.

4.3.1 band structure and band gap energy

Spin polarized calculations were performed using spin up and spin down electrons separately. Figures 4.3.1-4.3.10, show the spin polarized band structure of $\text{Ga}_{1-x}\text{Fe}_x\text{N}$ with $x= 0, 0.25, 0.5, 0.75, 1$ for both spin up and spin down (majority spin and minority spin) using both LSDA and GGA approximations.



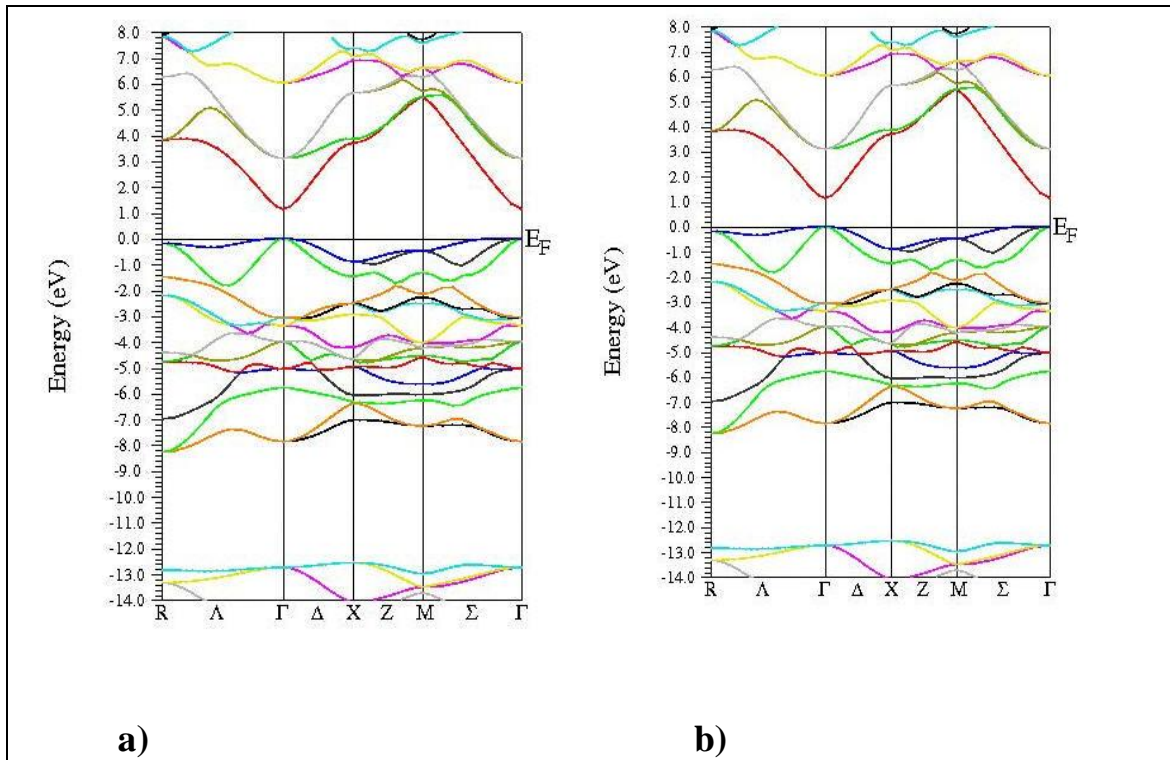


Fig 4.3.3: The spin polarized band structure for $\text{Ga}_{0.75}\text{Fe}_{0.25}\text{N}$ in Zincblende structure using LSDA method: a) Minority spin b) Majority spin

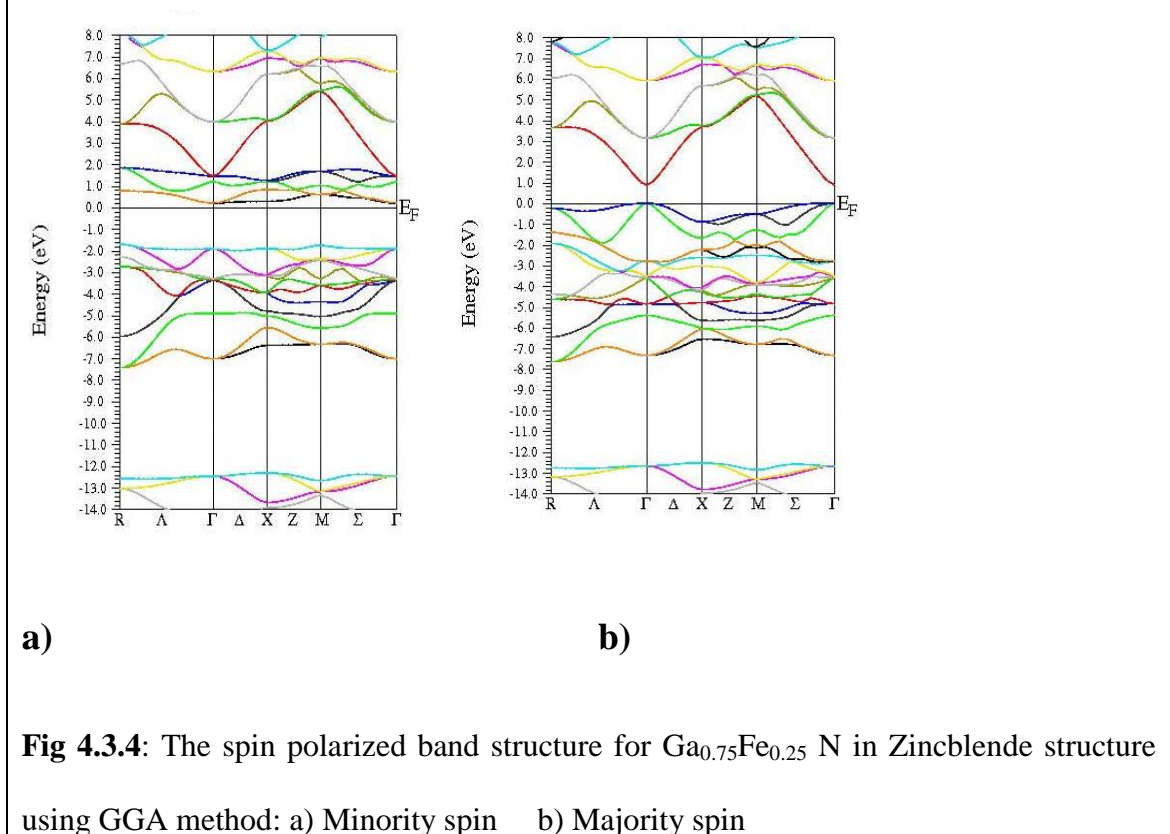


Fig 4.3.4: The spin polarized band structure for $\text{Ga}_{0.75}\text{Fe}_{0.25}\text{N}$ in Zincblende structure using GGA method: a) Minority spin b) Majority spin

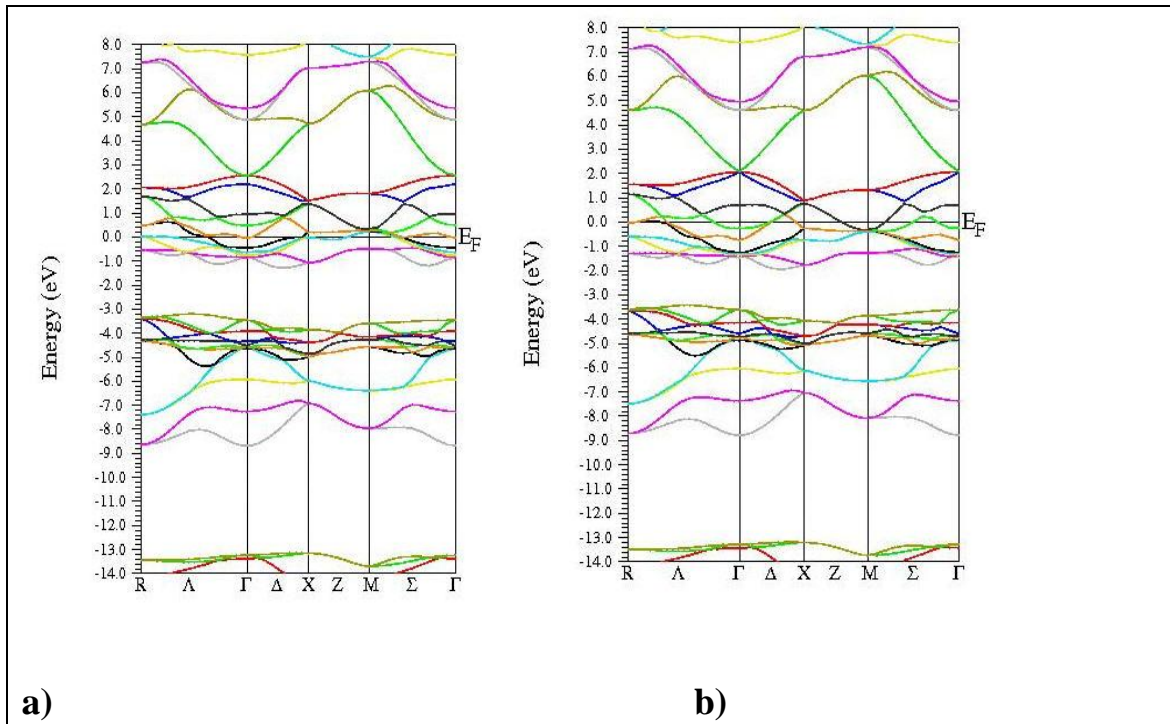


Fig 4.3.5: The spin polarized band structure for $\text{Ga}_{0.5}\text{Fe}_{0.5}\text{N}$ in Zincblende structure using LSDA method: a) Minority spin b) Majority spin

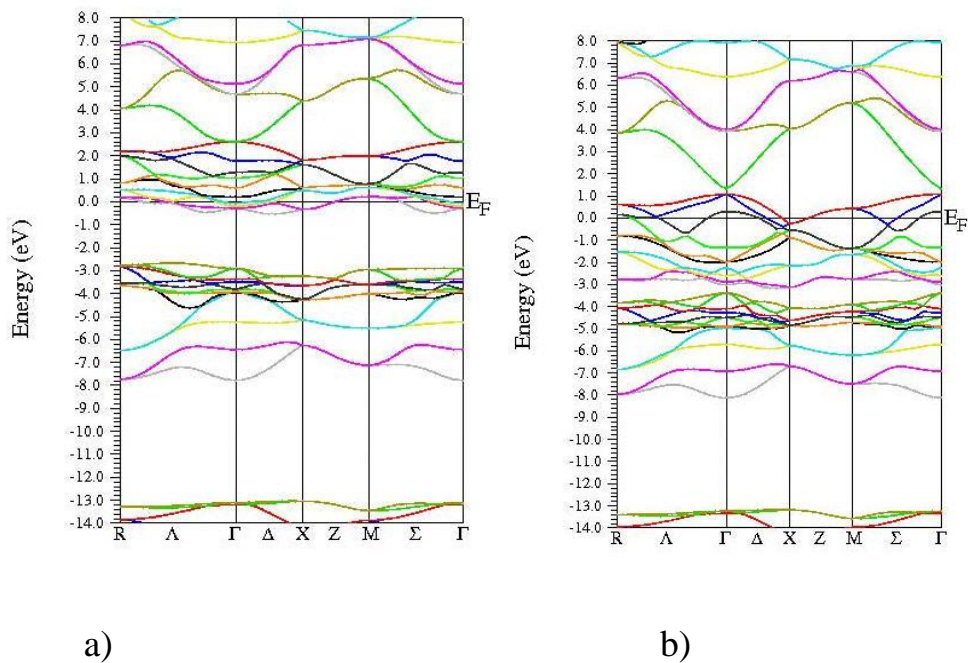


Fig 4.3.6: The spin polarized band structure for $\text{Ga}_{0.5}\text{Fe}_{0.5}\text{N}$ in Zincblende structure using GGA method: a) Minority spin b) Majority spin

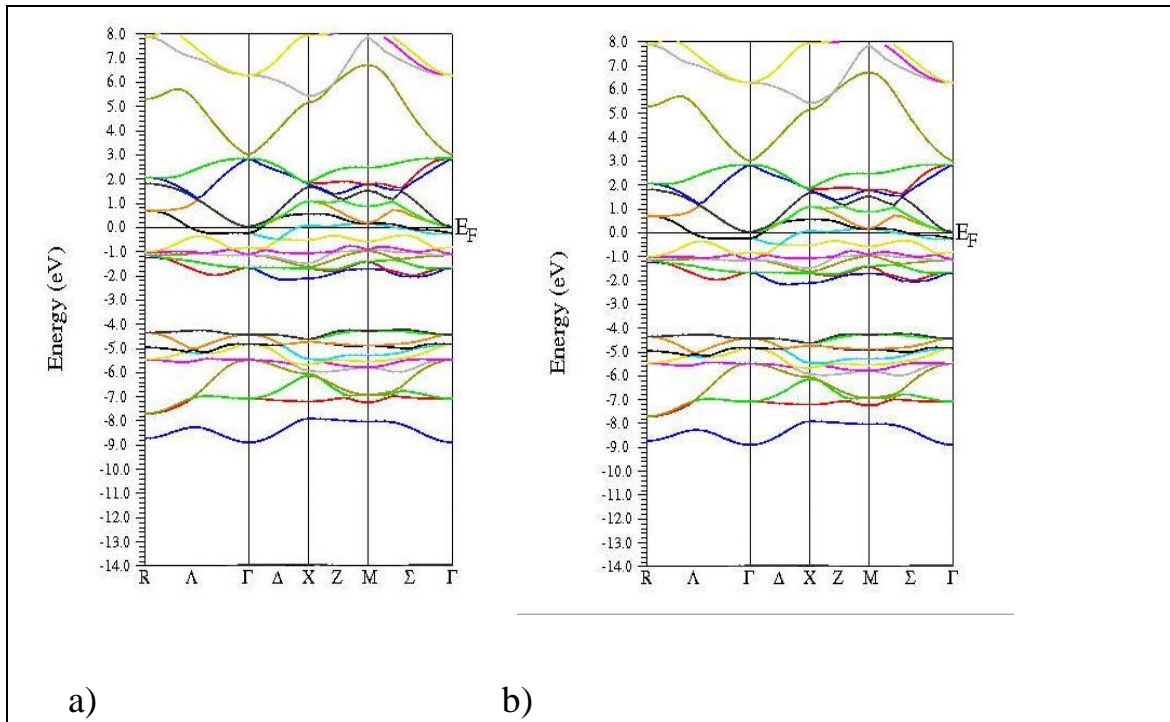


Fig 4.3.7: The spin polarized band structure for $\text{Ga}_{0.25}\text{Fe}_{0.75}\text{N}$ in Zincblende structure using LSDA method: a) Minority spin b) Majority spin

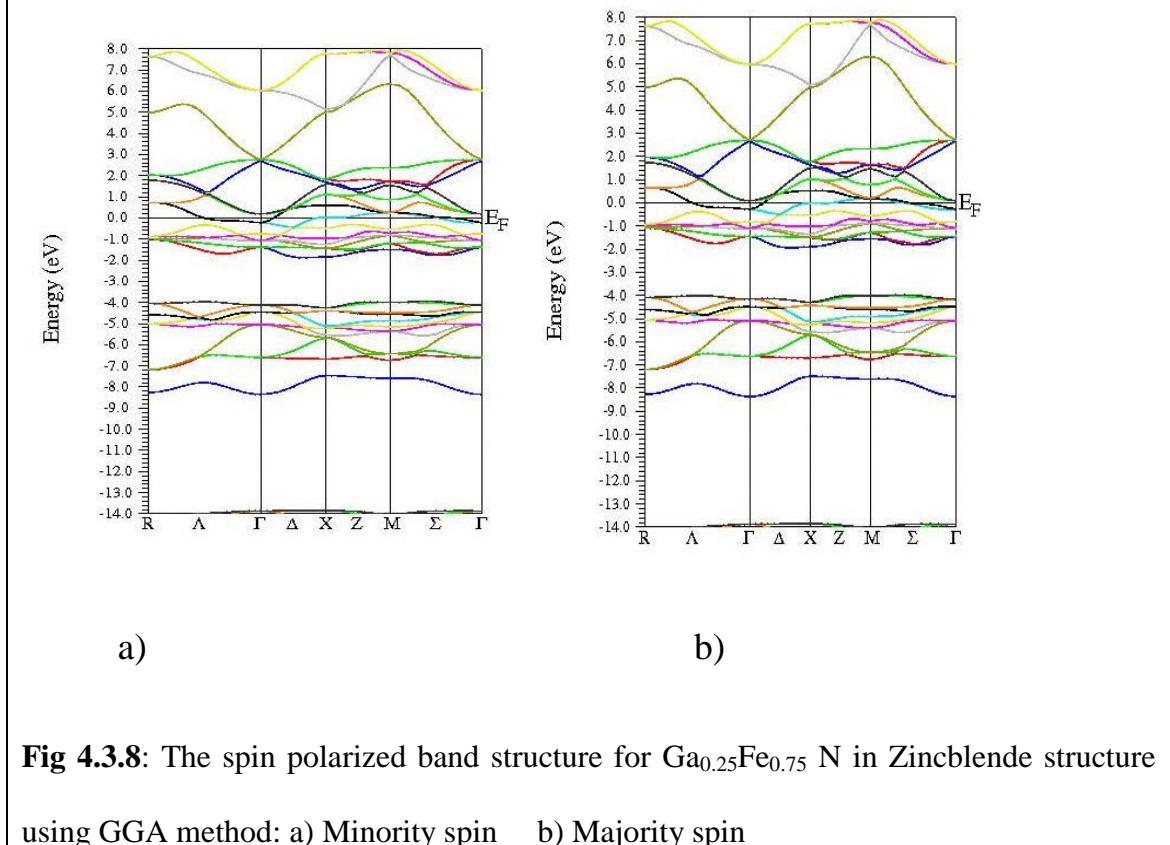


Fig 4.3.8: The spin polarized band structure for $\text{Ga}_{0.25}\text{Fe}_{0.75}\text{N}$ in Zincblende structure using GGA method: a) Minority spin b) Majority spin

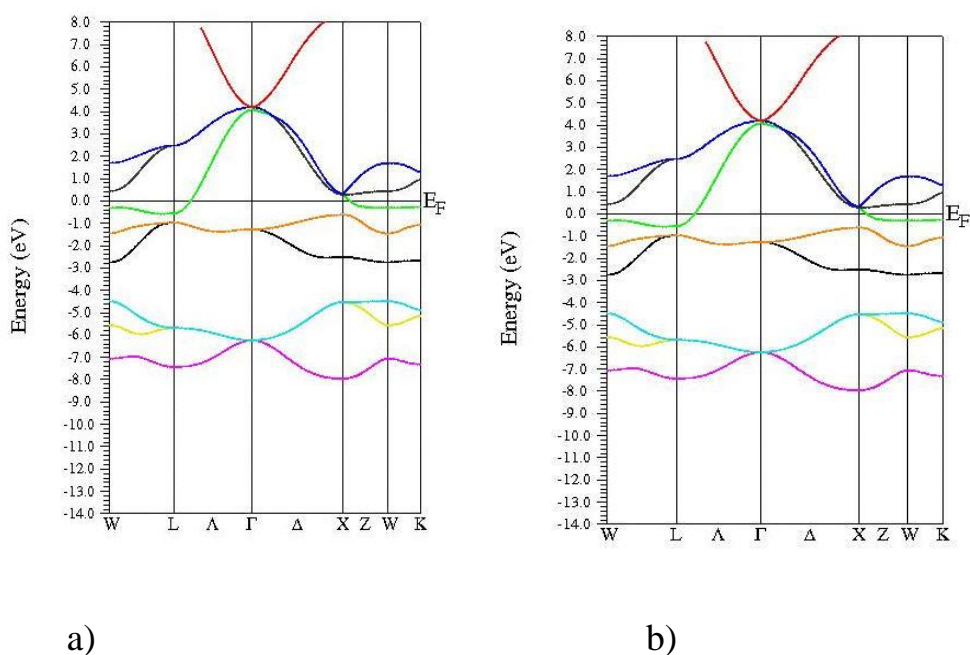


Fig 4.3.9: The spin polarized band structure for FeN in Zincblende structure using LSDA method: a) Minority spin b) Majority spin

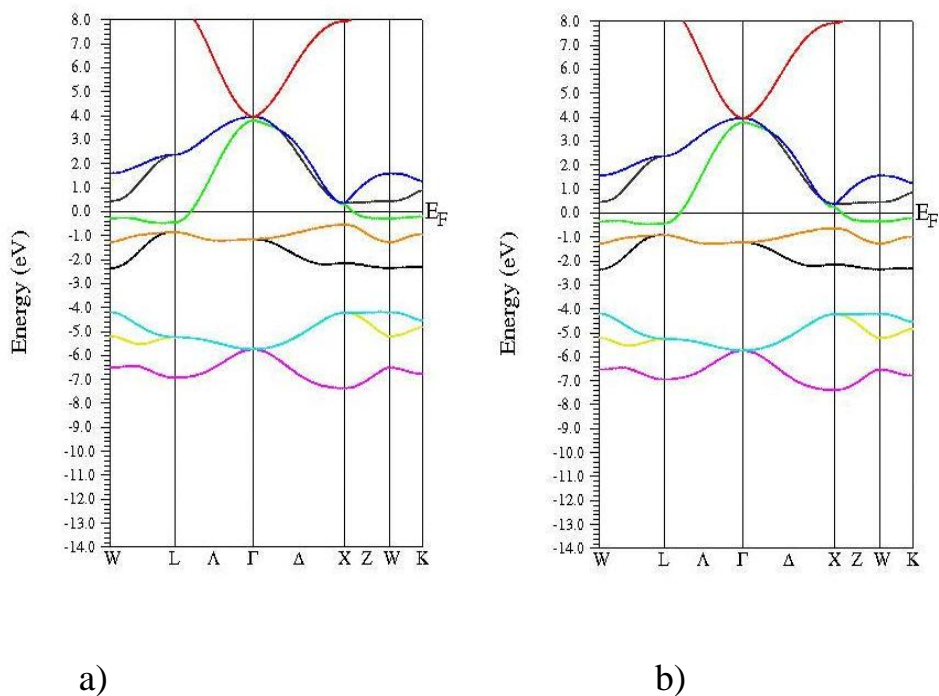


Fig 4.3.10: The spin polarized band structure for FeN in Zincblende structure using GGA method: a) Minority spin b) Majority spin

The valence band maximum and the conduction band minimum occurs both at the Γ point. The main band gaps direct (Γ - Γ) and indirect (Γ -X) band gaps are given in table 4.3.1 as well as the theoretical and experimental available values. Figures (4.3.11-4.3.14) show the relation of direct and indirect band gap energy variation with concentration of Fe in $\text{Ga}_{1-x}\text{Fe}_x\text{N}$ alloys using both LSDA and GGA methods.

The variation of the direct $E_{\Gamma-\Gamma}$ and indirect $E_{\Gamma-X}$ band gaps versus alloy composition is given in fig 4.3.11 (a-d) using LSDA and GGA methods respectively. Through fig. 4.3.11 we observe that the direct gap decreases when the concentration of iron increases with a linear decrease between 0 and 0.5 concentration having an average slope of 3.7486 eV and 2.5324 eV using LSDA and GGA methods, respectively. From fig. 4.3.11 we observe a down bowing parameter for direct band gap curve and a bowing up parameter for indirect band gap in both LSDA and GGA methods. This implies that the alloy is changed from semiconductor to metal with the increase of the iron concentration.

From figures (4.3.3 – 4.3.8), as the concentration of iron increases we notice that some bands are slightly crossing the Fermi level, so the maximum of the valance band becomes higher and the band gap energy becomes narrower.

Table (4.3.1): Direct and indirect band gap energy of $\text{Ga}_{1-x}\text{Fe}_x\text{N}$ alloy for different concentrations at equilibrium volume.

Concentration	Direct band gap (Γ - Γ) LSDA	Indirect band gap (Γ -X) LSDA	Direct band gap (Γ - Γ) GGA	Indirect band gap (Γ -X) GGA
0	1.902 ^a , 1.922 ^b 1.8 ^c 2.20 ^d 1.97 ^d	3.9658 ^a	1.5238 ^a 1.517 ^b	3.921 ^a
0.25	1.1326 ^a	3.6937 ^a	0.887 ^a	3.6726 ^a
0.50	0.0277 ^a	2.534 ^a	0.2576 ^a	2.9529 ^a
0.75	0.1462 ^a	2.321 ^a	0.02595 ^a	2.2856 ^a
1.0	0 ^a	-3.857 ^a	0 ^a	-3.58 ^a

a: present work, b: [10], c: [14] d: [73]

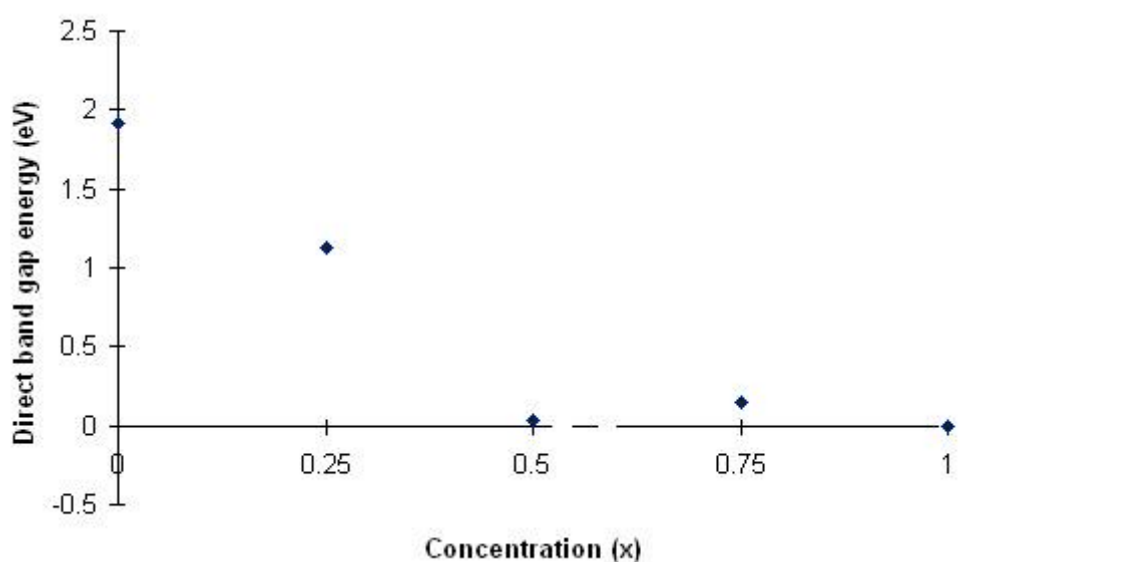
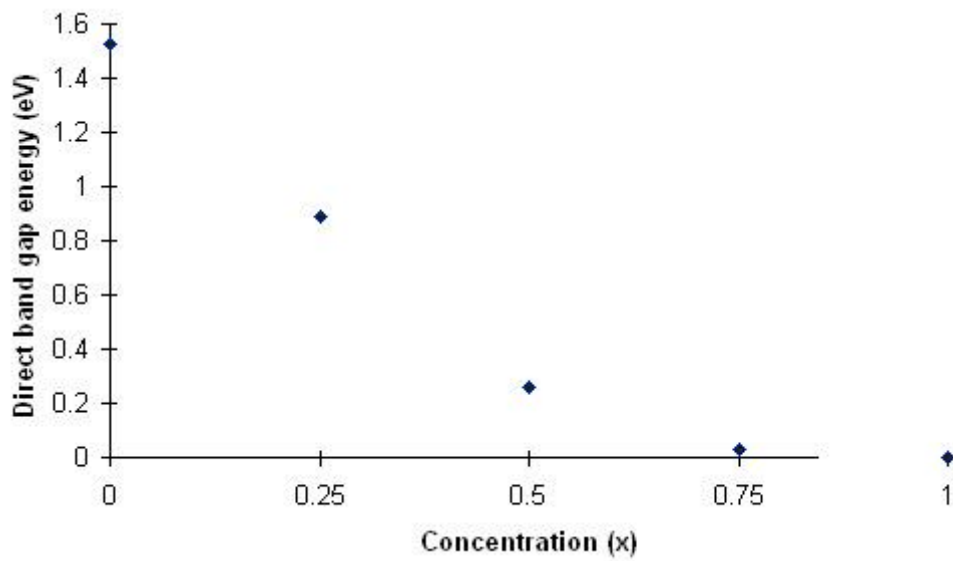
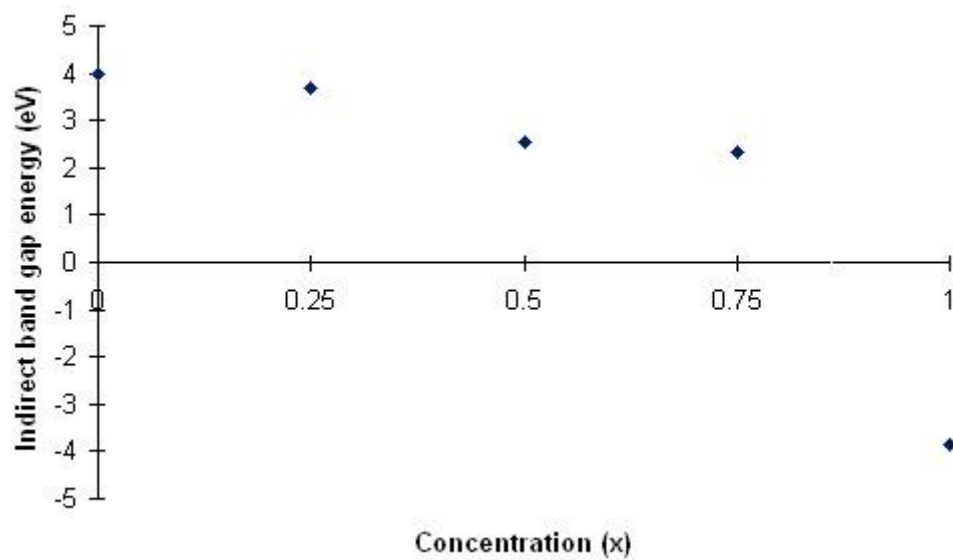


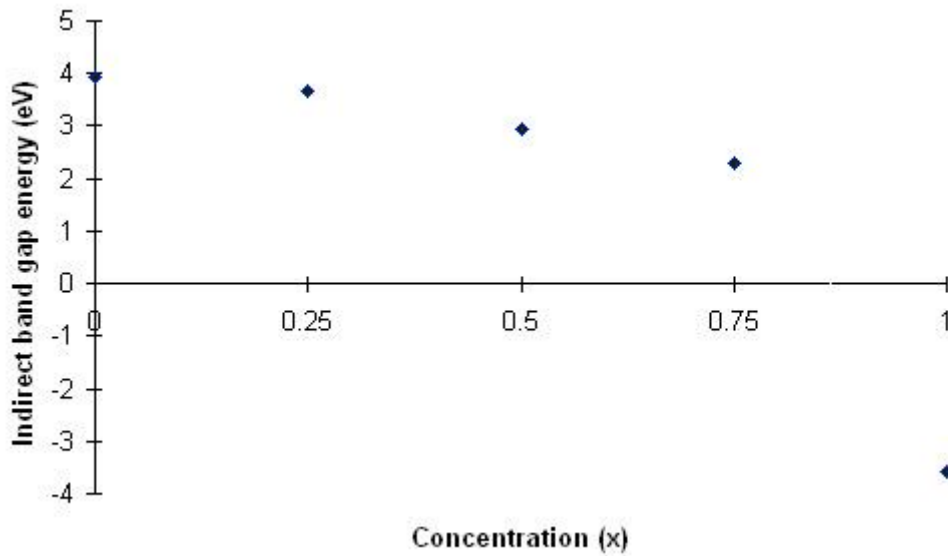
Fig (4.3.11) (a): direct band gap energy versus concentration of $\text{Ga}_{1-x}\text{Fe}_x\text{N}$ alloy using LSDA method.



(b) Direct band gap energy versus concentration of Fe in $\text{Ga}_{1-x}\text{Fe}_x\text{N}$ alloy using GGA method



(c) Indirect band gap energy versus concentration of Fe in $\text{Ga}_{1-x}\text{Fe}_x\text{N}$ using LSDA method.



(d) Indirect band gap energy versus concentration of Fe in $\text{Ga}_{1-x}\text{Fe}_x\text{N}$ using GGA method

4.4 Magnetic Properties of $\text{Ga}_{1-x}\text{Fe}_x\text{N}$ alloys

The total magnetic moment (MMTOT) per unit cell of

$\text{Ga}_{1-x}\text{Fe}_x\text{N}$ at $x = 0.25$ is $5 \mu_B$ using both LSDA and GGA approaches. The main value of the MMTOT is strongly localized on the Fe site $\sim 3.1 \mu_B$, the remaining value comes from the Ga and N atoms, table (4.4.1).

The MMTOT for $x = 0.5$ is about $5.8 \mu_B$ at the equilibrium lattice constant ($a_0^{\text{LSDA}} = 4.46 \text{ \AA}$) using LSDA approach, and it is about $6.6 \mu_B$ at ($a_0^{\text{GGA}} = 4.55 \text{ \AA}$) using GGA approach. Because of the lattice constant difference (0.09 \AA) between LSDA and GGA the MMTOT differ by $0.8 \mu_B$; while for $x = 0.75$ a difference of about $0.25 \mu_B$ is observed due to the difference in the lattice constant at equilibrium of about 0.057 \AA . Table 4.4.1 shows that the main value of the total magnetic moment is strongly localized on the Fe

site, the remaining values come from the N and Ga atoms, so the most important role in this system is due to the contribution of the Fe atoms, and the related Fe-Fe spin interaction.

Table 4.4.1: Total and local Magnetic Moment in $\text{Ga}_{1-x}\text{Fe}_x\text{N}$ system in ZB structure using LSDA and GGA approximations.

Concentration x		Magnetic moment of each atom (LSDA)	Magnetic moment of each atom (GGA)
0.25	Interstitial μ_B	1.16546	1.17193
	Ga μ_B/atom	0.02933	0.02400
	Fe μ_B/atom	3.03482	3.10178
	N μ_B/atom	0.17590	0.16424
	MMTOT ($\mu_B/\text{unit cell}$)	4.99186	5.00269
0.50	Interstitial μ_B	1.37012	1.46328
	Ga μ_B/atom	0.03516	0.03567
	Fe μ_B/atom	2.03321	2.34936
	N μ_B/atom	0.93170	0.09399
	MMTOT ($\mu_B/\text{unit cell}$)	5.81311	6.59929
0.75	Interstitial μ_B	0.01514	0.09259
	Ga μ_B/atom	0.00071	0.00271
	Fe μ_B/atom	0.01454	0.06343
	N μ_B/atom	0.00382	0.00875
	MMTOT ($\mu_B/\text{unit cell}$)	0.07134	0.32059
1.0	Interstitial μ_B	0.00000	0.00791
	Fe μ_B/atom	0.00000	0.00383
	N μ_B/atom	-0.00002	0.00440
	MMTOT ($\mu_B/\text{unit cell}$)	-0.00001	0.01613
Other calculations FeN (x=1)		0 ^a 0 ^b	

a: [21], b: [39]

Fig 4.4.1 (a, b) show the calculated total magnetic moment of $\text{Ga}_{1-x}\text{Fe}_x\text{N}$ alloys versus the concentration of the iron using FP-LAPW method within LSDA and GGA approximations. These alloys change from paramagnetic ($x=0$) to ferromagnetic ($x = 0.25, 0.5, 0.75$) to nonmagnetic ($x=1$). The result for FeN ($x=1$) agrees with other theoretical results [21].

The Fe atom has 5 extra electrons, thus there is an addition of five extra spin-up states, but no addition spin-down state in valance band, so all spin up states are occupied, but spin down states are empty. Thus in this case the spin-up state in N ions become more occupied than the spin-down state and consequently induced magnetic moments in N ions are parallel to that of Fe ions. The Ga cations interact with N ions in the same way as Fe ion for energy gain and consequently the magnetic coupling between Ga and N is ferromagnetic due to Fe ions. As Fe impurity is increased the spin polarization between spin-up and spin-down e_g bands decreases which results in decrease in the magnetic moment.

From table 4.4.1 we observe that, when Fe substitute Ga site it gives a magnetic moment = $5 \mu_B$, the Fe d-state dominate the total magnetic moment by amount of $3.03482 \mu_B$ using LDA, and $3.10178 \mu_B$ using GGA; which is about 61% for LDA method and 62% for GGA method of the total magnetic moment at iron concentration $x=0.25$. Fe magnetic moment is very much localized inside the first coordinational sphere of the impurity; magnetic moments induced at the nearest N atom are $0.16-0.175\mu_B$ (the 2p contribution), while Ga contribution is very small ($0.024-$

0.029 μ_B). This is due to hybridization of spin-up p-like states of the N atoms with the spin-up of the Fe d-states which form the states at the top of the valance band. The spin-down p and d-states hybridized to form the lower portion of the valance band.

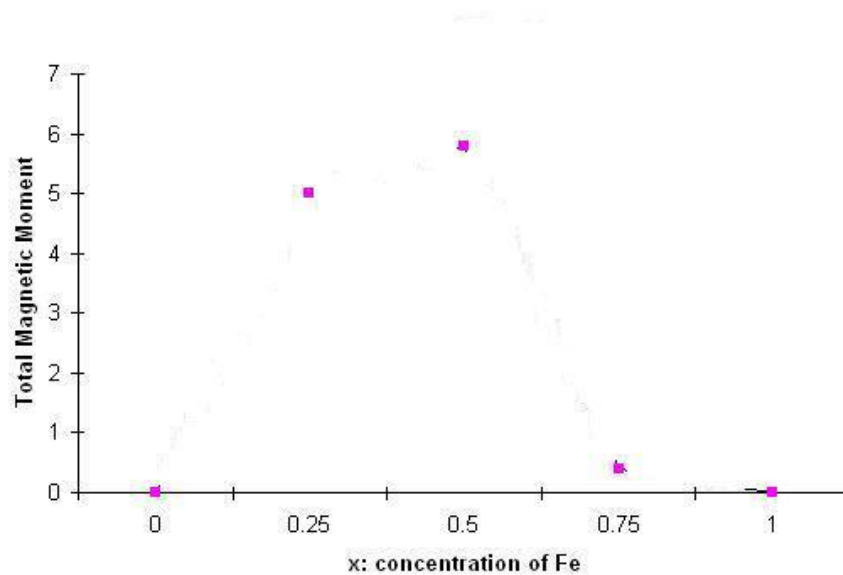
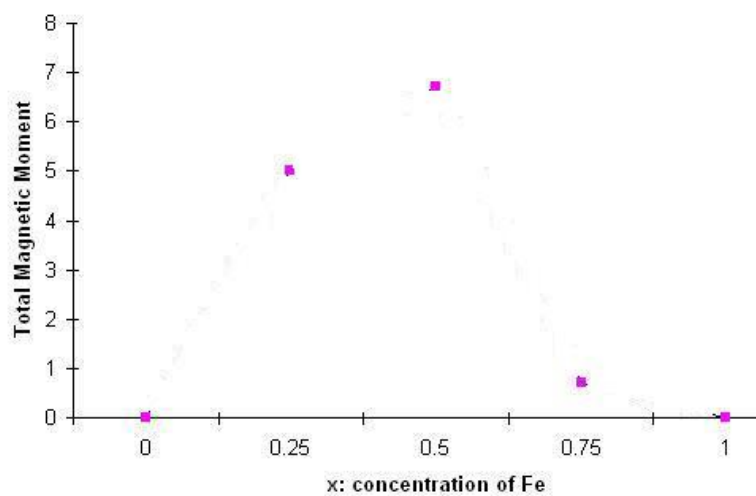


Fig (4.4.1): (a) MMTOT using LSDA method



(b) MMTOT using GGA method

Chapter V

Conclusions

The ternary alloys $\text{Ga}_{1-x}\text{Fe}_x\text{N}$ properties are calculated using the self consistent FP-LAPW method within the LSDA and GGA approximations. We have studied the equilibrium lattice parameters for different values of iron concentrations

($x= 0, 0.25, 0.5, 0.75, 1$).

Our results are in good agreement with the other calculations for $x= 0, 1$, but there is no other theoretical or experimental results in the literatures for ($x= 0.25, 0.5, 0.75$). We found that the lattice parameters of $\text{Ga}_{1-x}\text{Fe}_x\text{N}$ alloys depend on the Fe doped atoms concentration.

We found that Fe doped GaN converts it from semiconductor to metal.

The total magnetic moment depends strongly on iron concentration and reaches its maximum value ($5.81311 \mu_B/\text{unit cell}$ using LSDA and $6.59929 \mu_B/\text{unit cell}$ using GGA) at $x= 0.5$. The main value of the total magnetic moment is strongly localized on the Fe.

We found that FeN has a total magnetic moment equal to zero at the equilibrium lattice parameter using the LSDA and GGA methods, which is in a good agreement with other results (table 4.4.1).

The main results and conclusions of our work are summarized as follows:

1- The calculated structural parameters (a , B , and B') at $x=0, 1$ using FP-LAPW, are found to be in good agreement with the available theoretical and experimental results .

2- The equilibrium lattice parameters of $\text{Ga}_{1-x}\text{Fe}_x\text{N}$ alloys ($x=0, 0.25, 0.5, 0.75, 1$) using GGA approach are larger than those obtained using the LSDA approach, while the bulk modulus values obtained using GGA approach are smaller than those obtained using LSDA approach.

3- The lattice parameters of $\text{Ga}_{1-x}\text{Fe}_x\text{N}$ alloys depend strongly on the Fe concentration.

4- The energy at equilibrium lattice constant using GGA approach always larger than which obtained using LSDA approach.

5- Upon Fe doping GaN we found that the compound converted from semiconductor to a metal.

6- The total magnetic moment of $\text{Ga}_{1-x}\text{Fe}_x\text{N}$ alloys depends strongly on Fe concentration and reaches its maximum at $x=0.5$.

7- The calculated total magnetic moment of FeN are zero at equilibrium lattice parameters using both LSDA and GGA methods.

8- The calculated total magnetic moment for $\text{Ga}_{1-x}\text{Fe}_x\text{N}$ alloys at the equilibrium lattice constant using GGA are always greater than those obtained using LSDA approach.

References

- [1] H. Morko C. C, S. Strite, G.B. Gao, M.E. Lin, B. Sverdlov, and M. Burns, **J. Appl. Phys.** **76**, 1363 (1994)
- [2] S. N. Mohammed, A. Salvador, and H. Markoc, **Proc. IEEE** **83**, 1306 (1995)
- [3] F. Litimein, B. Bouhafs, G. Noure, and P. Ruterana, **Phys. Status Solidi b** **243**, 1577 (2006)
- [4] R. F. Davis, **Physica B** **185**, 1 (1993)
- [5] S. C. Jain, M. Willander, J. Narayam, R. Van Overstraeten, **J. Appl. Phys.** **87**, 965 (2000)
- [6] P. Carrier and S. H. Wie, **J. Appl. Phys.** **97**, 033707 (2005)
- [7] F. A. Ponce and D. P. Bour, **Nature** **386**, 351 (1997)
- [8] S. Nakamura, M. Seno and T. Mukai, **Appl. Phys. Lett.** **62**,2390 (1993)
- [9] G. Fasol, **science** **278**, **1902** (1997)
- [10] H. Y. Xiao, Fie Gao, X. T. Zu, and W. I. Weber, **Journal of Alloys and Compounds** **490**, 537-540 (2010)
- [11] Tan Li-Na, Hu Cui-E, Yu Bai-Ru, and Chen Xiang-Rong, **Chin. Phys. Soc. And IOP Publishing Ltd**, vol.16, No12 (2007)

- [12] B. Daoudi, M. Sehil, A. Boukraa, and H. Abid, **Int. J. Nanoelectronics and Materials** **1**, 65-79 (2008)
- [13] O. Arbouche, B. Belgoumene, B. Soudini, and M. Driz, **Computational Materials Science** **47**, 432-438 (2009)
- [14] S. Berrah, H. Abid, and A. Boukortt, **Semiconductor Physics, Quantum Electronics & Optoelectronics**, **9**, N2.P. 12-16,(2006).
- [15] S. Saib and N. Bouarissa, **Physica B** **387**, 377-382 (2007)
- [16] M. Abu-Jafar, A. I. Al-Sharif, and A. Qteish, **Solid State Communications** **116**, 389-393 (2000)
- [17] G. Y. Gao, K.L.Yao, Z. L. Liu, Y. L. Li, Y. C. Li, and Q. M. Liu, **Solid State Communications** **138** 494-497 (2006)
- [18] D. Li, J. W. Roh, K. J. Jeon, Y. S. Gu, and W. Lee, **Phys. Stat. Sol. (b)**, **No. 11**, 2581 – 2585 (2008)
- [19] X. Wang, W. T. Zheng, H. W. Tian, S. S. Tu, W. Xu, S. H. Meng, X. D. He, J. C. Han, C. Q. Sun, and B. K. Tay, **Applied Surface Science** **220**, 30- 39 (2003)
- [20] A. Houari, S. F. Matar, and M. A. Belkhir, **Journal of Magnetism and Magnetic Materials** **322**, 658-660 (2010)
- [21] A. Houari, S. F. Matar, M. A. Belkhir, and M. Nakhl, **Cond-Mat. Mtrl-Sci.** **1245**, v1 (2009)

- [22] B. Eck, R. Dronskowski, M. Takahashi, and S. Kikkawa, **J. Mater. Chem.** **9**, 1527-1537 (1999)
- [23] K. Suzuki, H. Morita, T. Kaneko, H. Yoshida, and H. Fujimori, **J. Alloys and Compounds** **201**, 11 (1993).
- [24] N. Heiman, N. S. Kazama, **J. Appl. Phys.** **52**, 3562-3564 (1981)
- [25] L. Wenzhi, J. Pak, D. C. Ingram, and A. R. Smith, *Journal of alloys and compounds*. vol. **463**, 257- 262 (2008)
- [26] T. Hinomura, S. Nasu, **Physica B** **237-238**, 557-558 (1997)
- [27] Y. Kong, **Cond-Mat. Mtrl-Sci** **4091**, v1 (2000)
- [28] B. Dieny, R.C. Sousa, J. Héroult, C. Papusoi, G. Prenat, U. Ebels, D. Houssameddine, B. Rodmacq, S. Auffret and L.D. Buda-Prejbeanu, **Int. J. Nanotechnol.**, **Vol. 7**, Nos. 4/5/6/7/8, (2010)
- [29] T. Jungwirth, J. Sinova, J. Masek, J. Kuzner, and A. H. MacDonald, **Rev. Mod. Phys.** **78**, 809 (2006)
- [30] G. M. Dalpian, J. L. F. Da Silva, and S. Wie, **Physical Review B** **79**, 241201 (2009)
- [31] H. Ohno, **Science** **281**, 951-956 (1998)
- [32] K. Sato, and H. Katayama-Yoshida, **Semicond. Sci. Technol.** **17**, 367-376 (2002)

- [33] H. Katayama-Yoshida, and K. Sato, **Physica B** **327**, 337- 337 (2003)
- [34] R. P. Vaudo, X. Xu, A. Salant, J. Malcarne, and G. R. Brandes, **Phys. Stat. Sol. (a)** **200(1)**, 18-21 (2003)
- [35] T. Dieth, H. Ohno, and F. Matsukura, **Phys. Rev. B** **63 (19)**, 195205 (2001)
- [36] T. Dieth, **Phys. Stat. Sol. (b)** **240 (2)**, 433-439 (2003)
- [37] A. Bonanni, **Semicond. Sci. Technol.** **22 (9)**, R41-R56 (2007)
- [38] S. C. Lee, K.R. Lee, and K. H. Lee, **J. Magnetism and Magnetic Materials**, **310**, e732-e734 (2007)
- [39] E. Choi, K. J. Chang, **Physica B** **401-402**, 319-322 (2007)
- [40] C. Y. Fong, V. A. Gubanov, and C. Boekema, **Journal of Electronic Materials**, Vol **29**, No.9, (2000)
- [41] R. Singh, **Journal of Magnetization and Magnetic Materials** **322**, 290-297 (2010)
- [42] A. Bonanni, M. Kiecana, C. Simbrunner, T. Li, M. Sawicki, M. Wegscheider, M. Quast, H. Przybylinska, A. Navarro-Quezead, R. Jakiela, A. Wolos, W. Jantsch, and T. Dietl, **Physical Review B** **75**, 125210 (2007)
- [43] I. Zutic, J. Fabian, S. D. Sarma, **Rev. Mod. Phys.** **76**, 323 (2004)

- [44] K. Audo, H. Saito, V. Zayets, and M. C. Depnath, **J. Phys. Condens. Matter.** **16**, 85541-85548 (2004)
- [45] P. Blaha, K. Schwarz, P. Sorantin, and S. B. Trickey, *Full-potential, linearized augmented plane wave programs for crystalline systems*, **Compound Physics Communications.** **59**, 399 (1990)
- [46] WIEN2K, *An Augmented –Plane-Wave+Local Orbitals Program for Calculating Crystal Properties*, Karlheinz Schwarz, **Techn., Wien, Austria, ISBN 3-9501031-1-2**, (2001)
- [47] N. E. Christensen, O. Gunnarsson, O. Jepsen, and O. K. Andersen, **Journal De Physique, Colloque C8, Supplement au No 12**, Tome 49, (1988)
- [48] J. P. Perdew, S. Burke, and M. Ernzerhof, **Physical Review Letter** **77**, 3865 (1996)
- [49] S. Cottenier, *Density Functional Theory and the Family of (L)APW-methods: a step-by-step introduction*, **ISBN 90-807215-1-4**, version 1.05 (2004)
- [50] B. Crasemann, Kh. R. Karim, and M. H. Chen, **Surface Science Letters**, **V36, I 3**, 355-374 (1987)
- [51] W. E. Palke, and W. A. Goddard, **The Journal Of Chemical Physics**, **Vol. 50, No. 10**, 4524-4533(1969)

- [52] M. Higuchi and K. Higuchi, **Cond. Mat.** **0301578**, 1-23 (2003)
- [53] P. Senet, **J. Chem. Phys.** **107 (7)**, 2516-2524 (1997)
- [54] M. Stadele, M. Moukara, J. A. Majewski, and P. Vogl, **Physical Review B**, volume **59**, Number **15**, 10031 -10041 (1999)
- [55] J. P. Perdew, J. A. Chevary, S. H. Vosko, K. A. Jackson, M. R. Pederson, D. J. Singh, and C. Fiolhais, **Physical Review B**, volume **46**, Number **11**, 6671 - 6687 (1992)
- [56] S. H. Vosko, L. Wilk and M. Nusair, **Can. Journal of Phys.** **58**, 1200 (1980)
- [57] D. C. Langreth and M. J. Mehl, **Phys. Rev. Lett.** B 28, 1809 (1983)
- [58] J. P. Perdew, K. Burke, and M. Ernzerhof, **Phys. Rev. Lett.** **77**, 3865 (1996); *ibid.* 78, 1386(E) (1997)
- [59] E. Malguth, A. Hoffman, and M. Matthew R. Phillips, **Phys. Stat. Sol. (b)** **245**, No. **3**, 455-480 (2008)
- [60] J. P. Perdew, J. A. Chevary, S. H. Vosko, K. A. Jackson, M. R. Pederson, D. J. Singh, and C. Filhais, **Phys. Rev. Lett.** B 46, 6671, (1992)
- [61] O. Arbouche, B. Belgoumene, B. Soudini, and M. Driz, **Computational Materials Science** **47**, 432- 438 (2009)
- [62] A. Lachebi, and H. Abid **Turk. J. Phys.** **32**, 157-166 (2008)

- [63] A. Beloufa, Z. Bensaad, B. Soudini, N. Sekhal, A. Bensaad, and H. Abid, **Int. J. Nanoelectronics and Materials** 2, 11- 22 No. 1, (2009).
- [64] P. Carrier, and S. Wie, **Physical Review B** 70, 035212 (2004).
- [65] A. Lachebi, H. Abid, M. Driz, and Y. Al-Douri, **Int. J. Nanoelectronics and Materials** 1, 81-90 (2008)
- [66] P. Lukashev and Walter R. L. Lambrecht, **Physical Review B** 70, 245205 (2004).
- [67] A. Ben Fredj, Y. Oussaifi, N. Bouarissa, M. and Said, **Phys. Stat. Sol. (b)** 243, No.12, 2780-2787 (2006).
- [68] A. Lachebi, and H. Abid, **Turk J. Physics** 32, 157-166 (2008)
- [69] S. Zerroug, F. A. Sahraoui, and N. Bouarissa, **Journal Of Applied Physics** 103,063510 (2008)
- [70] A. Trampert, O. Brandt, K. H. Ploog, in **Crystal Structure of Group III Nitride, vol. 50**, Academic, San Diego, (1998)
- [71] I. Vurgaftman, J. R. Meger, L. R. Ram-Mohan, **J. Appl. Phys.** 89, 5815 (2001)
- [72] C. Verie, **Mater. Sci. Eng. B** 43 60 (1997)
- [73] A. Qteish and A.I. Al-Sharif, **Physical Review B** 72, 155317 (2005)

جامعة النجاح الوطنية

كلية الدراسات العليا

دراسة أولية للخصائص الالكترونية والتركيبية والمغناطيسية للمخلوط الثلاثي

$\text{Ga}_{1-x}\text{Fe}_x\text{N}$ في حالة التركيب زنك بلند لتركيز $x = (0, 0.25, 0.50, 0.75, 1)$

إعداد

محمود محمد احمد عيسى

إشراف

د. محمد سلامة سالم أبو جعفر

د. عبد الرحمن مصطفى أبو لبده

قدمت هذه الأطروحة استكمالاً لمتطلبات درجة الماجستير في الفيزياء بكلية الدراسات العليا في جامعة النجاح الوطنية في نابلس - فلسطين.

2010

ب

دراسة أولية للخصائص الالكترونية والتركيبية والمغناطيسية للمخلوط الثلاثي $Ga_{1-x}Fe_xN$ في حالة التركيب زنك بلند لتركيز $x=(0, 0.25, 0.50, 0.75, 1)$

إعداد

محمود محمد احمد عيسى

إشراف

د.محمد سلامة سالم أبو جعفر

د. عبد الرحمن مصطفى أبو لبدة

ملخص

نقدم في هذه الأطروحة حساب الخصائص المغناطيسية والالكترونية والتركيبية للمخاليط المغناطيسية $Ga_{1-x}Fe_xN$ في حالة التركيب البلوري زنك بلند لتركيز $x=(0, 0.25, 0.50, 0.75, 1)$ وذلك باستخدام طريقة الموجات المستوية المعدلة الخطية لجهد تام (FP-LAPW). لقد تم استخدام تقريب الكثافة المغزلية الموضعية (LSDA) وتقريب الميل الاتجاهي المعمم (GGA) للجهد التبادلي الترابطي.

البرنامج المستخدم في حساباتنا هو (WIEN2K-code) وهو برنامج خاص مكتوب بلغة فورتران 90 (Fortran 90) على نظام التشغيل لينكس (Linux).

لقد درسنا تطور البنية لحزم الطاقة والعزم المغناطيسي واعتمادها على ثابت الشبكة للمركب نترات الحديد FeN والمخلوط الثلاثي $Ga_{1-x}Fe_xN$.

أظهرت الدراسة الحالية بأن المركب GaN ذو فجوة طاقة مباشرة مقدارها 1.9 إلكترون فولت ($\Gamma-\Gamma$) وفجوة طاقة غير مباشرة مقدارها 3.2658 إلكترون فولت ($\Gamma-X$) وهو مادة شبه موصلة ولا يمتلك الخصائص المغناطيسية في التركيب البلوري الحالي.

تم الحصول على فجوة طاقة متباينة للمخلوط الثلاثي $Ga_{1-x}Fe_xN$ وتبين بأنها تعتمد على تركيز مادة الحديد Fe.

لا يوجد عزم مغناطيسي لمركب نترات الحديد FeN عند حالة الاتزان الحجمي، ولكن العزم المغناطيسي للمخلوط $\text{Ga}_{1-x}\text{Fe}_x\text{N}$ يعتمد مقداره على نسبة تركيز الحديد فهو يتزايد من التركيز $0=x$ الى $0.5=x$ ثم يتناقص الى التركيز $1=x$.

وجد أن قيمة ثابت الشبكة (lattice constant) وكذلك العزم المغناطيسي للمخلوط Ga_1 أكبر باستخدام التقريب (GGA) بالمقارنة مع ما وجد باستخدام التقريب (LSDA) والعكس لمعامل الصلابة (Bulk modulus).